Evolution of Volcanic Unrest Explained by Ash Physical and Compositional Characteristics: Case Studies from Poás and Turrialba Volcanoes, Costa Rica

by

Monserrat Cascante Matamoros

A dissertation accepted and approved in partial fulfillment of the

requirements for the degree of

Doctor of Philosophy

in Earth Sciences

Dissertation Committee:

Thomas Giachetti, Chair and Advisor

Paul Wallace, Core Member

James Watkins, Core Member

Heather Michelle Nicholson Wright, Core Member

Cathy Wong, Institutional Representative

University of Oregon

Fall 2025

DISSERTATION ABSTRACT

Monserrat Cascante Matamoros

Doctor of Philosophy in Earth Sciences

Title: Evolution of Volcanic Unrest Explained by Ash Physical and Compositional Characteristics: Case Studies from Poás and Turrialba Volcanoes, Costa Rica

Volcanic ash offers a window into the subsurface processes occurring within a volcano during an eruption. This dissertation investigates how the physical properties of ash trace the evolution of eruptions at Poás volcano (2016–2019) and Turrialba volcano (2010–2019) in Costa Rica. Variations in the proportions of wall-rock lithics, hydrothermal, recycled, and fresh juvenile material and in the size distributions of the ejected particles indicate changes in conduit dynamics, fragmentation processes and drivers of eruption.

Chapter 2 of this dissertation is previously published coauthored material.

Chapter 2 examines the 2016–2019 eruptive activity at Poás volcano, documenting how rapid changes in ash properties accompanied transitions from phreatic to phreatomagmatic to magmatic eruptions and later recycled-ash activity. Chapter 3 focuses on diagnostic evaluation of particle componentry and morphology to improve the accuracy of ash classifications during small, ash-dominated eruptions, using ash from Turrialba volcano as a case study. Chapter 4 analyzes a decade-long (2010–2019) eruptive sequence at Turrialba volcano, linking trends in ash properties to conduit evolution and monitoring signals. Results show that coarser ash and lower fractal dimensions of the cumulative grain size distributions correspond to shallow hydrothermal fragmentation, while finer ash and higher values of the fractal dimension indicate efficient secondary fragmentation or magma-water interaction. At Poás volcano, these changes are accompanied by strong increases in juvenile material. However, at Turrialba, hydrothermal

dominance persists longer, with only modest contributions of juvenile material. Comparative analysis of these volcanoes offers a framework to recognize shared characteristics relevant to analogue volcanoes and to highlight unique data to individual volcanic settings. This work demonstrates that ash characterization provides independent constraints on eruptive transitions and enhances operational monitoring.

ACKNOWLEDGMENTS

I am profoundly grateful to everyone who helped me complete this dissertation and the research behind it. I owe special thanks to my advisor, Thomas Giachetti, whose encouragement and guidance helped me stay curious and resilient during difficult moments. I am also thankful to my committee members, Paul Wallace, Jim Watkins, and Cathy Wong, for their support and thoughtful feedback. A heartfelt thank you to Heather Wright, working with you has been an honor and a joy.

This work would not have been possible without the collaboration and logistical support of the Costa Rican Volcano Observatory (OVSICORI-UNA). I thankfully acknowledge funding from the National Science Foundation Award 2240044 and the Department of Earth Sciences at the University of Oregon, whose support made this research possible. Thank you to Marla Trox and the department staff who helped me with the university system. Special thanks to the Giachetti Lab group, Josh, Margery, Marcus and everyone who has been around the lab.

The heart of my PhD has been the support of my family and friends. I cannot thank them enough; I am incredibly fortunate to have them in my life. My friends through this journey, the Revelers troupe, the RfLers. Maria Jose, Karla and Marco los quiero mucho. Kellum and Jacob, I will always repeat this: I am soooo glad to have y'all in our life! And of course, Jessie, I would not have made it without you, and you always made it better. And the Jessie clan, Logan and Gus. Adrienne and James took us in like family. Tia Nana and Dieguito who were always there for us. And my Titas and Titos for their love. To all of you thank you, thank you, thank you.

Thank you to my parents Gaby and Diego for all the infinite support. My siblings Majo, Jime, and Diego are my home, my ground, my rock, I love you. Alexa, I love you so much, I will always be your cheerleader. Sean there are no words to express my love for you. And Curtis and Natalie, welcome to the family. I love you all.

DEDICATION

A Tito Rigo y Tita Sole en su honor.

TABLE OF CONTENTS

LIST OF FIGURES

LIST OF TABLES

CHAPTER I

1. INTRODUCTION

Explosive activity at hydrothermally influenced volcanoes generally transitions between eruptive styles. Activity begins with low-energy phreatic eruptions and evolves toward phreatomagmatic and/or magmatic behavior. The initial phreatic eruptions are typically triggered by the over-pressurization of shallow hydrothermal systems that have been sealed over time (Barberi et al. 1992; Stix and de Moor 2018). If magma rises toward the surface, phreatomagmatic activity may occur, and eventually the system may transition to magmatic activity (Hamzah et al. 2025). Once the conduit is sufficiently open and pressure is released, the system may become an open-vent system (van der Laat et al., 2022).

Material from the initial eruptions is typically dominated by wall-rock lithics, altered and hydrothermal material, and fresh new magma input (also known as juvenile material) may be present only in small quantities or not at all (Pardo et al. 2014; Alvarado et al. 2016). Furthermore, the challenge is also due to the character of early juveniles, which are commonly high crystallinity, low vesicularity (Cashman and Hoblitt, 2004). This makes early detection of fresh juvenile material challenging with conventional methods alone. However, identifying the onset of magmatic involvement is crucial because it often signals heightened eruption intensity, changes in plume dynamics, and shifts in hazard potential, particularly for communities living nearby and for downwind aviation operations (e.g., Cashman and Hoblitt 2004; Alvarado et al. 2016).

Physical properties of volcanic ash such as componentry, grain-size distributions, and particle density, capture fragmentation processes of the material involved in the eruptions, and thus provide information on the shallow plumbing system, and its evolution (Cascante et al., 2025). Componentry constrains the relative contributions of juvenile, hydrothermal, altered, and lithic

material; grain-size distributions reflect the efficiency of fragmentation and transport processes; density data provide insights into porosity and material evolution; and fractal dimensions provide insight into the fragmentation processes (Dufek et al., 2012; Kueppers et al., 2006; Matsumoto and Geshi, 2021). These parameters are well-suited to operational monitoring because they can be relatively rapidly obtained within hours of ash collection using standard techniques such as laser diffraction, dynamic image analysis, stereomicroscopy, and SEM imaging. When integrated with monitoring data, they provide a powerful record of conduit processes, hydrothermal sealing and failure, and eruptive transitions (e.g., Gaunt et al. 2016; Shoji et al. 2018; Iguchi et al. 2019).

Rapid ash characterization can provide a high-frequency view of shallow conduit processes that complements monitoring data. **Given the kinds of information we can infer from the physical properties of ash, how can we use that information to detect and interpret eruptive transitions in hydrothermally influenced volcanoes?** This question is addressed in this dissertation through three research chapters, with high-frequency temporal observations and ash collection, method development, and monitoring integration at Poás and Turrialba volcanoes in Costa Rica.

Chapter 2 of this dissertation is previously published coauthored material.

Chapter 2 focuses on Poás volcano during a well-documented eruptive sequence in 2016–2019 and examines how ash physical properties evolve through eruptive transitions. This chapter documents changes in grain-size distributions, componentry, and particle density as the activity shifted from phreatic, phreatomagmatic to dominantly magmatic phases, followed by eruptions rich in recycled ash. The results of this chapter show that coarse-grained, hydrothermal-rich ash is associated with early phreatic activity, while finer-grained, highly recycled ash is associated with high fractal dimensions, indicating secondary fragmentation through particle-particle collisions and

milling. Study results also demonstrate that these transitions in ash properties correspond to documented changes in evolving plume dynamics and conduit width and depth. Therefore, ash can be used as an indicator of evolving eruptive behavior by providing a sensitive record of eruptive processes and their temporal evolution at Poás volcano.

Chapter 3 focuses on improving the accuracy of ash componentry analyses of small ash-rich eruptions dominated by hydrothermal material. To address this problem, hundreds of 250–500 μm grains were tracked across multiple imaging techniques (stereomicroscope, SEM-projected area, and SEM-cross section) to validate the classification made using the stereomicroscope. This study demonstrates that by categorizing ash with binocular microscopy and enforcing the componentry by tracking these particles to analyze internal polish texture, critical questions about the components of eruptive materials can be answered. This chapter also evaluates the utility of characterizing particle morphology in improving componentry analysis in small eruptions. This study highlights how morphological parameters combined with fractal morphology measurements can help distinguish between juvenile particles and other components. Further, by restructuring the classification of ash componentry, we show that small eruption componentry is not a straightforward process. While this chapter emphasizes the necessity of integrating other methods with traditional componentry to enhance monitoring, it also introduces practical correction factors for componentry and concludes that analyzing cross sections of ash particles under the SEM is essential.

Chapter 4 correlates trends between ash physical properties and monitoring signals by examining 29 eruptions of Turrialba volcano from 2010–2019. Measured physical properties include grain size, size-fraction componentry (>125 μm), and density across multiple eruptive phases. Results show that median grain size (D50) is controlled by dispersal controls (upwind vs.

downwind). Densities vary temporally with lower and variable density in the early eruptions (2010-2014), high density in 2015-2016, and comparatively stable densities after 2016. The amount of juvenile material slightly increased after 2016, coinciding with sustained magmatic input and conduit opening. Fractal dimensions demonstrate fragmentation efficiency and distinguish coarse, inefficient hydrothermal fragmentation from finer, more efficiently comminuted (phreatomagmatic/recycled) deposits, mirroring changes in monitoring signals (de Moor et al., 2016a; van der Laat et al., 2022). This chapter provides insight into how conditions and fragmentation efficiency evolved through Turrialba volcanic phases. These insights provide a practical framework for integrating ash data into operational eruption forecasting, particularly for the small, frequent, hydrothermally influenced events common to these volcanoes.

Together, these three chapters demonstrate how ash particle properties can be used to understand subsurface volcanic processes like hydrothermal sealing, changes in magmatic input, and eruptive style transitions. Chapter 2 provides high-resolution documentation of progressive eruptive phases at Poás volcano. Chapter 3 refines methodological approaches to improve ash classification accuracy. Finally, Chapter 4 applies these methods with monitoring signals at Turrialba volcano. This work establishes a robust, process-based methodology for identifying fresh juvenile input and fragmentation efficiency. Such integration is critical for improving hazard assessment and early warning capabilities at active volcanoes with complex hydrothermal systems worldwide.

CHAPTER II

2. CHARACTERISTICS OF VOLCANIC ASH REVEAL CHANGES IN FRAGMENTATION AND ERUPTION DYNAMICS AT POÁS VOLCANO, COSTA RICA, 2016–2019

From Cascante M, Giachetti T, Wright HMN, et al (2025) Characteristics of volcanic ash reveal changes in fragmentation and eruption dynamics at Poás Volcano, Costa Rica, 2016–2019. Bull Volcanol 87:36. https://doi.org/10.1007/s00445-025-01820-5

1. Introduction

Volcanic ash from explosive eruptions can be one of the most far-reaching of volcanic hazards, with potential to impact vulnerable infrastructure and human populations (e.g., Craig et al., 2016; Horwell, 2007; Vargas-Alfaro et al., 2023; Wilson et al., 2012). The fall deposits from explosive volcanic eruptions tend to contain a mixture of particle types—here we use the term juvenile for fresh, not altered magmatic particles and non-juvenile for all other material that is not of fresh magmatic origin (e.g., lithic, loose crystal, fragments of the hydrothermal system). Juvenile particles may exhibit a wide range of sizes, shapes, and textures that are the result of magma vesiculation and primary fragmentation during magma ascent in the conduit, and secondary fragmentation during transport (Dufek et al., 2012; Giachetti et al., 2021; Kaminski and Jaupart, 1998). The study of tephra, defined as any fragments ejected by a volcanic eruption (Cashman and Scheu, 2015), includes the characterization of grain size, shape, texture, and proportion and the interpretation of the origin of juvenile and non-juvenile components, thus providing insights into the last stages of magma transport and fragmentation (e.g., Liu et al., 2017).

A volcanic eruption is classified as ‘phreatic’ in this study if it involves an over-pressurized hydrothermal or groundwater system without direct interaction between magma and water (Barberi et al., 1992) producing a total absence of fragments of juvenile magma in its deposits (Pardo et al., 2014; Stix and de Moor, 2018). Phreatomagmatic eruptions, also known as ‘wet’ or hydrovolcanic eruptions (Alvarado et al., 2016b; Dellino et al., 2011; Liu et al., 2015b, 2017; Lupi et al., 2011;

Miwa et al., 2013; Sheridan and Wohletz, 1981; Zimanowski et al., 2015) occur when magma or hot particles do interact explosively with external water (Houghton et al., 2015). This type of interaction may take place in the shallow plumbing system of the volcano or at the surface, resulting in changes to tephra characteristics. The products of phreatomagmatism have been classically associated with finer grained deposits than their 'dry' eruption counterparts (Aguilera et al., 2012; Barberi et al., 1992; Büttner et al., 2002, 1999; Dellino et al., 2018, 2011; Dellino and Kyriakopoulos, 2003; Taddeucci et al., 2007; Zimanowski et al., 2003, 1997, 1991). Previous studies have suggested that small-scale explosions and/or 'turbulent shedding' of chilled glass at the magma-water interface enhance the fragmentation process (Fagents et al., 2013; Mastin, 2007; Wohletz, 1983). Further, the maximum fragmentation efficiency, which is when the newly fragmented material is the finest, is thought to occur when the water-to-melt ratio approaches ~2–5 (e.g., Fagents et al., 2013). Consequently, the variations in size, texture, and componentry of volcanic ash at a given volcano can provide information about the relative involvement of fluids in the volcanic system, whatever their source (e.g., lake water, water table, or a hydrothermal system; Minami et al., 2016; Ohba and Kitade, 2005).

However, unambiguous identification of juvenile magma in the tephra deposit is not always easy, as widely applied criteria can provide inconclusive results (Pardo et al., 2014). Alteration and (re)incorporation of surrounding rocks, including host rocks and young unconsolidated deposits from previous eruptions may also impact magma fragmentation, eruption dynamics, ash transport and thus our interpretations of the cause(s) of the eruption (D'Oriano et al., 2014; White, 1996). Pardo et al. (2014) demonstrated through textural and chemical analyses of the products of the 2012 Te Maari eruption of Mt. Tongariro, New Zealand, that the fragments of fresh-looking glass in fact originated from country rocks in the vent and that rising magma during this eruption

provided only heat and gas into the overlying, sealed hydrothermal system, triggering a phreatic eruption. Conversely, Cashman and Hoblitt, (2004) showed more than 20 years after the event that the tephra deposit of the pre-climactic, eruption of Mount St. Helens in spring 1980, classified as 'phreatic', in fact contained juvenile glass. Nevertheless, determining whether magma is involved in an eruption—or not—is valuable for evaluating the severity of a volcanic crisis and anticipating its evolution (Montanaro et al., 2022; Stix and de Moor, 2018).

Here we take advantage of detailed sampling of fresh ash products from explosions at Poás volcano (Costa Rica) over a three-year period to study the relationships between the characteristics of the ash particles (componentry, grain size distribution, density, composition) and of the explosions that ejected them (plume height, inferred extent of magma-water interaction, fragmentation processes). We use the term 'explosion' henceforth to refer to a distinct eruptive event producing fall deposits. Our study focuses on the eruption dynamics at Poás volcano from 2016 to 2019, a period during which the volcano experienced major changes in the geometry of its shallow plumbing, hydrothermal system, and crater, with another period of unrest at the time of writing. Geophysical and geochemical monitoring data in previous, multidisciplinary studies describe the volcano's behavior prior to and during this unrest period (e.g., D'Arcy et al., 2022; de Moor et al., 2019; Salvage et al., 2018). We build from this existing framework to provide a more comprehensive understanding of the eruption dynamics of this volcano during this period. We discuss the role of fresh magma in triggering these explosions and provide insights into the mechanism of future 'wet' explosions at Poás volcano and analogous systems globally.

1.1 Poás volcano

Poás volcano is one of Costa Rica's most visited national parks and is located 37 km northwest of the capital San José. It is one of the largest and most active volcanoes in Costa Rica

and is part of the Central American Volcanic Arc, which is a result of subduction of the Cocos plate beneath the Caribbean plate. The active crater of Poás is approximately 1.1 km in diameter, 290 m deep, and often hosts an acidic crater lake (Figure 1) (Martínez et al., 2000). Its geological history dates to 700–600 ka and it compositionally ranges from basaltic-andesitic to dacitic in the most recent lavas unit (56–0.1 ka; Ruiz et al., 2009). The volcano has had several historical major eruptions, the latest one in 1953–1955 (Madrigal and Lücke, 2017), and has also had numerous periods of smaller-scale eruptions. According to Mora Amador et al. (2019), Poás volcano experienced eruption cycles in 1834, 1910, and 1953–1955. A new period of unrest started in 2006 (Martínez Cruz, 2008; Rymer et al., 2009), and de Moor et al. (2019) identified several eruptive phases between 2012 and 2017 based on gas geochemistry and geophysical data. Historically, Poás crater lake is known to disappear and reappear, change in color, and exhibit pH and temperature fluctuations depending on the presence and size of the hydrothermal system beneath it, and/or on the magmatic input into the system (Martínez et al., 2000). During periods of quiescence within the eruptive cycles themselves, the volcano can host the following features and characteristics: fumarolic discharges in the lake, subaerial fumaroles with temperatures ranging from 22 ℃ to a record temperature of 960 °C (recorded in 1981; Casertano et al. 1983), hot springs surrounding the crater, occasional incandescence, changes in lake color, pH values in the lake ranging from 0.87–1.75, and lake temperatures of 33–49 °C (Martínez Cruz, 2008).

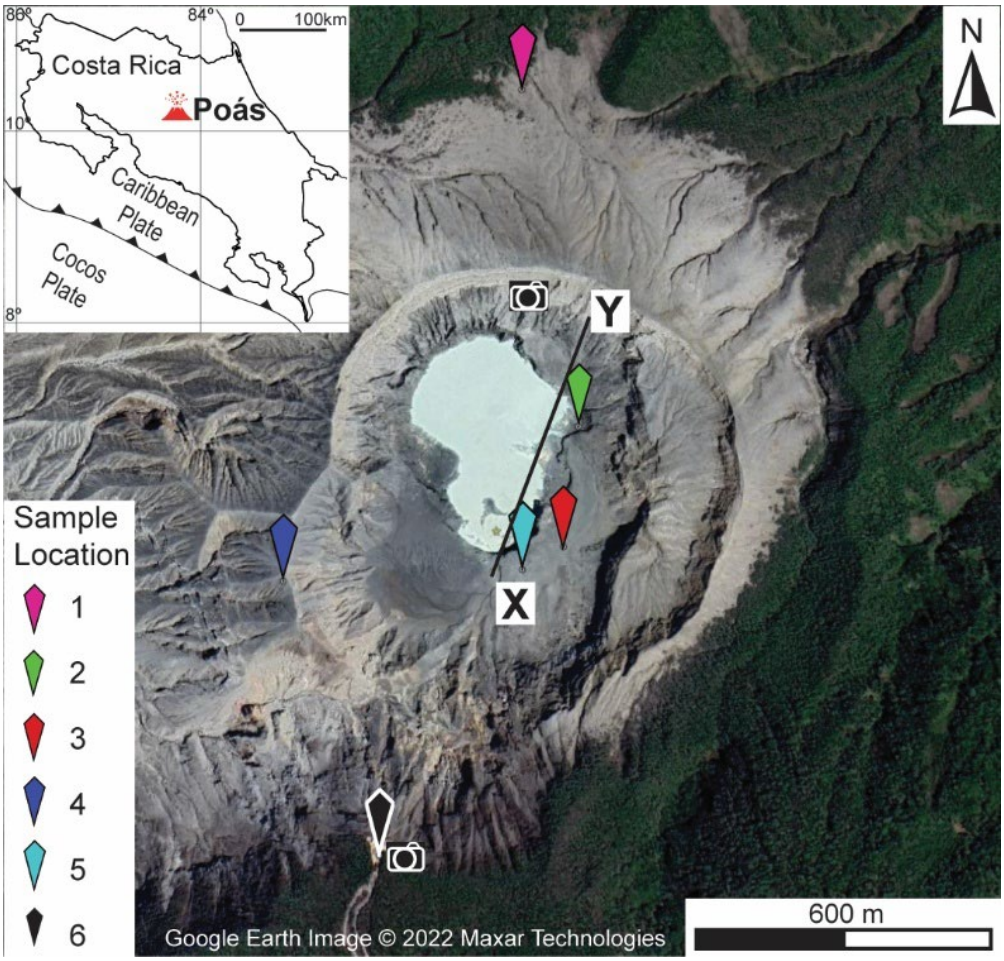

Figure 1. Poás volcano aerial view and insert map of location in Costa Rica. Sample location by color and numbers. Symbol color correlates with sample location and is consistent throughout the figures. Line XY marks the topographic profile used in Figure 3. The camera icons indicate the locations of webcams used to monitor the volcano at different times (see Figure 3). Google Earth© imagery date February 22, 2020.

1.2 Eruptive activity since 2012

Activity at Poás volcano since 2012 can be divided into several eruptive phases (de Moor et al., 2019). The first two phases, with ~150 eruptions between 2012 and August 2014 (phase one), and another ~80 eruptions between June–September 2016 (phase two), are characterized by small 'phreatic' eruptions resulting from the interaction of water and magmatic gas, with little to no direct magma input, and plumes reaching a maximum of 400–700 meters above the crater (de Moor et al., 2019). Although characterized as phreatic by de Moor et al. (2019), the 2016 'energetic, geyser-like eruption' contains ~6% juvenile material in its 250-500 μm size fraction

(Salvage et al., 2018). A third phase in April-November 2017 is described as phreatomagmatic by de Moor et al. (2019), with explosions involving a new batch of magma, which was identified via componentry of the eruptive deposit (de Moor et al., 2019). This activity in 2017 was thought to have been the first involving dominantly juvenile magma since 1953–1955 (Salvage et al. 2018), with >80% of the 250-500 μm size fraction of the ejected tephra being juvenile material at the end of April-June 2017 (de Moor et al. 2019). During this third phase, the highest plumes were recorded on April 14 and April 22, 2017, with heights of ~4,000 m above the crater floor (Figure 2). The whole rock composition of the ejected material in 2017 is andesitic (57.4 wt.% SiO_2; de Moor et al. 2019), slightly more evolved than the basaltic andesite composition of the magma ejected in 1955 (~54.4 wt.% SiO_2; Prosser and Carr, 1987; de Moor et al. 2019). During most of 2018 there was strong degassing, but no ejection of solid material observed, until activity dominated by small phreatic/phreatomagmatic eruptions started again in December 2018 and continued until October 2019. This activity was characterized by plumes with a maximum reported height of about 500 m above the crater floor (Figure 2). Ash emissions ranged in duration from single ~2-minute-long pulses of ash emissions (with recorded plume height), several minutes of passive ash emissions (without recorded plume height), and longer periods of sustained ash emissions for several hours.

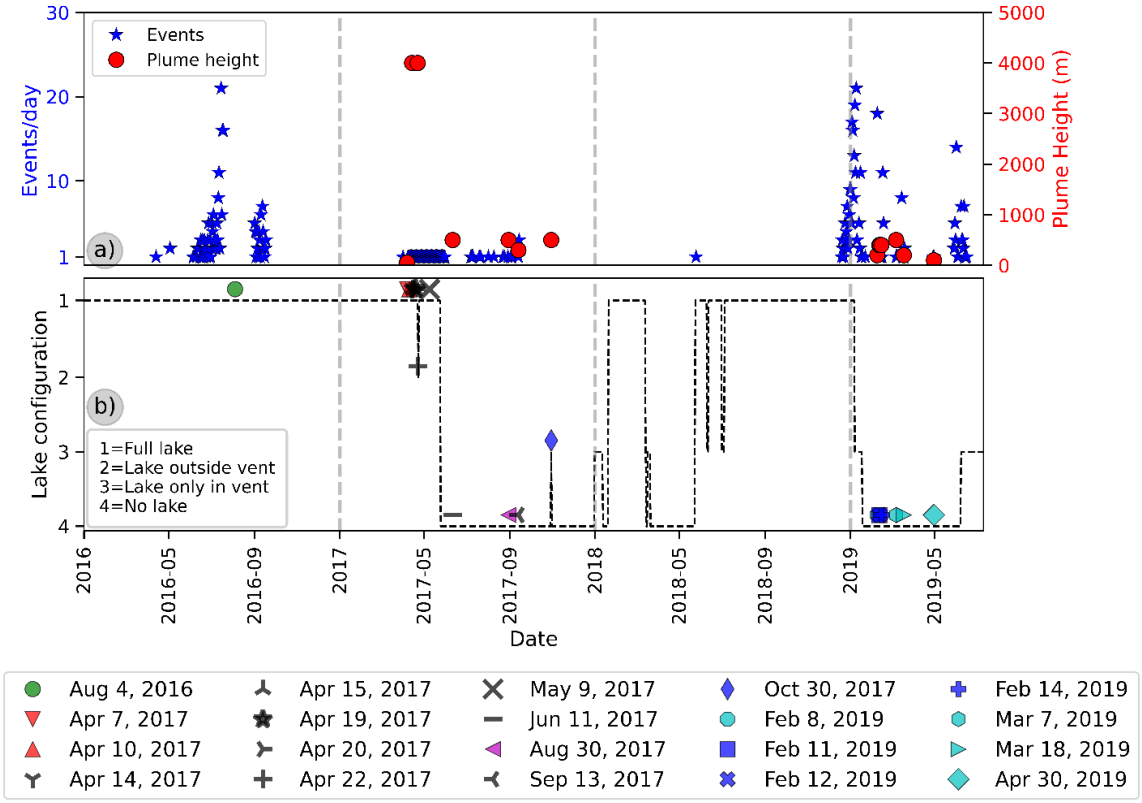

Figure 2. Number of explosive events per day, plume height (when measurable), and configuration of the vent with the crater lake (see Figure 3) at Poás volcano as a function of time. a) Blue stars are the number of explosives, tephra-producing events per day on the left axis, as determined from seismic data. Red circles are plume heights with scale on the right axis, determined from webcam imagery; b) Poás volcano lake configuration, which roughly corresponds to lake size, from a full lake (configuration 1) to no lake (configuration 4). Lake configuration 2 is present only during April 22, 2017. Lake configuration 3 presents during transition between configuration (1) and (4). Collected samples at different lake configurations during the eruption sequence are indicated in (b) with each sample having unique symbology in the bottom legend. Discontinuous gray lines mark the beginning of a year.

Significant changes in the crater lake occurred during the period studied. From 2016 to early April 2017, the lake level was high, and the entire crater floor was under water (Figure 3a). By April 21, 2017, continuous deposition of ejected material close to the vent created a tephra dam separating the active vent from the crater lake (Figure 3b). The most energetic eruption, on April 22, 2017, broke that dam and the lake filled the active vent again. The vent then contained water for short periods of time (Figure 3c) until the end of May 2017, when the water was no longer visible to the cameras, indicating that the lake was very low and possibly mostly gone by that time (Figure 3d). During the first half of 2018, the lake started to re-appear; it was confined within the main vent most of the time (Figure 3c) and sporadically extended beyond it.

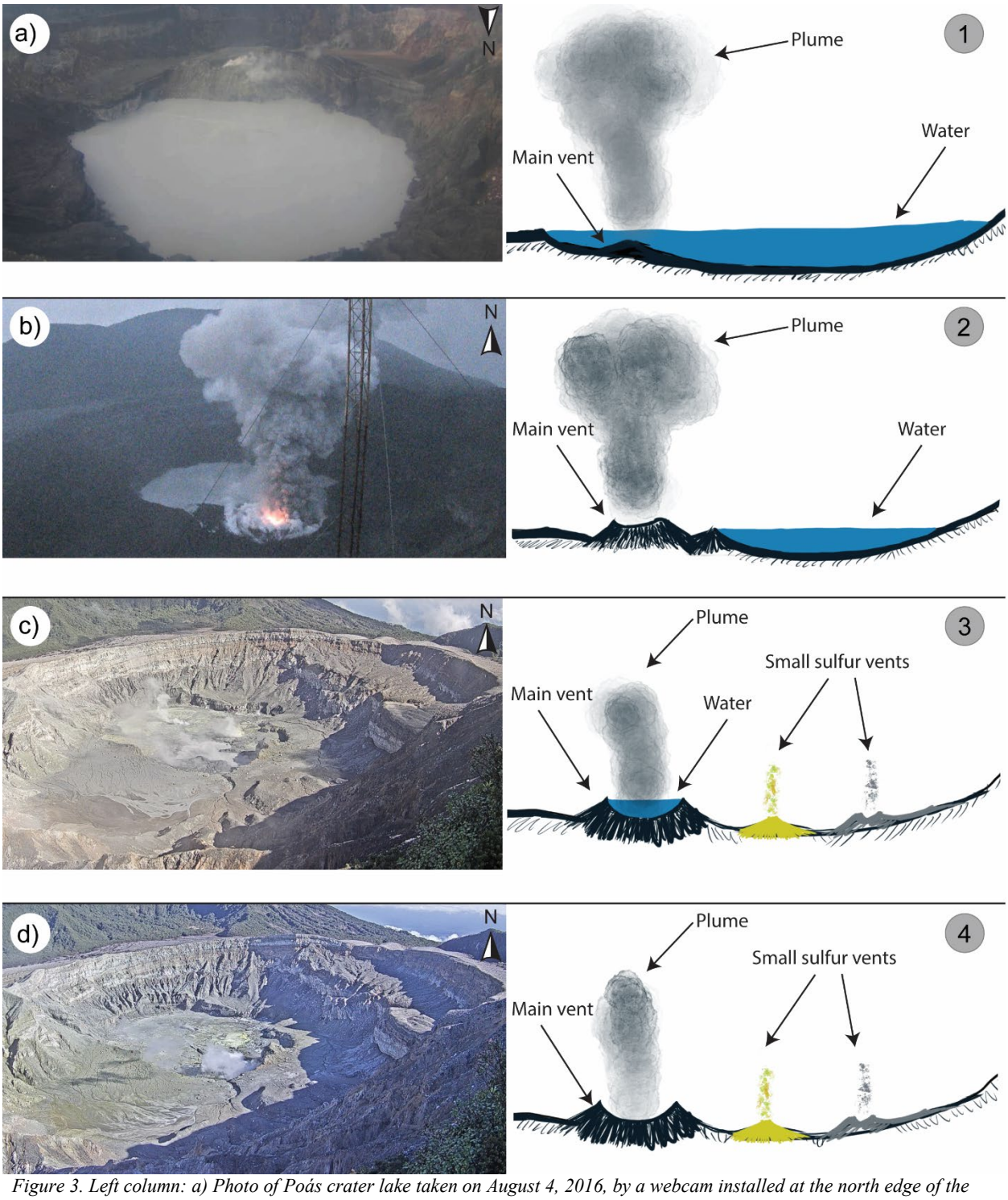

Figure 3. Left column: a) Photo of Poás crater lake taken on August 4, 2016, by a webcam installed at the north edge of the crater looking south. This lake configuration (1) was present from 2016 until mid-April 2017 and between mid-2018 and January 2019. b) Webcam image from April 22, 2017, looking north, showing the lake configuration (2) present during that day only. c) Webcam image from January 8, 2019, looking north. This configuration (3) was present during small periods of time in transition between configuration (1) and (4). d) Image from February 6, 2019. This configuration was present from June 2017 to January 2018 and from February 2019 to June 2019. Right column: sketch of the cross-section of the crater as seen on the corresponding webcam image to the left (see profile marked as XY in Figure 1). Sketch not to scale.

By March 2018, the lake disappeared again for approximately two months; it reappeared at the end of May 2018 but disappeared again between January and June 2019. Two additional, smaller vents covered by the lake exist to the NE of the active vent (de Moor et al., 2016b), but all products collected for this study erupted from the main southern vent.

2. Methodology

2.1 Volcanic plume characteristics and sampling

We collected twenty ash samples from Poás volcano between August 2016 and May 2019, thus covering several of the eruptive phases defined in Section 1.2. Ash was collected at six places around the crater (Figure 1), including at permanent monitoring sites (seismometer or multigas stations) and at the main tourist lookout of Poás volcano. All six sampling locations are within 800 m of the active vent (Figure 1, Table 1). Sample masses vary from about 0.1–1 kg and were typically collected within 24 hours and no more than 48 hours after the explosion that produced them. Plume height was estimated by the Costa Rican Volcano Observatory (Observatorio Vulcanológico y Sismológico de Costa Rica - OVSICORI) via webcam image analysis. Note that plume height was not available for some explosions that occur at night or during cloudy days. Wind speed and direction were estimated from NCEP-DOE Reanalysis 2 data (Kanamitsu et al., 2002) at 200 m above the vent.

Table 1. Explosion data and collection locations (Figure 1) of analyzed samples. The daily wind speed and daily wind direction is the average of the four files available using Reanalysis2 (one wind file every 6 hours) for the day of the eruption, at 200 m above the vent. Plume height above vent was estimated from webcam images; n.a indicates plume was not measurable via webcam due to poor visibility conditions.

Explosion Date (m/d/y)	Sample location (Figure 1)	Easting 16P	Northing 16P	Plume Height (m)	Average wind speed (m/s)	Average wind direction (deg)
August 4, 2016	2	803587	1128583	n.a.	4.1	159
April 7, 2017	3	803559	1128344	50	5.4	249
April 10, 2017	3	803559	1128344	n.a.	5.4	239

April 14, 2017	6	803220	1127777	4000	7.6	254
April 15, 2017	6	803220	1127777	n.a.	7.4	248
April 19, 2017	6	803220	1127777	n.a.	3.5	202
April 20, 2017	6	803220	1127777	n.a.	3.5	174
April 22, 2017	6	803220	1127777	4000	2.0	280
May 9,2017	6	803220	1127777	n.a.	3.6	277
June 11, 2017	6	803220	1127777	500	2.5	234
August 30, 2017	1	803470	1129238	500	4.9	234
September 13, 2017	6	803220	1127777	300	4.7	254
October 30, 2017	4	803013	1128276	500	2.9	170
February 8, 2019	5	803477	1128297	200	5.9	252
February 11, 2019	4	803013	1128276	400	6.0	244
February 12, 2019	4	803013	1128276	400	5.4	229
February 14, 2019	4	803013	1128276	400	4.6	234
March 7, 2019	5	803477	1128297	500	14.3	263
March 18, 2019	5	803477	1128297	200	6.7	233
April 30, 2019	5	803477	1128297	100	7.4	259

2.2 Sieving

All samples were unconsolidated at the time of collection and consisted primarily of ash-sized particles (<2000 μm). Samples were put into a beaker with water and immersed in an ultrasonic bath to disperse aggregates and remove fines from larger particles. We used short intervals of 30 seconds to avoid individual particle breakage. Samples were then wet sieved in whole φ intervals where $\varphi = -\log_2(d)$ with d being the particle diameter in mm. This led to eight sieve fractions from 4000 μm down to <32 μm. Each size fraction was then dried at ~60°C for 24 hours before weighing.

2.3 Particle density

We used a high-precision balance (+/- 0.1 mg) and a Micromeritics AccuPyc II 1340 pycnometer with high-purity helium as the working gas to calculate the density of the solid portion and close pores (i.e., helium-inaccessible) of the ash particles for all sieve fractions. Helium penetrates in between individual grains and within the open pores of the particles at all measured grain sizes, giving the sample volume, and thus, together with the mass measured with the high-precision balance, the average density of the solid portion and closed pores of the grains for each individually measured size fraction. Measurements were repeated five times, and the average density is reported here. Uncertainty on the density is < 10 $kg \cdot m^{-3}$ for all samples determined by propagating the uncertainties associated with the measurements of the mass (balance) and the volume (pycnometer).

2.4 Grain size distribution

The grain size distribution of each bulk tephra sample was obtained by combining individual sieve fractions with detailed measurements acquired by dynamic image analysis and/or laser diffraction, adopting, and adapting the methodology developed by Wiejaczka and Giachetti (2022). We used the masses of each size fraction determined from sieving to quantify the relative weight of each dataset. We calculated the median grain size as the fiftieth percentile on the cumulative grain size curve (Inman, 1949).

2.4.1 Dynamic image analysis (DIA)

The sizes of particles >125 µm were obtained using a Microtrac PartAn^{3D} Particle Size Analyzer at the University of Oregon, USA (Trafton and Giachetti, 2021; Wiejaczka and Giachetti, 2022). A high-speed, high-resolution camera captures images of individual grains of each sieve fraction >125 µm as they fall in air from a vibrating tray, taking 2–15 pictures of each grain. The instrument measures the dimensions of each particle of each size fraction from a series of 2D

projections. Particle volume is calculated by assuming an ellipsoid shape and using the minimal (width) and maximal (length) distance between parallel tangents, taking the minimum difference between the several widths to obtain thickness. Using this instrument, the volume of hundreds of thousands of individual particles were calculated in hours for each sample.

2.4.2 Laser diffraction

The size distribution of particles <1000 μm was measured by laser diffraction on a Beckman Coulter LS 13320 at the U.S. Geological Survey Cascades Volcano Observatory in Vancouver, Washington, USA. We used a refractive index of 1.58 and an absorption coefficient of 0.001 (Romero et al., 2020). The instrument measures the scattering of light by particles that are continuously circulating in water, obtaining the relative volume of particles in 126 size bins between 0.3 μm and 2000 μm.

2.4.3 Combining datasets

To obtain a grain size distribution of the whole sample, we combined data from sieving, DIA, and laser diffraction. Some of the sieve fractions (125–250 μm, 250–500 μm, and 500–1000 μm) were analyzed by both DIA and laser diffraction to examine the compatibility of the data (Supplementary Figure 1). To combine the datasets, we arbitrarily used the laser data for all sieve fractions below 500 μm, and the DIA data above 500 μm. For each sieve fraction, we binned the volumes of individual particles from DIA into 40 regular logarithmic bins covering diameters from 1 μm to 10,000 μm. We interpolated the laser diffraction data into the same bins (i.e., from the original 0.3–1000-μm 126 bins into 1–10,000-μm 40 bins). We then converted these relative volume distributions (both DIA- and laser-derived) into absolute mass distributions using the ash density measured by helium pycnometry and the mass obtained from each sieve fraction. Finally, we added the contributions of all sieve fractions and divided the resulting distribution by the total mass of the sample to obtain the relative mass distribution as a function of particle diameter for the

whole sample.

2.5 Componentry

Particle components were categorized for each sieve fraction from 32–63 μm to 2000–4000 μm. We used photographs acquired with a stereoscope or a petrographic microscope, depending on grain size, as reference to count and categorize every particle within the frame with the software JMicrovision (Roduit, 2007). For the >1000 μm sizes we categorized all the particles available (5–825 grains depending on the sample, with most samples having ~100 grains) and for each size fraction <1000 μm we used 500 particles on most samples and a minimum of 200 particles. Six categories of components were identified: juvenile (dark, transparent, or red), recycled, hydrothermal, lithics, free crystals, and aggregates, following in part de Moor et al. (2019); Gaunt et al. (2016); Houghton and Smith (1993). The characteristics of these components are described below and summarized in Supplementary Table 1 and pictures of the four main components are provided in Figure 4.

- Juvenile particles comprise two types. The first type, which is by far the most abundant, is vesicular with no obvious rounding of particle edges, varying from black/dark brown to transparent, exhibiting a glossy luster, and lacking signs of weathering or erosion. Scanning Electron Microscope images of the particles reveal a smooth glass-surface morphology. Backscattered electron images show fresh groundmass and unaltered phenocrysts. The other type, far rarer, consists of reddish, porous particles, i.e., scoriae ("red" category in the componentry).
- Lithics are gray, opaque, vesicle-free, slightly more rounded than juvenile particles, and do not show any evidence of weathering or alteration. These clasts are inferred to derive from the deposits of older eruptive episodes at the volcano, or from basement rocks.

- Recycled particles are characterized by reworked, rounded grain edges and/or a dull luster. These grains appear to be mostly juvenile particles that were lightly physically altered and thus lost their vitreous luster. Some of the particles contain clay or oxidation of the surface. These particles are usually translucent-transparent and/or black in color.
- Hydrothermally altered material shows a wide variety of colors and luster, including metallic luster, yellowish color of sulfide minerals, and/or white color. These particles are inferred to record interaction with hydrothermal fluids and hence are inferred to originate from the hydrothermal system.
- Free crystals consist of rock-forming minerals such as plagioclase, olivine, pyroxene, zeolite, and secondary minerals. Free crystals are quite rare in the samples collected.
- Aggregates were identified as subspherical clumps of ash that lack any internal microstructure (massive). They may have formed from moisture in the volcanic plumes, but we cannot rule out the possibility of a post-depositional origin. Because we were primarily interested in analyzing the proportion of different components and their primary size distribution at fragmentation, we attempted to gently break down aggregates in the deposits. Most of the aggregates broke up during processing, but we created a separate category for those that survived ultrasonication and wet sieving, suggesting they were cemented enough to remain intact. Our aggregate counts provide a qualitative indication of plumes that may have incorporated more moisture from the vent region and/or atmosphere. Overall, intact aggregates were rare and found only at sizes >125 μm.

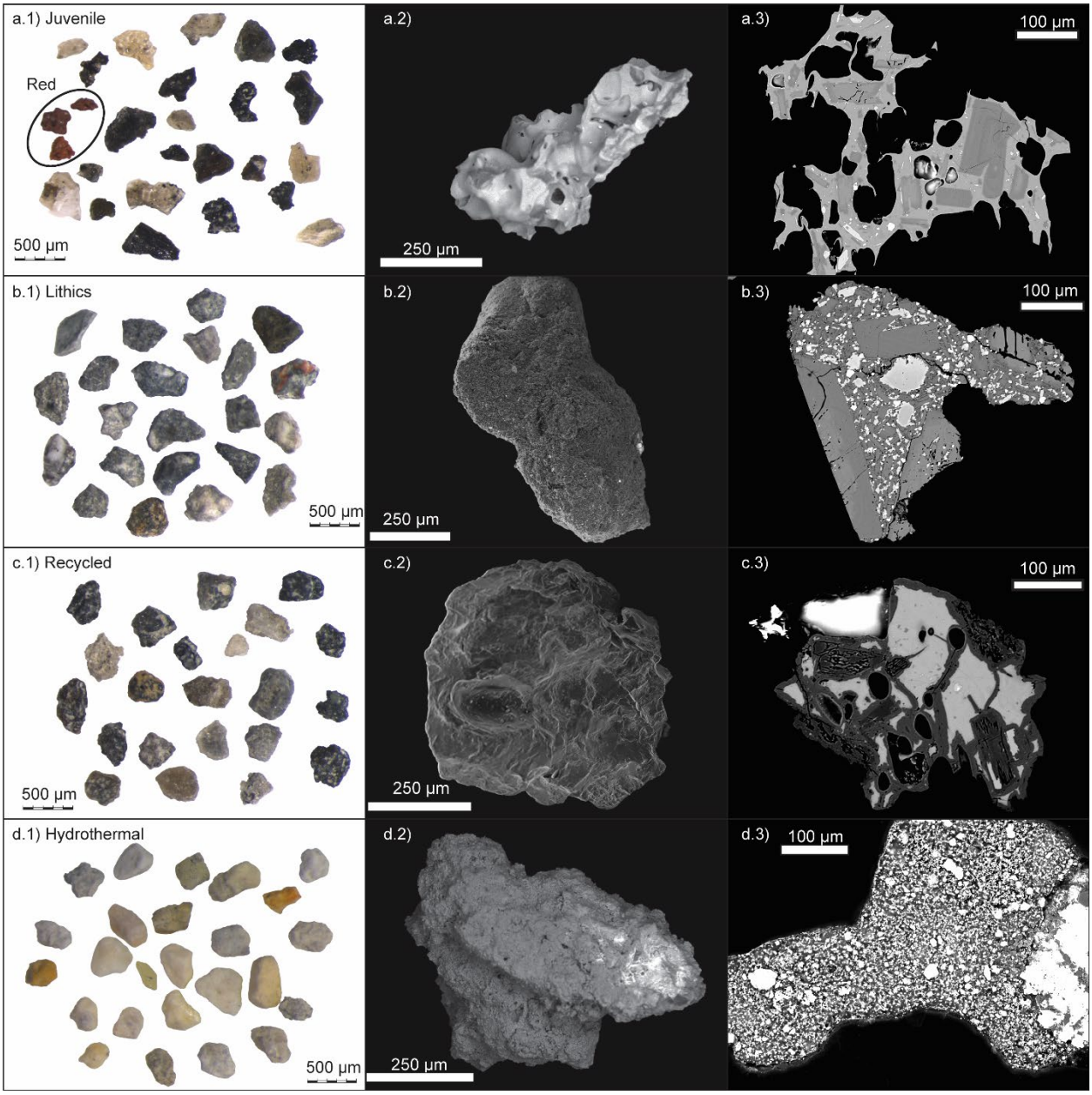

Figure 4. Four principal components found in the samples studied. All particles shown here come from the explosions on April 19 and April 22, 2017. a.1) Stereomicroscope image of juvenile components, including dark, and transparent types. Red particles are separated in a circle because they are counted as a sub-category in the juvenile componentry.a.2) SEM image of juvenile particle external morphology. a.3) BSE-SEM image of juvenile groundmass texture showing fresh glass, well-formed vesicles and phenocrysts of plagioclase and smaller size pyroxenes. b.1) Stereomicroscope image of lithics components. b.2) SEM image of lithic particles showing the external morphology. b.3) BSE-SEM image of lithic components showing the internal groundmass showing high crystallinity and low vesicularity. c.1) Stereomicroscope image of recycled particles. c.2) SEM image of recycled particle external morphology. c.3) BSE-SEM image of recycled components showing opal replacement on phenocryst and fractures and some fresh glass in the core of the particle. d.1) Stereomicroscope image of hydrothermal particles. d.2) SEM image of hydrothermal particle external morphology. d.3) BSE-SEM image of recycled particle internal structure. Because of their rarity, free crystals and aggregates are not included here.

Validation of the componentry analysis was conducted by isolating 25 particles from each category using a binocular microscope (column 1 on Figure 4). Subsequently, their external

textures (column 2 on Figure 4) were examined through scanning electron microscopy with secondary electron imaging (SEM-SE), and the internal groundmass textures (column 3 on Figure 4) were analyzed using backscattered electron imaging (SEM-BSE). This validation, performed on three samples with a 25-particle count per sample, yielded a relative error of 8–16% for the component percentage estimates. The most common source or error is a misinterpretation of a 'juvenile' particle for a 'recycled' one, or vice versa.

2.6 Electron Microprobe Analysis (EMPA)

To ascertain their juvenile origin, the major element composition of many ‘juvenile’ particles from three characteristically distinct explosions (August 04, 2016, April 22, 2017, and February 11, 2019) were obtained via EMPA at the Center for Advanced Materials Characterization in Oregon, at the University of Oregon. For each explosion, six to seven individual 250–500μm particles categorized as juvenile were embedded in resin, polished, carbon-coated, and analyzed using a Cameca SX-100 equipped with five wavelength dispersive spectrometers and a 15 kV accelerating voltage. The 5-μm spot targeted areas of fresh glass in between crystals (ranging in size from phenocrysts to visible microlites) and 1–2 spots were acquired per grain, resulting in 12–14 measured compositions per explosion (Supplementary Table 2). We also analyzed the groundmass glass in seven fragments of a single scoria sample ejected in 1955, during the 1953–1955 eruptive phase of Poás, to evaluate the chemical evolution of the magma between the two successive eruptive periods. This scoria was chosen because it was a typical clast in the deposit. Fragments come from the same scoria sample analyzed by de Moor et al. (2019) by x-ray fluorescence for whole rock composition.

3. Results

3.1 Density from helium pycnometry

Density data are reported in Table 2. The density of particles in the sieved samples varies

from 2200 kg·m^{-3} (particles <32 μm ejected on August 4, 2016) to 2850 kg·m^{-3} (particles 125–250 μm ejected on September 13, 2017). The variation in density between the size fractions of a single sample is 1–15% and 6% on average. This variation can be explained by 1) changes in the componentry from one size fraction to another and/or 2) variations in the isolated (i.e., closed) porosity of the particles with grain size. The exact impact of the variation in componentry is difficult to predict as it depends on the density of each component, which is unknown. The presence of isolated pores within some of the grains would cause an overall decrease in the measured density, because of a higher helium-inaccessible volume for the same mass. SEM images of the different components (Figure 4) suggest that juvenile material (and recycled to a lesser extent) is the component most likely to contain isolated pores. To estimate the impact of isolated porosity on the measured density, we remeasured the density of three size fractions (63–125 μm, 250–500 μm, and 1000–2000 μm) of a sample containing a high proportion of juvenile material (April 22, 2017, with 77 vol.%, 73 vol.%, and 60 vol.% of juvenile material for these size fractions, respectively) after finely grinding the grains to break any isolated pores. We see an increase in density from +20 kg·m^{-3} to +40 kg·m^{-3} between the non-ground and ground particles, confirming the presence of isolated pores in some of the grains. This accounts for an increase in density of 3%, which is below the average variation observed from one size fraction to the other within the same sample (6%), and from sample to sample (up to 24%, as shown below). We thus conclude that, for this sample suite at least, the change in componentry is the primary factor affecting changes in the density of the sample.

Table 2. Average particle densities from each sieve fraction for all the samples studied, obtained by helium pycnometry. Absence of data means there are no particles in the given size fraction, or the volume of particles is too small for analysis by helium pycnometry.

Density by size fraction ($kg \cdot m^{-3}$). Uncertainty for all the data is ±10 ($kg \cdot m^{-3}$)								
	Size fraction in microns (μm)							
Explosion Date (M/D/Y)	0–32	32–63	63–125	125–250	250–500	500–1000	1000–2000	2000–4000
August 4, 2016	2198	2257	2258	-	-	-	-	-
April 7, 2017	2429	2392	2375	2322	2298	2304	2317	-
April 10, 2017	2378	2294	2267	2277	2270	2274	-	-
April 14, 2017	2626	2624	2655	2625	2607	2568	2551	-
April 15, 2017	2566	2610	2632	2625	2662	2641	2590	-
April 19, 2017	2587	2622	2638	2653	2665	2623	2610	-
April 20, 2017	2478	2506	2531	2573	2592	-	-	-
April 22, 2017	2555	2608	2669	2697	2725	2705	2696	2695
May 9,2017	2545	2596	2683	2673	2745	2720	2785	-
June 11, 2017	2483	2554	2681	2773	2816	-	-	-
August 30, 2017	2674	2738	2783	2730	-	-	-	-
September 13, 2017	2540	2637	2788	2850	2813	-	-	-
October 30, 2017	2537	2559	-	-	-	-	-	-
February 8, 2019	2305	2559	-	-	-	-	-	-
February 11, 2019	2440	2332	2339	-	-	-	-	-
February 12, 2019	2507	2371	2450	-	-	-	-	-
February 14, 2019	2513	2452	2575	-	-	-	-	-
March 7, 2019	2446	2466	2435	-	-	-	-	-
March 18, 2019	2439	2491	2573	2680	-	2474	-	-
April 30, 2019	2446	2496	2465	2811	-	-	-	-

Density values for the 0–32 μm and 32–63 μm size fractions are within 5% of each other for all the samples (<2% on average, Figure 5a). Based on this observation and because we could

not conduct componentry analysis for the smallest particles, we assumed that the componentry of the <32 μm fraction is identical to the 32–63 μm size fraction (Figure 5a). Using the density and relative mass of each size fraction, it is possible to calculate the average density of the particles of all sizes, which varies from 2227 kg·m^{-3} (August 4, 2016) to 2768 kg·m^{-3} (September 13, 2017). When looked at as a function of time, density is 1) relatively low for explosions prior to April 10, 2017 (2293±58 kg·m^{-3}); 2) sharply increases in 2017 from 2315 kg·m^{-3} on April 10 to 2622 kg·m^{-3} on April 13, 2017; 3) further gradually increases between April 13, 2017 (2622 kg·m^{-3}), and September 13, 2017 (2768 kg·m^{-3}); and 4) finally decreases and stabilizes around a value of 2443±73 kg·m^{-3} in 2019 (Figure 5b).

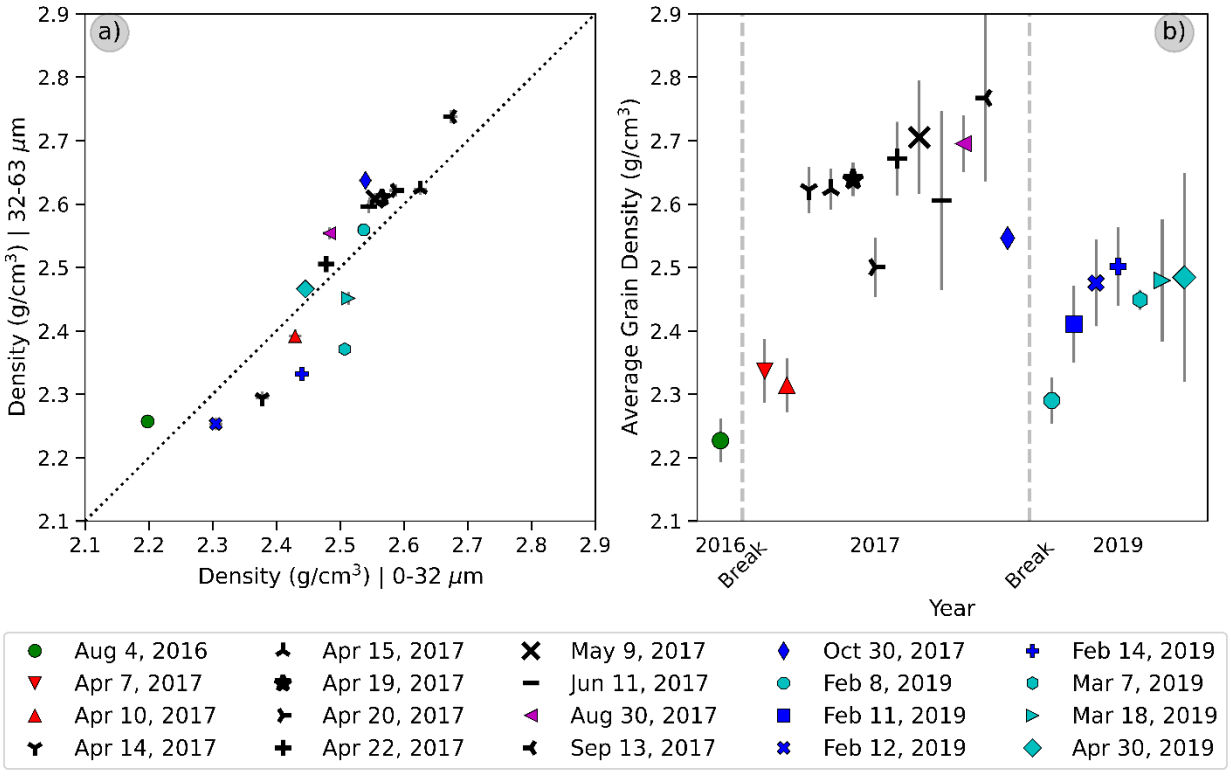

Figure 5 a) Density of particles in the 0–32 μm and 32–63 μm size fractions of each sample as measured by helium pycnometry. Error bars are gray; errors are one standard deviation. Where not visible, the error bar is smaller than the symbol itself. b) Density averaged over all grain sizes with the standard deviation shown in gray bars. The dashed gray lines show a break in time from different events.

3.2 Grain size

Supplementary Figure 1 shows the good agreement between laser diffraction and dynamic

image analysis (DIA) using two sieve fractions of the same sample. The merging of grain size data from three methods (sieving, DIA, laser diffraction) results in artifacts in the final distribution, especially where the laser and DIA data merge (see sharp deviations 400–700 µm for most samples; Figure 6). The challenges of merging different grain-size datasets are complex, as discussed by Dinis and Castilho (2012), and are the subject of ongoing investigation. However, for the purposes of this study, we do not believe this analytical artifact impacts our overall interpretations because the most key features are found at sizes < 500 µm, which relied only on the laser diffraction technique.

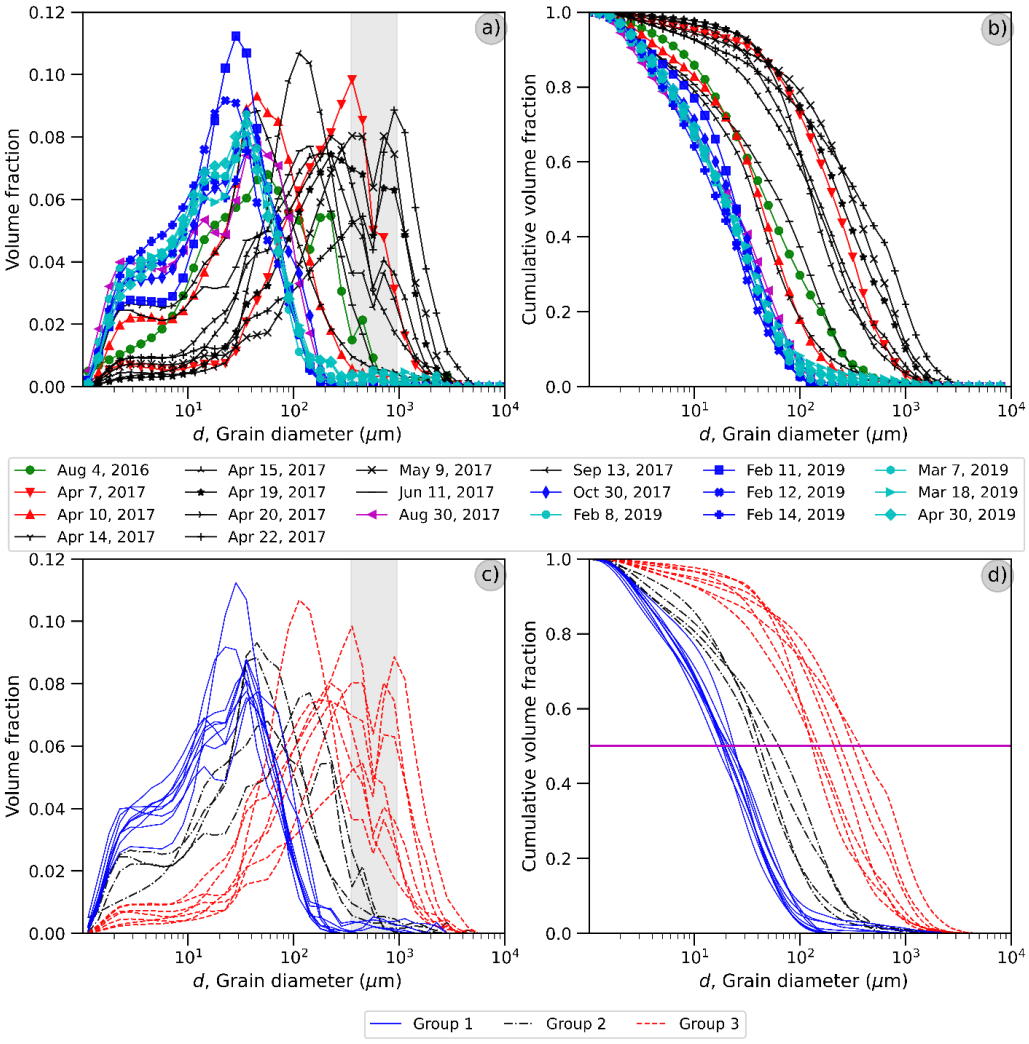

Figure 6. a) Grain size distribution and b) Cumulative Volume Fraction of all the samples. Colors represent the location (see Figure 1 and Table 1). c) and d) are the same as a) and b), but here colors represent the three distinct size groups identified

(see text). Group 1 has a median diameter <30 μm, group 2 has a median diameter of 30–100 μm, and group 3 has a median diameter >100 μm. The magenta horizontal line in d) represents 50% of the whole volume of the sample (i.e., cut the distribution at the median diameter). The gray rectangle in a) and c) shows the artifact created by the merging of data between laser diffraction and photogrammetry (see text for explanation).

Results of the grain size analysis are provided in Figure 6 in both differential and cumulative volume fraction as a function of particle equivalent diameter (d). Additionally, the median diameter of each sample is provided in Supplementary Table 3. Altogether, the volume fraction (Figure 6a, c) and the cumulative volume fraction (Figure 6b, d) show three distinct grain size distributions groups: Group 1 is characterized by small grain sizes (nine samples with a median diameter <30 μm), Group 2 is made of four samples with an intermediate median diameter of 30–100 μm, and Group 3 with large grain sizes (seven samples with a median diameter >100 μm). Group 1 (in blue in Figure 6c-d) is made of unimodal distributions with a median diameter of 16–24 μm and a subpopulation mode between 2–8 μm. Further, Group 1 comprises all (and only) products of explosions that occurred after August 2017, which are also characterized by a high content of recycled material (>56 vol.%) and an extremely low proportion of lithics (≲2 vol.%). On the other end of the size spectrum, Group 3 (in red in Figure 6c-d) is composed of seven roughly unimodal grain size distributions with a median diameter of 137–370 μm, and a fine tail around 2–25 μm. There is more diversity in terms of grain size distribution and componentry in this group. All samples containing >50 vol.% of juvenile material have median diameters 130–370 μm and fall into this Group 3; as do all samples containing appreciable lithic material (>15 vol.%) that have median diameters of 137–242 μm. Group 2, at intermediate sizes, contains two samples with high amounts of hydrothermal material (35–64 vol.%) and another two samples with a mix of recycled (35–65 vol.%) and juvenile (19–32 vol.%) material, and with an intermediate amount of lithics and crystals (2–10 vol.% total).

3.3 Componentry

Results of the componentry analysis are provided in Supplementary Table 4 and presented in Figure 7 (for each sieve fraction) and in Figure 8 for the weighted-average sample (weighted average, at the sample scale). Because of the limited variation in particle density between the individual size fractions of a given sample (6% on average, see Section 3.1), the componentry can be expressed both in mass (wt.%) or volume (vol.%) terms.

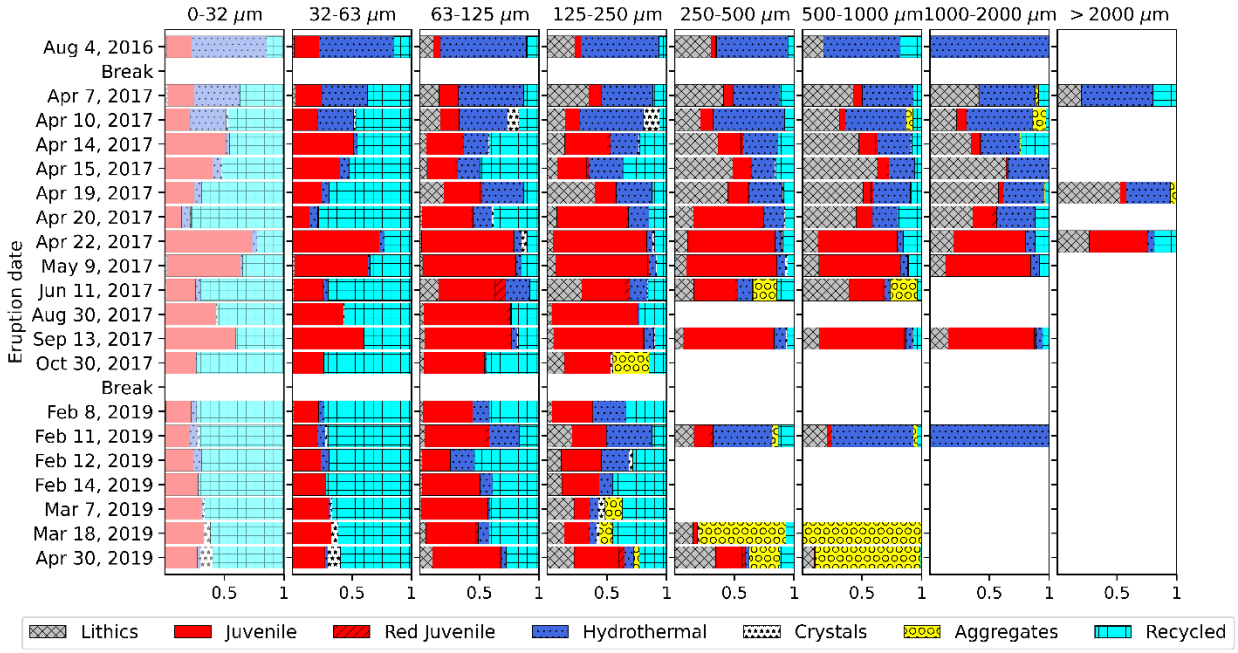

Figure 7. Componentry of all individual size fractions for all the samples analyzed. The componentry of the 0–32 μm size fraction is faded in the figure, highlighting the assumption that the 0–32 μm size fraction componentry is equal to that of the 32–63 μm size fraction (see text for explanation).

Except for particles >250 μm in the two samples analyzed from 2019 (March 18 and April 30, 2019), both crystals and aggregates are rare in all samples and at all size fractions (Figure 7), together accounting for <10% of the weighted-average sample; therefore, they will not be discussed in depth here. Lithic, juvenile, hydrothermal, and recycled particles thus always account for >90% of the volume (or mass) of a sample (Figure 8). Where present, hydrothermal material is visible in all size fractions, with a relatively higher proportion in particles >63 μm. The proportion of hydrothermal material gradually decreases with time from 64 vol.% in August 2016 down to ~9

vol.% on April 20, 2017, and remains low after that (5±4 vol.%). Lithic fragments, when present, are concentrated in size fractions >250 μm and account for >50% of particles >500 μm in some samples (April 15 and 19, 2017, Figure 7). At the sample scale, we note an overall increase in lithics from <6 vol.% in August 2016 to a maximum of ~34 vol.% on April 19, 2017. This increase is followed by a decrease down to <5 vol.% by the end of 2017 and samples from the 2019 explosions essentially lack lithic fragments (<1 vol.%). Fresh, juvenile particles are found in almost all size fractions of all samples (Figure 7) and account for at least 12 vol.% of each sample. The black-to-transparent type always dominates the juvenile component (90% to 99% of juvenile clasts) at the expense of the red type. Between April 22 and September 13, 2017, the juvenile magmatic component was predominant in three explosions (April 22, May 9, September 13), with proportions between 70–72 vol.% of total sample. The explosions on June 11 and August 30 had a lower percentage of juvenile fragments, 32–46 vol.%. Starting with the explosion on October 30, 2017, and throughout 2019, the percentage of juvenile fragments stabilizes around 30 vol.%. Recycled material is found in all size fractions of all samples, although its proportion is always higher in size fractions <125 μm. At the sample scale, the amount of recycled material increases from 13 vol.% in August 2016 to 66 vol.% on April 20, 2017, fluctuates between 14 and 52 vol.% during the period of April 22-August 20, 2017, and stabilizes around 60 vol.% through 2019 (Figure 8).

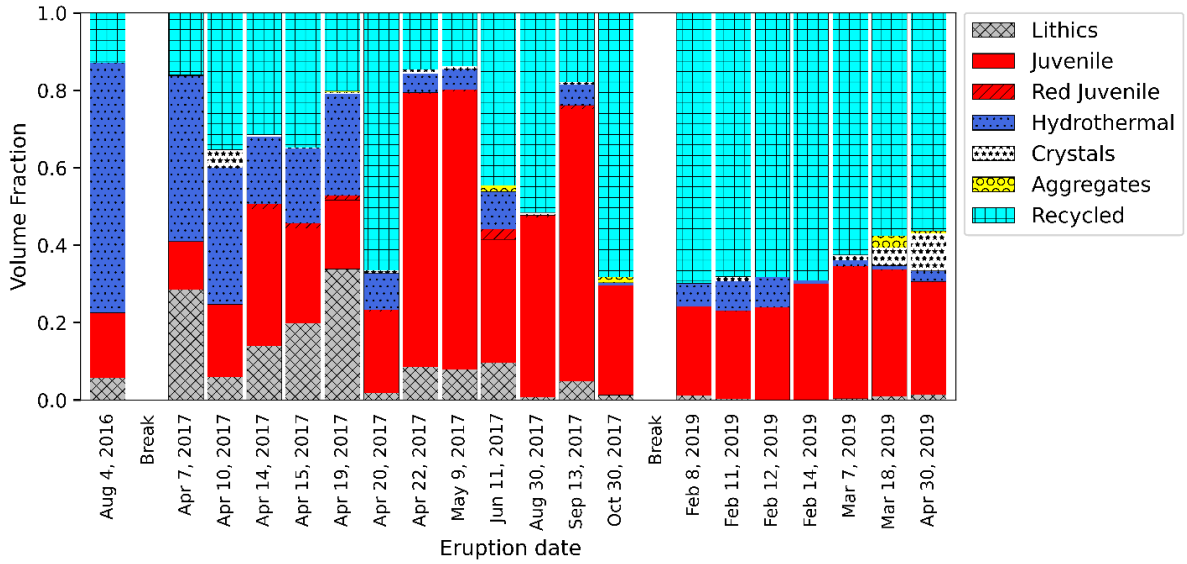

Figure 8. Componentry of the whole samples obtained via a weighted average using the componentry of each size fraction and its relative volume contribution to the whole sample, and assuming the componentry of the 0–32 μm size fraction is equal to that of the 32–63 μm fraction (see text for explanation).

3.4 Chemical composition of the groundmass glass

The compositions of the groundmass glass of the juvenile fragments from explosions in 1955, August 04, 2016, April 22, 2017, and February 11, 2019, obtained by EMPA, are provided in Supplementary Table 2, plotted in Figure 9, and backscattered electron images of some of the grains analyzed are provided in Supplementary Figure 2. Also provided in Supplementary Table 2 for reference, are the whole rock compositions of two scoria samples from the 1955 eruption (de Moor et al., 2019; Prosser and Carr, 1987) and of another two bombs from the explosion on April 22, 2017 (de Moor et al. 2019), obtained by X-ray fluorescence. These are, to our knowledge, the only other chemical compositions of solid products of Poás available in the literature from the 1953–1955 eruptive period and the eruptive period that started in 2006. All percentages in Supplementary Table 2 are normalized to 100 wt.%.

Supplementary Table 2 and Figure 9 show that the composition of the groundmass glass in juvenile products varied significantly between 1955 and 2019, from an average andesitic composition in 1955 (57.8±0.2 wt.% SiO_2, 5.2±0.2 wt.% Na_2O+K_2O) and 2016 (albeit with more

variations, 59.4±1.8 wt.% SiO_2, 5.5±0.5 wt.% Na_2O+K_2O), to dacitic in 2017 (67.7±0.7 wt.% SiO_2, 6.9±0.4 wt.% Na_2O+K_2O), and then trachyandesitic/trachytic in 2019 (62.4±0.4 wt.% SiO_2, 7.6±0.3 wt.% Na_2O+K_2O). Although variable through time, the compositions of the groundmass glass of the 6-7 individual juvenile fragments analyzed within each of the explosions in 2017 and 2019 are, however, restricted to narrow ranges for most elements, forming two distinct clouds in all classical Harker diagrams (Supplementary Figure 3). The juvenile fragments ejected during the 2016 explosion can be categorized into roughly two groups; the first group is compositionally in all respects like the juvenile glass from the 1955 eruption, while the second group is more evolved (61±0.7 wt.% SiO_2, 5.9±0.5 wt.% Na_2O+K_2O) and exhibits an intermediate composition between the groundmass glass of the 1955 scoria and the two groups formed by the 2017 and 2019 explosions (Figure 9).

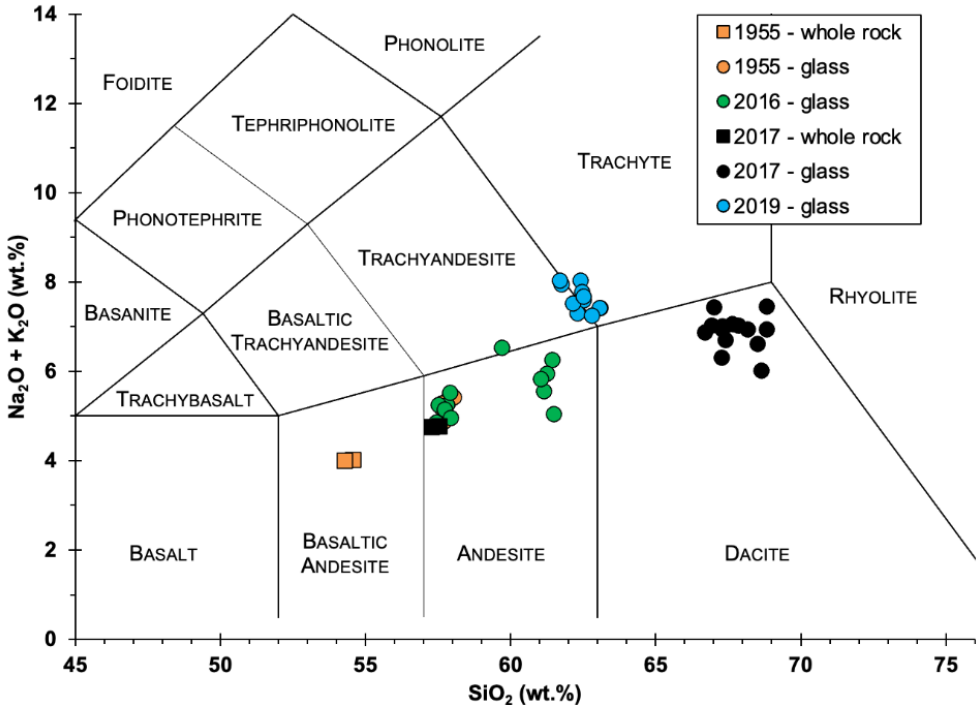

Figure 9. Whole rock and groundmass glass composition of juvenile clasts from explosions at Poás in 1955, August 4, 2016, April 22, 2017, and February 11, 2019. Groundmass glass compositions of ash grains were obtained by electronic microprobe in this study whereas whole rock compositions were obtained by x-ray fluorescence by Prosser and Carr (1987, scoria from 1955 eruption) and de Moor et al. (2019, scoria from 1955 and bombs from 2017). Each dot represents the average measured composition of an individual ash grain. Oxide analyses are normalized to 100% on an anhydrous basis.

The juvenile groundmass glass of the 1955 bomb is ~2 wt.% richer in SiO_2 than the corresponding whole rock composition, whereas the groundmass glass of the 2017 juvenile products is ~10 wt.% richer in SiO_2 than the 2017 whole rock composition, with a large difference in K_2O wt.% of ~2 wt.% (Figure 9).

4. Discussion

4.1 Factors controlling erupted grain size

4.1.1 Componentry

The componentry of the ash varies widely among size fractions within a single sample (Figure 7), and among different samples (Figure 8). These variations in componentry correlate with the grain size distribution of the tephra. When present, recycled particles concentrate in the smaller size fractions (<125 μm), whereas lithic particles prevail above 250 μm (Figure 7). Conversely, the juvenile and hydrothermal fragments are found in large quantities at all size fractions when they volumetrically dominate the whole sample (see explosions on April 22, May 9, and September 13, 2017, in Figure 7 for juvenile fragments, and August 4, 2016, for hydrothermal material).

We note that the finer grained the deposit the more abundant the recycled particles (Figure 10). The two end-member groups identified on the grain size distribution plots (Groups 1 and 3, see Figure 6) are also clearly visible in Figure 10: all samples in group 1, which have a median diameter <30 μm, have a recycled volume percent >50 % (and almost no lithics), whereas for samples in group 3, with a median diameter >100 μm, the recycled volume percent is <35%. Samples of group 2, intermediate in size, have intermediate volume contents of the different components, with no apparent relationship with the recycled material. We also note that the deposits containing relatively high amounts of lithics (20–34 vol.% on April 7, 15 and 19, 2017) have high median diameters (150–240 μm). Many studies attribute the high proportion of fine ash to phreatomagmatic eruptions; however, whole-deposit grain-size distribution is necessary to

assess this feature (White and Valentine, 2016). And as we discussed in this section, the grain size distribution during these 2016–2019 explosions at Poás, seems to correlate primarily with the relative proportion of each component present in the ejected ash.

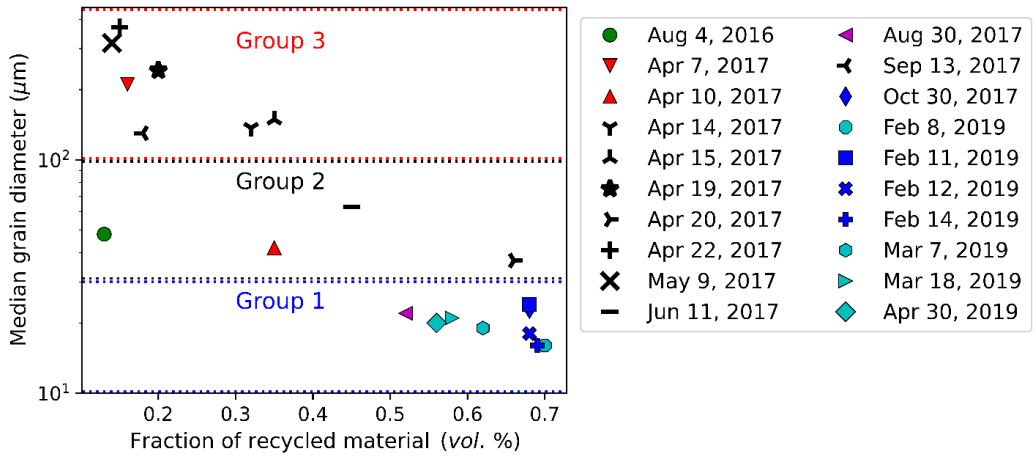

Figure 10. Median grain diameter as a function of the volumetric fraction of recycled material. The three groups defined based on median grain size (see Figure 6c and 6d) are represented. Each symbol represents a sample and is color-coded by location (see Figure 1).

4.1.2 Plume height, wind, and sample location

At any given site, deposit grain size distributions reflect changes in plume dynamics, background wind velocity, and sample location with respect to the overall deposit dispersal axis. In our dataset the plume height varies widely among explosions (50–4,000 m above vent level). In addition, explosions occur at different times of the year, and samples were collected at six locations around the vent (and at only one location per explosion). Teasing out the role of these factors on our measured grain size is not straightforward (Figure 11). First, the samples collected closest to the vent (~100 m) are amongst the finest, whereas the three coarsest samples were collected at 600 m from the vent, farther away than most of their counterparts (Figure 11a). Some samples collected at the same location cover an order of magnitude or so in median diameter (see red and black symbols in Figure 11a). Second, there is no clear correlation between plume height and median grain size of the sample in Figure 11b (noting that many plume heights are missing due to

nighttime and/or cloudy conditions). Third, we do not observe any obvious trends when the median diameter of a sample is plotted as a function of the direction or speed of the wind prevailing during the explosion (Figure 11c, d). To investigate whether a combination of wind direction and sample location could explain the variations in deposit grain size (in terms of median diameter), we calculated the location of the sample compared to the main dispersal axis of the tephra deposit, assuming the latter is the same as the direction of the wind 200 m above the crater during the day of the explosion. Thus, samples located downwind at a low angle compared to the main dispersal axis and close to the vent should in theory have the coarsest particles. Figure 11e-f show that the coarsest samples were collected almost perpendicular to the main dispersal axis at ~600 meters from the vent, whereas most samples collected closer to the vent and within ±30 degrees from the main dispersal axis are amongst the finest samples, with median diameters around 20 μm. Overall, these results suggest that, within the resolution of data available for this study, the plume height, sampling location, and wind patterns affect deposit grain size in a less straightforward way than sample componentry (particularly recycled material, Figure 10). Having only a single sample from each explosion, rather than a network of samples to characterize the full deposit, prevents more sophisticated examination of the atmospheric plume transport and deposition processes.

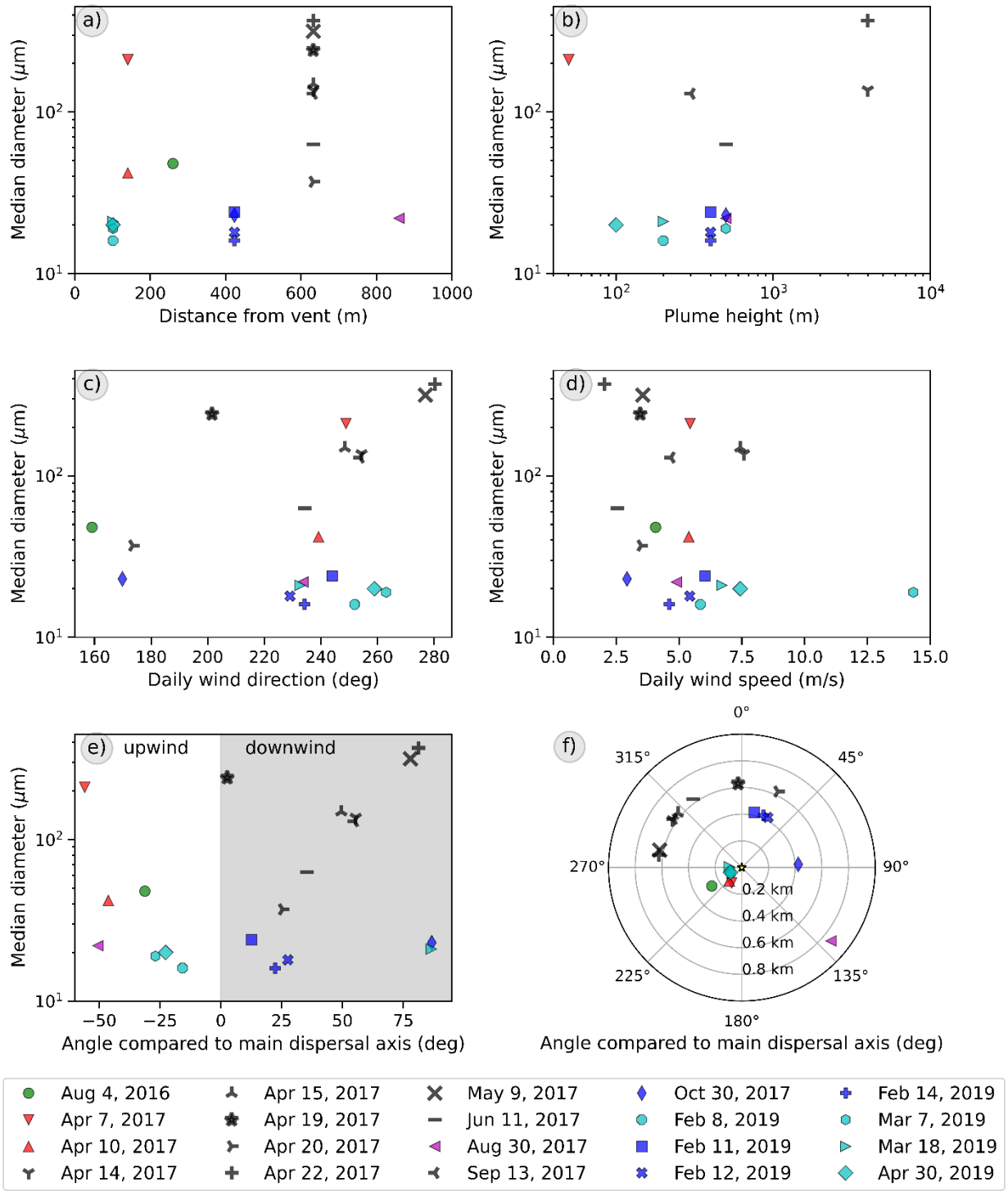

Figure 11. Sample median diameter as a function of parameters related to the explosion and wind. The symbol's color corresponds to the location of sampling (Figure 1). a) Median grain diameter as a function of the distance from the vent in meters. b) Median grain diameter versus plume height. c) Median grain diameter versus daily wind direction. The prevailing wind direction 250+/-25 degrees at Poás. d) Median grain diameter versus daily wind speed. Wind direction and intensity were calculated using NCEP-DOE Reanalysis 2 (Kanamitsu et al., 2002) at an altitude of 200 m above the crater rim. Note that both wind direction and speed do not vary much within the first 4 km above the crater. e) Median diameter versus angle compared to main dispersal axis. Main dispersal axis is zero degrees. f) Median diameter versus angle compared to main dispersal axis and distance from the vent (circles). Main dispersal axis is at zero degrees. The yellow star at the center represents the vent.

4.2 Insights into fragmentation processes

Explosive magmatic fragmentation in the conduit of a volcano produces particles with a size distribution that can be modeled under idealized conditions. When plotted as a cumulative number distribution as a function of size, primary products of magma fragmentation show a power law relationship of the form $N = \lambda d^{-D}$, where N is the number of particles greater than size d, λ is a scaling factor, and D is the power-law exponent (fractal dimension) whose value is in the range 2.5±0.3 (Giachetti et al., 2021; Gonnermann, 2015; Kaminski and Jaupart, 1998; Kueppers et al., 2006; Turcotte, 1997, 1986). On a plot of log(N) vs log(d), D is the slope of the line. If these particles are further re-fragmented via particle-particle collisions or collisions with the conduit sides, not only is their average size reduced, but the fractal dimension of their cumulative size distribution also increases to values larger than 3 (Dufek et al., 2012; Kaminski and Jaupart, 1998)

When plotted as cumulative number distributions, our samples show an exponential distribution over the entire range of sizes that is roughly power-law at small sizes, as shown on Supplementary Figure 4 for one sample of each of the three groups defined based on grain size distribution (see Figure 6). The size at which the distribution first departs from a power-law increases with increasing median grain size diameter; this breakpoint is ~30 μm for the sample of Group 1, whereas the sample from Group 3 exhibits a power-law distribution until about 600 μm (Supplementary Figure 4). For better illustration, we calculated the fractal dimension of the cumulative size distribution over each size fraction <32 μm, 32–63 μm, 63–125 μm, and 125–250 μm for all samples. Both the average and the standard deviation of these four fractal dimensions increase with decreasing median grain size (Figure 12a). The fractal dimension of the cumulative grain size distribution is also linked to the componentry: both the value of the fractal dimension and its standard deviation increase with the proportion of recycled material (Figure 12b).

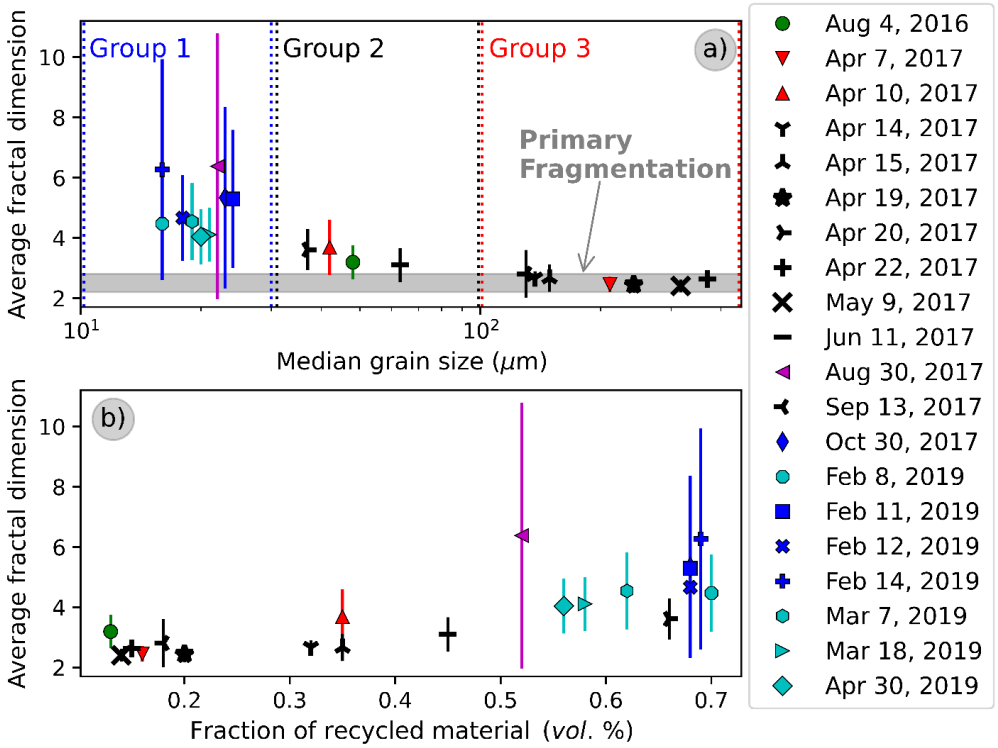

Figure 12. a) Average fractal dimension as a function of median grain size. The standard deviation of the four calculated slopes obtained in the size range 2–250 μm is indicated by the error bars (see text for explanation). Gray rectangle is the region for primary fragmentation. b) Average fractal dimension as a function of the fraction of altered material in the sample with the standard deviation of the four calculated slopes.

Samples dominated by juvenile material. The three samples that are dominated by juvenile material (>66 vol.%; April 22, May 9, and September 13, 2017) and that also contain a rather low amount of recycled material (<20 vol.%) exhibit an average fractal dimension of 2.4–2.9, which is consistent with the primary fragmentation of juvenile magma within the conduit of the volcano, with minimal to no involvement of external water.

Sample dominated by hydrothermal material. The only sample dominated by hydrothermal material, which was collected on August 4, 2016, and contains 60 vol.% of hydrothermal material, exhibits a power law relationship at small sizes with a fractal dimension of 3.2. This is higher than the expected fractal dimension for dry fragmentation of juvenile magma and possibly the evidence of interaction with fluids from the hydrothermal system, creating a more efficient magma fragmentation as suggested by other studies (e.g., Wohletz et al. 2013). This finding also suggests that the external water that interacted with the magma to produce the

observed phreatic/phreatomagmatic explosions likely originated from the hydrothermally altered rock, as we do not see any obvious correlation between the level of the lake and the grain size distribution or fractal dimension (Supplementary Figure 5).

Sample dominated by recycled material. Samples that all have a volumetric fraction of recycled material larger than 50%, also have a fractal dimension >3 (and a small median diameter, all belonging to size Group 3). Together with their reworked edges and loss of most of their luster, this observation strongly suggests that recycled particles are the result of secondary fragmentation of juvenile (or lithic) particles previously deposited. Secondary fragmentation would explain fractal dimension above 3 for samples that contain lots of particles of this type. Extensive alteration and weathering of the erupted material after the eruption, although occurring, is limited in our sample set given the brief period between eruption and collection (<24–48 hours) and overall short eruptive period sampled (~3 years). We thus favor a mostly physical re-fragmentation of previously erupted particles to explain the origin of the 'recycled' material. We observe a greater proportion of recycled material in the 2019 products, suggesting that most of the material deposited during these rather small explosions in 2019 is the result of the re-fragmentation of the 2016–2017 tephra.

All other samples have a more heterogeneous componentry, with sizeable amount of all components, making the interpretation of the relationships between their fractal dimension and their componentry more difficult. We note, however, that samples from April 7, 14, 15, and 19 of 2017, which have similar componentry (10–30 vol.% lithics, 15–35 vol.% recycled, 15–40 vol.% hydrothermal, and 10–30 vol.% juvenile), also have similar fractal dimensions of 2.5–2.7, reenforcing the observation that grain size distribution, fractal dimension, and componentry are intimately related.

4.3 Evolution of Poás eruptive system over the period 2016–2019

Here, we summarize our interpretations of the evolution of Poás eruptive system over the period August 2016–April 2019 (see Figure 13). de Moor et al. (2019) estimated that the total volume of ejected material at Poás between August 2016 and June 2017 was at least 1.5–2.0×106 m3, calculated from drone-based photogrammetry, and that the magma source was shallow, probably <500 m. A large fraction of the volume ejected during this period comes from a single explosion on April 22, 2017, given that it produced a plume of ~4 km above the crater, whereas all other explosions between August 2016 and June 2017 produced plumes that were smaller than 500 m (note that the 4-km-high plume produced by the April 14 eruption was mostly vapor, based on its whitish color). In the following discussion, we assume that: 1) magma rose to a depth of 500 m below the surface by 2016; 2) 2×106 m3 of tephra were ejected between August 2016 and June 2017; 3) 15% of that volume was ejected between 1–14 April 2017 and 80% between April 22 and June 2017 (de Moor et al. 2019); and 4) all other explosions during this period each ejected 1–5% of this total volume. The finding that juvenile particles are present in all ash deposits analyzed over the period of observation indicates the persistent involvement of magma, as opposed to magmatic heat only, consistent with the findings of de Moor et al. (2019). However, our work demonstrates varying degrees of magma involvement with the hydrothermal system through time, with juvenile material representing a wide range of abundance (~10–70 vol.%) in deposits of individual explosions.

In August 2016, the shallow eruptive system of Poás was partially sealed by a semi-permeable hydrothermal seal and the crater was filled with the lake (Figure 13-1). Magma interacted with a well-developed, sealed hydrothermal system above it, leading to explosions forming relatively fine tephra (median grain size of ~50 μm on August 4, 2016) with a fractal dimension of ~3.2. This explosion coincided with a notable but brief increase in SO2/CO2 (de

Moor et al. 2019). Our EMPA data are consistent with an interpretation that the explosion on August 4, 2016, with a plume height <400 m like all explosions during 'phase 2' (de Moor et al. 2019), erupted both 1955 magma and another slightly more evolved composition, either suggesting a more evolved composition (if microlite contents are the same between sets of eruptive products) or a magma that had experienced varying degrees of shallow crystallization. Both chemical compositions accounted as juvenile material, altogether representing 17 vol.% of this explosion. If this explosion accounted for only 1–5% of the total volume ejected during the Aug 2016–June 2017 period and reached the top of the already-emplaced 1955 magma sitting ~500 m below the surface, the equivalent of a cylinder 7–16 m in diameter would have been evacuated by this eruption, carved mostly through the hydrothermal system (64% of the volume ejected) and recycled material from previous explosions (13 vol.%), probably concentrated at the top of the plumbing system, near/at the surface. Conduit evacuation continued in September 2016 and through early April 2017, with conduit widening through the hydrothermal system and increasing amounts of recycled material incorporated from previous explosions, from 13 vol.% in August 2016 to 35 vol.% in early April 2017.

Componentry data show a change starting with the explosions in early-mid April 2017. They marked the start of a long-term decrease in hydrothermal fragments in the explosive products, a higher amount of juvenile material than previously seen, and an increase of the lithic fragments fraction, all leading to a sharp increase in the average ash density from <2300 kg·m-3 in 2016 to >2600 kg·m-3 by April 14. Explosions on April 14, 15, and 19 are similar in terms of the material ejected – and inferred eruptive mechanisms – although variable in terms of plume height (up to 4 km on April 14); ejected ash had a median diameter >130 μm and a size distribution consistent with primary magma fragmentation (fractal dimension of 2.5–2.7, see Supplementary

Table 3), comparably low amount of juvenile material (18–24 vol.%), but a relatively high amount of lithics (20–34 vol.%). We believe that these explosions between April 14–20, 2017, widened the shallow plumbing system via erosion beyond the hydrothermal system, as indicated by the increase in lithic fragments in the componentry. Assuming altogether these explosions accounted for ~20% of the 2×106 m3 of material ejected during the Aug 2016-June 2017 period (de Moor et al. 2019), the ~20 vol.% of lithics found in their deposit would correspond to a volume of 8×104 m3 of host rock removed. We infer that the three explosions on April 22, May 9, and September 13, 2017, represent comparatively 'dry' magmatic activity, based on the high proportion of juvenile material in their deposits (70–72 vol.%) and the paucity in hydrothermal material, consistent with the increase in the role of magmatic gas geochemistry in de Moor et al. (2019), where magmatic gasses reached the surface and drive the eruptions. The explosion on April 22 sampled a new aliquot of previously emplaced magma, characterized by a significantly more evolved groundmass glass composition compared to the 1955 and August 4, 2016, eruptions (Figure 9). Based on photogrammetric data from de Moor et al. (2019), which suggest a conduit diameter of ~50 m at this time, this single event is estimated to have evacuated the conduit over a vertical extent of ~300 m of fresh magma (~800 m if assuming a narrower conduit diameter of 30 m). Despite variable eruptive intensities, with plume heights from 50 m to ~4 km above the vent, the ash ejected by these magmatic explosions on April 22, May 9, and September 13, 2017, consistently shows a rather low amount of recycled (14–18 vol.%) and lithic (5–9 vol.%) materials, and a high density of the particles (2670–2760 kg·m-3) related to a high concentration in juvenile magma, denser than hydrothermal material. There is almost no hydrothermal material present, and the ash has a relatively coarse median diameter (>130 μm). The fractal dimension is consistent with primary fragmentation of the magma in the conduit (2.1–2.9). During this period, the crater lake slowly

disappeared. Altogether, these observations suggest limited water-magma interaction during these three explosions in 2017, with hydrothermally altered rocks that had been largely excavated by earlier explosions, and hydrothermal fluids that had retreated in response to the heat brought by the ascending magma (Figure 13-2). We suggest that the explosions from April 14–20, 2017, finished to 'clear' and widen the conduit and allowed larger batches of magma to reach the surface, with limited reincorporation of previously ejected material (i.e., low recycled material content). This is also substantiated by a large quantity of fresh, glassy degassed bombs ejected on April 14 and breadcrust bombs up to 20 m across on April 22 that remained hot for weeks as observed in thermal images (Brenes-André et al., 2020).

Except for a small explosion on October 30, 2017, which produced very fine-grained ash (23-μm median diameter) mostly consisting of recycled material, the eruptive activity at Poás was minimal after the explosion on September 13, 2017, until February 2019. This absence of eruptive activity allowed the crater lake to refill with water until a new series of explosions started in February 2019 and dried most of lake again (Figure 2). All sampled explosions from February to May 2019 are rather small in size (plume height 400 m or below) and their products exhibit similar size and componentry characteristics: small median diameter (< 24 μm), high average fractal dimension (>4.4), large amount of recycled material (56–70 vol.%), 23–34 vol.% of juvenile material, almost no lithics, and a density lower than in 2017 (2290–2500 kg·m-3). During this period, the lake sporadically filled the vent (Figure 3c) or was not visible (Figure 3d). We believe that the hydrothermal system re-advances toward the conduit and vent when there are periods of quiescence when the lake also reappears (Figure 13-3).

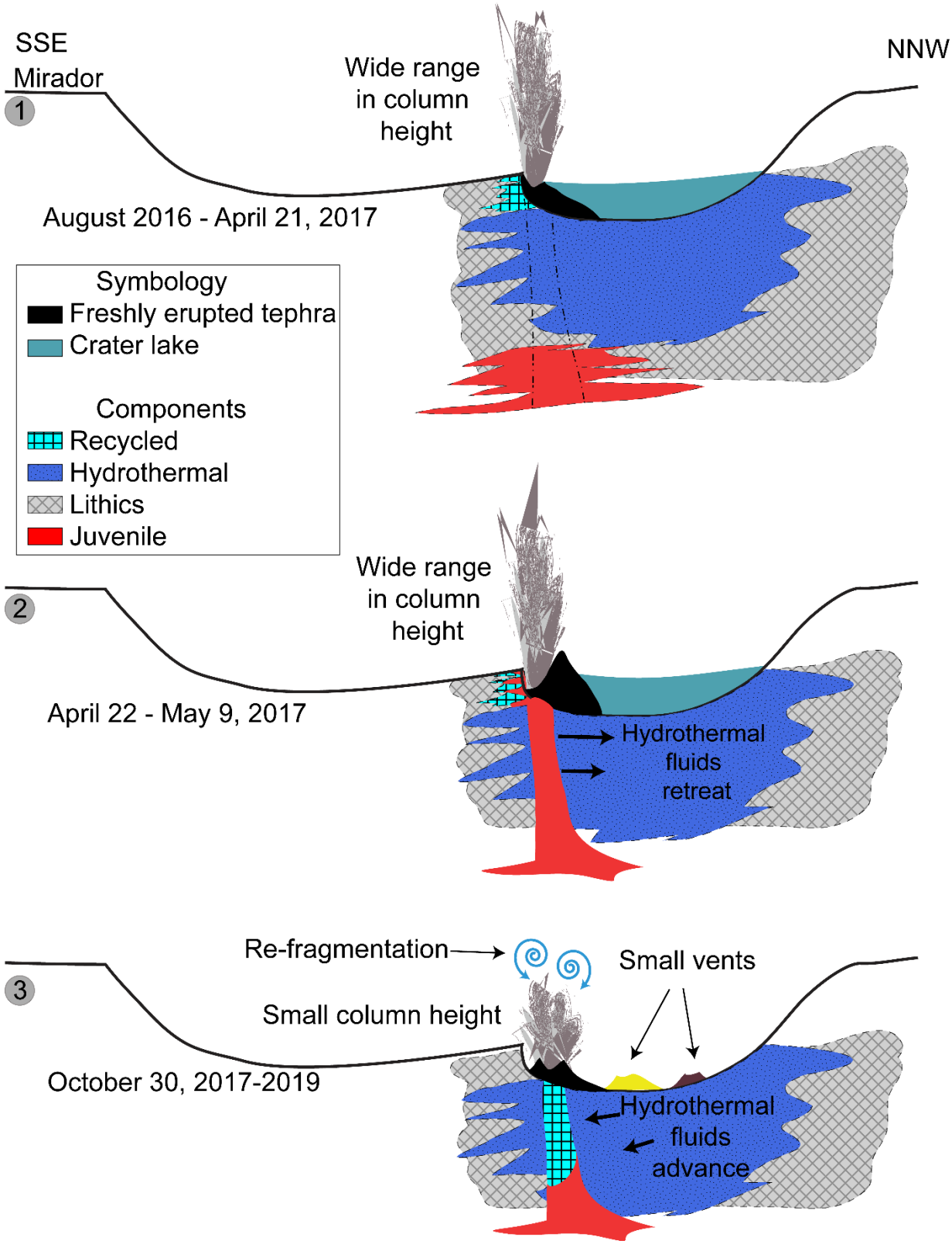

Figure 13. Schematic diagrams showing our interpretation of the evolution of Poás volcano shallow plumbing system between August 2016 and April 2019. See text for explanation.

In 2019, secondary fragmentation played a key role in controlling the grain-size distribution, with explosions probably shallow and small enough for the particles to fall near the vent, re-enter the system, and be re-entrained (and re-fragmented) during the next explosion. Magma input was occurring but was limited compared to 2017, and the system was slowly returning to its pre-August 2016 configuration, with the hydrothermal system rebuilding itself.

4.4 Origin and involvement of magma in the eruptive activity at Poás in 2016–2019

Identifying juvenile material in the deposits of 'wet' eruptions can be particularly difficult when there are fresh-looking fragments from pre-existing material (lithics) that can be wrongly interpreted as fresh magma (Pardo et al. 2014). It is thus possible that some of the glassy particles identified as 'juvenile' in this study are in fact not juvenile magma. However, they do appear pristine and texturally distinct from the unambiguously 'recycled' and 'lithic' material (Figure 4 and Supplementary Figure 2). Chemical analyses of the groundmass glass of six particles identified as 'juvenile' from the August 4, 2016, explosion at Poás revealed that half of them were probably sourced from the same batch of magma as the 1955 eruption. The other half are slightly more evolved, probably through progressive crystallization of the remnant 1955 magma. These lines of evidence provide strong support that juvenile magma was involved as early as August 2016 in the explosions at Poás, even if in limited amounts. EMPA data also confirmed that all particles identified as 'juvenile' in the explosions studied in 2017 and 2019 are indeed fresh magma, validating the observations from componentry analysis.

Although a deeper analysis of the chemical evolution of the magma at Poás since 1955 is beyond the scope of this study, our targeted EMPA analyses show two interesting features. Firstly, the groundmass glass of the juvenile material analyzed for each of the two explosions in 2017 and 2019 is quite homogeneous despite analysis of multiple grains. Secondly, each explosion has its

own compositional signature. This suggests that each explosion tapped a distinct batch of magma, either vertically and/or laterally, with its own crystallization history, whereas the 2016 explosion (based on our limited data) represents a compositional 'hybrid' of 1955 and later erupted products. Given the relatively small size of the explosions in 2019 and their high abundance of non-juvenile material, we infer that the volume of magma tapped in 2019 is much shallower than that sampled in 2016 and 2017. The paucity of chemical data for Poás products in the literature since at least 1955 (except for four whole-rock analyses in Prosser and Carr 1987 and de Moor et al. 2019) precludes further interpretation of our data. Given the comparative richness in geophysical and geochemical data over the same period (e.g., de Moor et al. 2019; d'Arcy et al, 2022; and references therein), further analyses of the chemical evolution of Poás magma would provide even more insight into its shallow plumbing system.

4.5 Ash characteristics and water-magma interactions: beyond Poás

Other volcanic systems, such as Turrialba volcano in Costa Rica, exhibit a transition from early phreatic eruptions dominated by hydrothermally altered lithics to phreatomagmatic eruptions characterized by increasing amounts of juvenile andesitic glass (Alvarado et al., 2016). Similarly, Suzuki et al. (2013) studied the 2011 eruption of Shinmoe-dake volcano in Japan, which followed a progression from phreatic activity (2008–2010) to distinct magmatic eruptive stages. Their detailed analysis of ash samples revealed significant changes in particle composition, whole rock chemistry, and size distribution, marking the onset of juvenile magma involvement and its interaction with external water. These studies underscore the importance of ash analysis, both physically and chemically, to understand transitions in eruption styles and the underlying magmatic processes. Similarly, at Sinabung in Indonesia, Primulyana et al. (2019) showed that ash analysis was pivotal in detecting the transition from hydrothermally driven eruptions to magma-

dominated activity, coupled with the gradual waning of the eruption over time.

5. Conclusions

Poás volcano's current activity has been divided into several eruptive phases since 2006, which marked the beginning of a new eruptive period. We studied the products of twenty explosions from August 2016 to May 2019—we measured grain-size distributions, componentry, particle density, and a targeted subsample of groundmass glass compositions. The deposit grain size and componentry revealed changes in magma-water interaction and fragmentation style. Specifically, the more juvenile-rich deposits were coarser grained (~80 vol.% juvenile, >100 μm), consistent with primary fragmentation in the conduit, whereas the deposits rich in recycled fragments were finer grained (>56 vol.% recycled, <24 μm), consistent with re-fragmentation of pre-existing material. This finding would not have been possible without performing componentry analysis on all available grain size fractions down to 32 microns, which is finer than the typical limit for componentry studies.

Between August 2016 and early April 2017, the abundance of hydrothermally altered particles (weighted average of 65 to 25 vol.%) and small proportion of fresh juvenile material (weighted average of <25 vol.%) suggest that the small explosions were driven by the failure of the sealed hydrothermal system. However, the direct involvement of magma confirmed by chemical analyses indicates that these explosions were phreatomagmatic rather than purely phreatic. As the hydrothermal system progressively dried up due to heat from the ascending magma, explosions in April-May 2017 also began to erode part of the shallow plumbing system, based on increasing proportions of wall-rock lithics. This 'drying' of the system led to three magmatic explosions in April, May, and September 2017. These magmatic explosions produced coarser grained deposits, consistent with primary fragmentation of magma in the conduit and more limited water-magma

interaction. Magma ejected during this 2017 magmatic phase was more evolved than the previous eruptive period in 1953–1955, supporting the suggestion of de Moor et al. (2019) that it represents remobilization of previously emplaced magma. Following this brief magmatic phase, the system returned to a wetter configuration during which small, shallow explosions mainly recycled the deposit of previous explosions in 2019.

This study shows that it is possible to track the opening of a closed volcanic system over months to years through analysis of the ejected particles in context with monitoring data. In particular, the progressive decrease in hydrothermal fragments, combined with an increase in wall-rock lithic material in the tephra deposits reveal the excavation of the shallow hydrothermal system and host rocks, signaling the opening of the conduit. At Poás, this process led to a shift to drier (magmatic) activity, involving coarser grained material with a different range of related hazards. For example, this change in grain size would affect the patterns of volcanic ash dispersal and ashfall model forecasts. Overall, this study emphasizes that petrological monitoring of deposit grain size, componentry, and geochemistry can provide insights into the conceptual model for an evolving volcanic system and inform eruption forecasting efforts.

6. Bridge

Chapter 2 examines the evolution of ash physical properties during the eruptive sequence at Poás volcano from 2016 to 2019. By tracking changes in grain-size distributions, componentry, and particle density across eruptive phases, I showed the transitions from phreatic to phreatomagmatic to magmatic activity, followed by the recycling of previously erupted material. These results demonstrate that ash characteristics can serve as indicators of eruptive behavior, capturing primary fragmentation processes and secondary ones.

This leads us to Chapter 3, where the focus changes to improving the reliability of ash componentry. Here, I employ a multi-imaging approach to treat ash componentry by tracking individual grains across stereomicroscope and SEM analyses, in order to address uncertainties associated with classifying ash particles. This methodology builds on the patterns identified in Chapter 2 and tests how classification and morphological metrics can improve our ability to interpret eruptive processes. Chapter 3 thus strengthens the analytical foundation for using ash componentry as a robust monitoring and interpretive tool for small ash-rich eruptions.

CHAPTER III

3. COMPONENTRY ANALYSIS OF ASH FROM SMALL EXPLOSIVE ERUPTIONS IN THE CONTEXT OF VOLCANIC UNREST: CAN MORPHOLOGY HELP?

1. Introduction

1.1 Importance of petrological monitoring

The goal of petrological monitoring is to examine the solid volcanic products ejected during an eruption to reconstruct the volcanic and magmatic evolution of the system (Re et al., 2021). Volcanic ash petrological monitoring (hereafter referred to as ash monitoring) during volcanic unrest is a critical component of hazard assessment (Alvarado et al., 2016b; Gaunt et al., 2016; Miwa et al., 2013; Primulyana et al., 2019; Taddeucci et al., 2002, 2007). It provides a physical description of the subsurface processes such as evidence of magma ascent, interaction with hydrothermal systems, and eruptive style (Andronico et al., 2009; Cascante et al., 2025; Cioni et al., 2008; D'Oriano et al., 2022, 2011; Liu et al., 2020; Miwa et al., 2009; Suzuki et al., 2013; Watanabe et al., 1999). Ash monitoring consists in rapidly and safely collecting recently erupted material for laboratory characterization of its components and their textures. Ideally, this process is completed as fast as possible (within 24 hours of deposition) to capture syn-eruptive changes and track longer-term trends in volcanic systems (Bernard, 2013; Liu et al., 2020; Miwa et al., 2021). The time-sensitive aspect of monitoring potentially limits the number of analytical tools that can be used, especially those requiring long sample preparation or expensive instrumentation that is not readily available.

Detailed ash analyses, including geochemical, morphological, and textural characterization, are essential for detecting early signals of the presence of juvenile magma and identifying eruptive transitions that may change the associated hazard and associated risk mitigation measures (Cashman and Hoblitt, 2004). These analyses are also crucial to understanding the driving mechanisms of volcanic eruptions and their temporal evolution. The volcanology community has

come a long way to produce and improve standardization of analytical protocols for grain-size, texture, and shape characterization, enabling reproducible and comparable datasets across studies. Componentry analysis of volcanic ash has generally been based on visual classification of particle color, texture, and morphology under binocular microscopy for a certain range of sizes, often supported by Scanning Electron Microscopy (SEM) observations, and geochemical techniques (Alvarado et al., 2016b; Cascante et al., 2025; D'Oriano et al., 2014; Gaunt et al., 2016; Miwa et al., 2013; Pardo et al., 2014; Yaguchi et al., 2022; Yamanoi et al., 2008). In the past two decades, quantitative approaches such as use of shape descriptors or fractal and multivariate analysis have complemented descriptive classifications to capture fragmentation dynamics and eruption evolution (Dellino and Liotino, 2002; Leibrandt and Le Pennec, 2015; Liu et al., 2017, 2015a; Maria and Carey, 2002; Nurfiani and Bouvet de Maisonneuve, 2018). However, most of these studies focus solely on juvenile material and often compare ash shape factors across different volcanoes, eruptions and/or eruptive styles of relatively large eruptions (e.g., Liu et al., 2015; Nurfiani and Bouvet de Maisonneuve, 2018). It remains to be assessed whether measurements of ash shape parameters can be useful during smaller eruptions, for example to rapidly identify juvenile material, help with componentry analysis, or swiftly track changes in ash composition with time.

Additionally, the integration of ash characteristics with geophysical and gas data has demonstrated that petrological monitoring can provide the earliest evidence of fresh magma involvement, particularly during hydrothermal-dominated or low-intensity events where other precursors are ambiguous (Cascante et al., 2025; Gaunt et al., 2016; Miwa et al., 2021; Primulyana et al., 2019). Further, automated image analysis and machine learning are expanding the capabilities of ash characterization, enhancing its potential as a tool for real-time operational

monitoring (Benet et al., 2025, 2024; Shoji et al., 2018).

In volcanoes with active hydrothermal systems, involvement of a juvenile magma may initiate gradually and constitute only a minor fraction of the erupted material at first, making it challenging to distinguish and prone to misinterpretation in visual componentry analyses (Alvarado et al., 2016b; Pardo et al., 2014). In such cases, transitions between phreatic, phreatomagmatic, and magmatic eruptions can be subtle and complex, making it difficult to identify the true progression of eruptive processes. Inconclusive interpretation of the componentry of the volcanic products may delay recognition of escalating hazards, as demonstrated in recent crises at Turrialba (Alvarado et al., 2016b, 2016a; Lücke and Calderón, 2016), Poás (Cascante et al., 2025; de Moor et al., 2019), Shinmoe-dake (Suzuki et al., 2013), Sinabung (Gunawan et al., 2019), Taal (Balangue-Tarriela et al., 2022), and Nevados de Chillán (Benet et al., 2021). Integrating ash monitoring into operational workflows therefore provides a critical forecasting benefit, ensuring that shifts in eruptive processes are identified in time to inform hazard assessments and crisis response.

Ash monitoring plays a pivotal role in developing and refining probabilistic approach of volcanic hazard scenarios in the case of unrest. Event trees are examples of methodologies to estimate the likelihood of volcanic events within predetermined time frames (Newhall and Hoblitt, 2002). Ash data directly informs whether activity is phreatic or phreatomagmatic, and can help characterize potential escalation paths (Wright et al., 2019). In some eruptions glassy, fresh-looking particles could represent recycled pyroclasts, lavas, or material from a recently intruded dike that crystallized shortly before the eruption (Pardo et al., 2014). If fresh juvenile magma identification on the ash deposits is inconclusive the resulting event tree may misrepresent true eruption trajectories. This not only undermines the reliability of probabilistic forecasts but may also delay critical decisions in crisis response. This also underscores the challenges of confidently

identifying fresh juvenile magma in ash deposits. Therefore, rapid, accurate, and high-resolution ash monitoring is essential to correctly parameterize forecasts and enhance early-warning effectiveness in dynamic volcanic environments.

The main goal of this study is to identify whether detailed shape descriptors, or fractal and multivariate analyses of ash particles can help with the rapid componentry analysis during ash monitoring for small explosive eruptions at an opening-system volcano, and thus with the identification of the onset and evolution of magmatic involvement. We used four eruptions in 2014–2016 at Turrialba volcano, Costa Rica, as a case study. Componentry realized using a stereomicroscope alone has long been recognized as prone to misinterpretation, potentially leading to incorrect conclusions about eruptive processes (e.g., Alvarado et al., 2016b; Cashman and Hoblitt, 2004; Pardo et al., 2014). While Scanning Electron Microscope (SEM) and Energy Dispersive Spectrometry (EDS) analyses have been widely incorporated to refine ash componentry, few studies have directly tracked the same clast though different imaging techniques. To address this challenge, we imaged hundreds of individual particles using multiple methods—stereomicroscopy, SEM Secondary Electron (SE) surface imaging, and SEM Backscattered Electron (BSE) imaging of polished sections through particles—tracking their appearance and shape parameters across all three techniques. By integrating detailed componentry classification with quantitative shape analyses following (Liu et al., 2015a) and (Nurfiani and Bouvet de Maisonneuve, 2018), the results help refine operational petrological monitoring approaches and provide guidance for hazard assessment strategies during volcanic crises, particularly systems where early magmatic signals are subtle and easily overlooked.

1.2 Turrialba volcano

Turrialba volcano is in the southeastern Central Volcanic Range of Costa Rica, where the

Cocos Plate subducts beneath the Caribbean Plate (Figure 14). Its geological history begins ~1 Ma ago with the Proto-Turrialba, followed by the Paleo-Turrialba (600–250 ka), and its most recent stage is Neo-Turrialba (started ~250 ka). Its eruptive products range from basalt to dacite, with basaltic andesites and andesites being the most common (Alvarado and Gans, 2011; Di Piazza et al., 2019, 2015; Reagan et al., 2006; Ruiz Cubillo, 2012). Its crater alignment and structural evolution are controlled by NE-SW and NW-SE strike-slip fault systems (Calvo et al., 2019; Soto, 1988). Reagan et al. (2006) found at least ten eruptions in the past 7,000 years, with the last historic event in 1864–1866. New unrest began in the late 20th century (Martini et al., 2010; Tassi et al., 2004; Vaselli et al., 2010), leading to phreatic, phreatomagmatic, and magmatic activity from 2010 onward, culminating in a persistent open-vent system between 2016 and 2019 (Alvarado et al., 2016a, 2016b; de Moor et al., 2016a; Lücke and Calderón, 2016; Mick et al., 2021; Moussallam et al., 2014; Rizzo et al., 2016; Stix, 2018; van der Laat et al., 2022). Magma origin during this unrest involves multi-stage mixing of back-arc and arc type geochemical signatures, predominantly trachyandesitic to trachydacitic compositions, and occurrence of a rhyolitic magma, with storage in deep (~13 km), mid-crustal (5–10 km), and shallow (1–2 km) reservoirs (de Moor et al., 2016a; DeVitre et al., 2019; Di Piazza et al., 2015).

Turrialba volcano is a great example of a slow reawakening that started with isolated yearly eruptions from 2010 until 2014 (Stix, 2018; Stix and de Moor, 2018), to periods of eruptions phases (2014–2017), followed by open vent ash emissions (i.e., quasi-continuous eruptive activity; van der Laat et al., 2022). This eruption cycle has been well documented via multiple monitoring techniques, allowing correlations across approaches (de Moor et al., 2016a; Rizzo et al., 2016; van der Laat et al., 2022). However, the moment when the new juvenile magmatic component reached the surface is still not well defined.

During its 2014–2016 activity, ash deposits at Turrialba volcano experienced a progressive shift from dominantly hydrothermal material to compositions increasingly enriched in altered clasts, and ultimately to deposits containing a higher proportion of juvenile components (Alvarado et al., 2016b, 2016a; Lücke and Calderón, 2016; Rizzo et al., 2016; Stix and de Moor, 2018). According to Lücke and Calderón (2016), early eruptions in 2014 produced ash composed of altered lithics and hydrothermal minerals, reflecting phreatic fragmentation. Alvarado et al. (2016b, 2016a) proposed that juvenile material was present from the beginning of this eruption cycle in 2010, they also emphasized that the magma composition was similar to the 1864–1866 activity (de Moor et al., 2016a; Di Piazza et al., 2015; Reagan et al., 2011). Rizzo et al. (2016) found potential fresh juvenile material in the ash products in May 2015 eruptions, and de Moor et al. (2016a) marked the onset of phreatomagmatic activity by mid–2015, based on shifts in gas compositions. The first unequivocally direct evidence of fresh magma reaching the surface was when lava bombs were observed in deposits during the 2017 eruption (Stix, 2018; Stix and de Moor, 2018).

The relationships between the surface, external morphology, and internal textures of ash particles are still poorly constrained, although these are crucial, particularly in low-energy or hydrothermal-dominated systems where the occurrence and origin of juvenile-looking material may be ambiguous. The relatively high frequency of monitoring and ash sampling during the eruption cycle of 2010–2021 eruption cycle makes Turrialba volcano an ideal case to investigate changes in ash componentry and textural and morphological indicators and assess how early involvement of juvenile magma can be detected via ash monitoring during an eruption sequence.

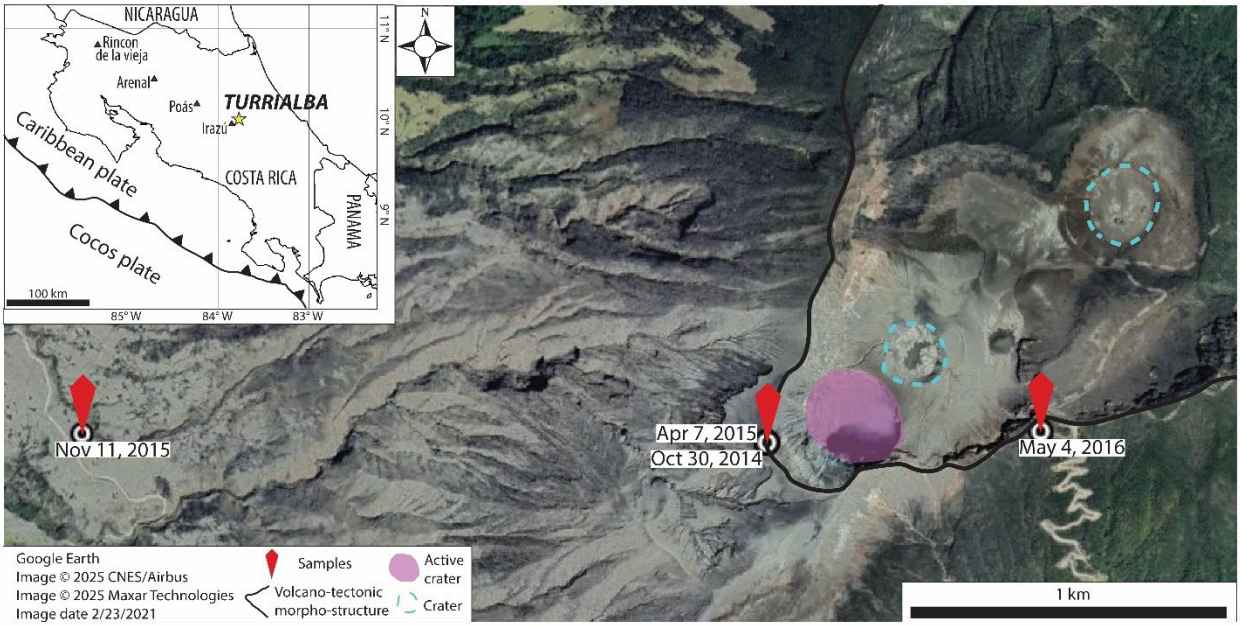

Figure 14. Map of Turrialba volcano location and satellite image with the location of samples and active crater.

2. Methodology

The overall methodology consists in 1) collecting fresh ash samples from Turrialba volcano throughout the 2014–2016 period that is pivotal in terms of type of volcanic activity, 2) completing two types of componentry, 2.1) documenting componentry and gathering shape factors of several hundred 250–500 µm grains of each ash sample through a camera-mounted stereomicroscope, and 2.2) quantifying relative proportion componentry for each eruption with random aliquot of the sample, 3) gathering the same shape factors on the same grains using a SEM on both projected area (SEM-PA) and cross-sectional (SEM-CS) area of the grains (i.e., similar to Liu et al. (2015a)), 4) ensuring that the original assigned component remained valid after grains had been observed in SEM-CS, as misinterpretation is possible (Alvarado et al., 2016a) to finally 5) compare all parameters throughout imaging techniques and establish a methodology to rapidly and accurate perform ash componentry analysis, potentially with the help of particle shape parameters.

2.1 Samples

To characterize the evolution of the abundance of juvenile magma during the 2014–2016

eruptive activity of Turrialba volcano, we sample and analyzed four key eruptions on October 30, 2014 (plume height 4 km), April 7, 2015 (plume height 2 km), November 6, 2015 (plume height 1 km), and May 4, 2016 (plume height 0.5 km). These eruptions were chosen because they represent critical intervals when it remained unclear whether juvenile magma had reached the surface. All sampling locations were within 2 km of the active vent (Figure 14). Ash samples vary from about 0.1–0.5 kg and were typically collected within 24 hours and no more than 48 hours after the eruptions that ejected them. Because of the short collection time after the eruption, we do not believe the alteration of our samples to be post-eruptive. Plume height was estimated by the Costa Rican Volcano Observatory (Observatorio Vulcanológico y Sismológico de Costa Rica - OVSICORI) via webcam image analysis ("Informes Técnicos," n.d.).

Samples were subdivided into aliquots of several tens of grams using a mechanical splitter to preserve representativeness. Each aliquot was then wet sieved in whole φ intervals, where $\varphi = -\log_2(d)$ and d is the particle's equivalent diameter in millimeters. Material was finally dried in an oven at ~65 °C for 12 to 24 hours before analysis. We focused on the medium ash grain-size fraction (250–500 μm) because it commonly preserves air-quenched volcanic glass and is large enough to allow for both observation under most stereomicroscopes and for rapid preparation for SEM analysis (Liu et al., 2015a), making it suitable for monitoring purposes.

2.2 Imaging the particles

Each particle was first photographed under a stereomicroscope at a constant magnification and catalogued with a unique identification number (Section 2.2.1). Particles were then mounted onto a glass slide using double-sided carbon tape suitable for SEM surface analysis (Figure 15) and their projected area was acquired in Secondary Electron mode (Section 2.2.2). Afterwards, we embedded the glass slide in epoxy resin, cured, and subsequently polished the slide to analyze the

cross-sectional area internal structure of the particles by SEM, using backscattered electron (BSE) imaging (Figure 15, section 2.2.3).

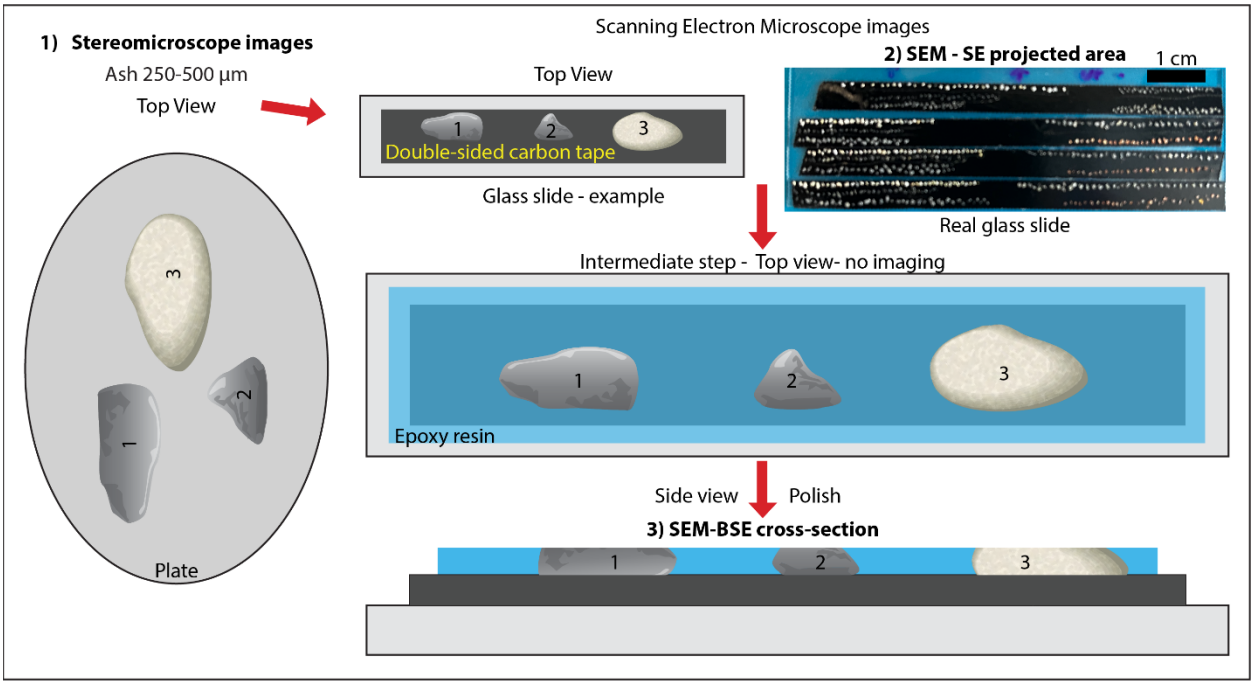

Figure 15. Diagram of our methodology for stereomicroscope and SEM imaging. Imaging steps include 1) stereomicroscope imaging in plane polarized light (PPL), 2) secondary electron (SE) imaging of grain surfaces, and 3) back-scatter electron (BSE) imaging of sectioned grains.

2.2.1 Stereomicroscope and componentry analysis

To approximate the traditional observatory approach, we identify different components to classify the types of particles found in the ash samples. The component classification (i.e., componentry) was based on qualitative observations of the color, shape, and luster of the particles observed under the stereomicroscope. Shape was defined by the degree of edge and surface roundness. Particles with predominantly rounded edges were classified as *rounded*. Particles showing a mixture of rounded and angular edges were termed *subrounded*, whereas particles lacking any rounded edges were described as *sharp*. Luster was assessed according to surface shine, following terminology adapted from D'Oriano et al. (2014). Particles with a high, continuous sheen were labelled as *glassy*, those displaying localized or patchy shine were termed

glittery, and those lacking visible sheen were described as *dull*. We tried to keep the intensity and orientation of the stereomicroscope lights constant across all observations. Together with the color of the clasts, shape and luster were then used to define the following five components (Figure 16a):

- **Juvenile**: Dark or transparent particles, glassy sheen, sharp edges.
- **Altered**: Dark particles, glittery sheen, subrounded edges.
- **Hydrothermal**: White to yellow/orange dull particles, rounded to subrounded edges.
- **Lithic**: Gray dull particles, subrounded to sharp edges.
- **Red**: Particles exhibiting a distinctly red color, which do not overlap with other categories. These particles were absent from the 2016 eruption, but present in all three other eruptions. As seen later, each red particle can be re-classified as one of the other four components once observed under the SEM.

For each eruption, we then quantified the proportion of the different components by sorting 375–475 randomly chosen 250–500-µm grains in one of the five categories listed above. Separately, we handpicked at least 25 individual particles of each component in each eruption to study their change in appearance and shape across the three imaging techniques (Figure 15; Figure 16). To reduce bias during these steps, two separate operators handpicked the grains and categorized them.

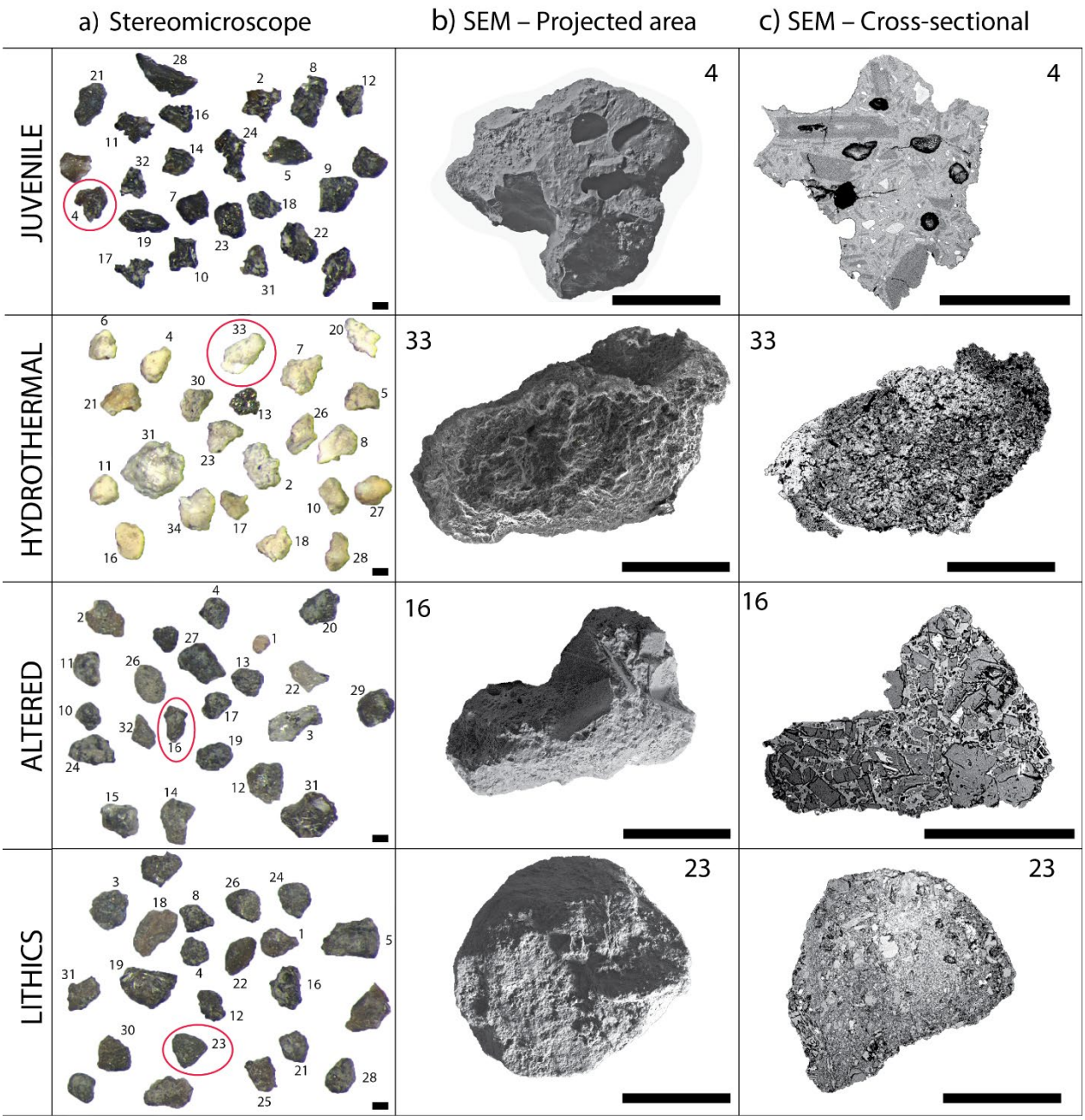

Figure 16. Main components of the ash particles of our study. Scale bars are always 200 µm. For each component, the circled particle is also shown in SEM projected area (SEM-PA) and SEM cross-section (SEM-CS). All particles come from sample May 4, 2016.

2.2.2 SEM - Projected area (SEM-PA)

Particles were mounted on a double-sided carbon tape and then carbon-coated prior to SEM imaging for external surface descriptions and shape factor analysis. We used Secondary Electron (SE) imaging on a ThermoFisher Scientific Apreo 2 SEM at 10 kV accelerating voltage, 1.6 nA beam current, and a 10 mm working distance. Analyses were conducted at the Center for

Advanced Materials Characterization in Oregon (CAMCOR), University of Oregon.

We chose an arbitrary scale from 0–3 to semi-quantitatively describe the particle surface 'roughness', where the surface of the particle is given a 0 if it appears smooth (i.e., large wavelength of the texture topography) and a 3 if the surface is rough and irregular (Figure 17). We added another description for the edges of the particle and assigned 0 if all the edges appeared round, 1 if they were subrounded, 2 for rugged or irregular, and 3 for sharp (Figure 17).

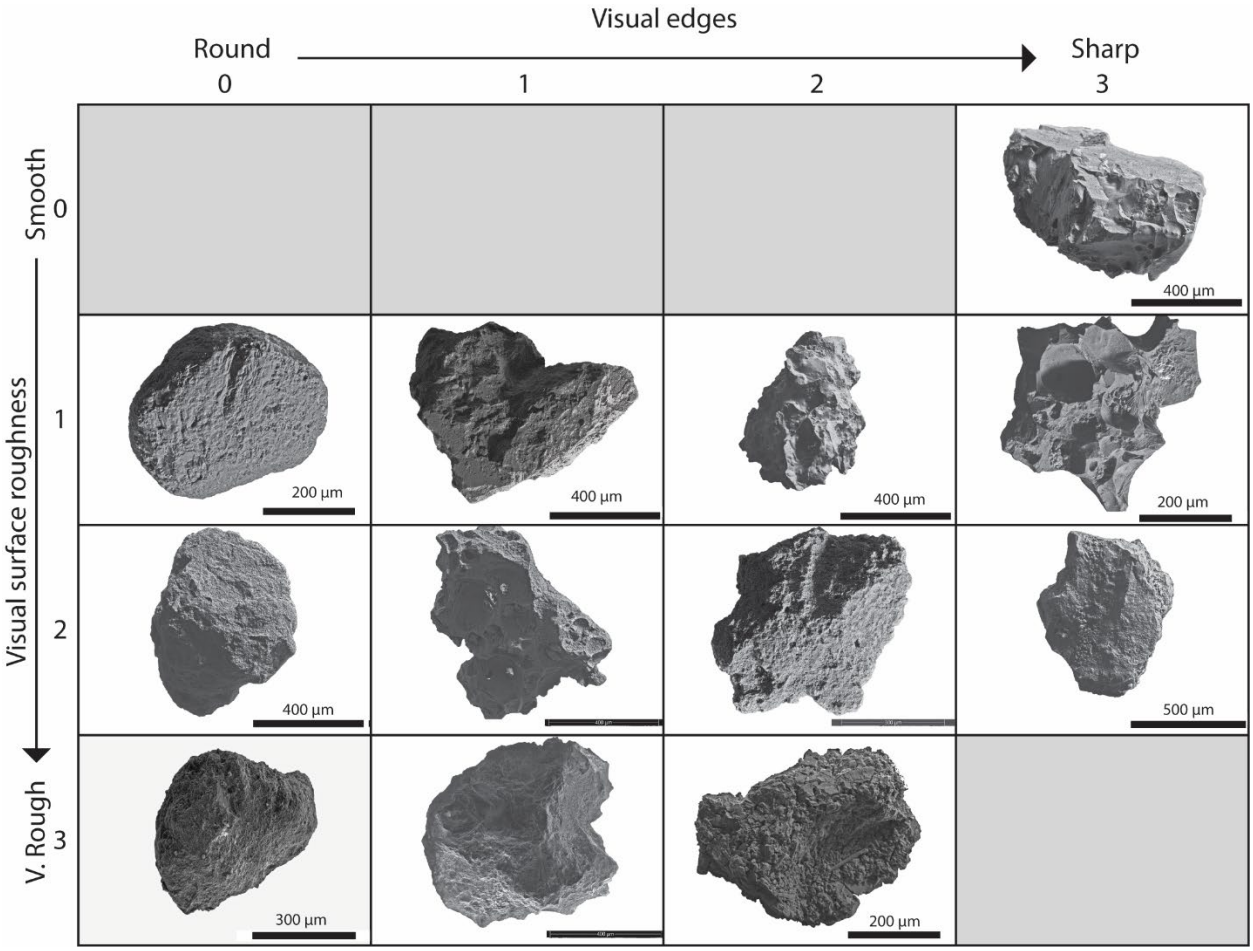

Figure 17. Semi-quantitative estimate of the roughness of the surface and edges of particles based on visual inspection of SEM-PA images. Particles shown here are a mix of all components and eruptions.

2.2.3 SEM - Cross-sectional (SEM-CS)

After imaging all intact particles using the SEM (SEM-PA), we added epoxy resin to glass slides and polished all grains to expose a cross-sectional view of each grain. The cross-section of

the particles was imaged using the same SEM in BSE mode to investigate internal structures, textures, and to identify mineral and glass alteration. For each juvenile, altered, and lithic grain, the intensity of alteration of both the glass and crystals present in each grain were independently quantified using a semi-quantitative scale (0–3), where 0 means no alteration and 3 corresponds to an advanced alteration (Figure 18). Note that for hydrothermal particles, the whole particle is completely altered to an extent that original glass and crystals were not easily recognizable, if at all, and were assigned a 4 on both scales by default.

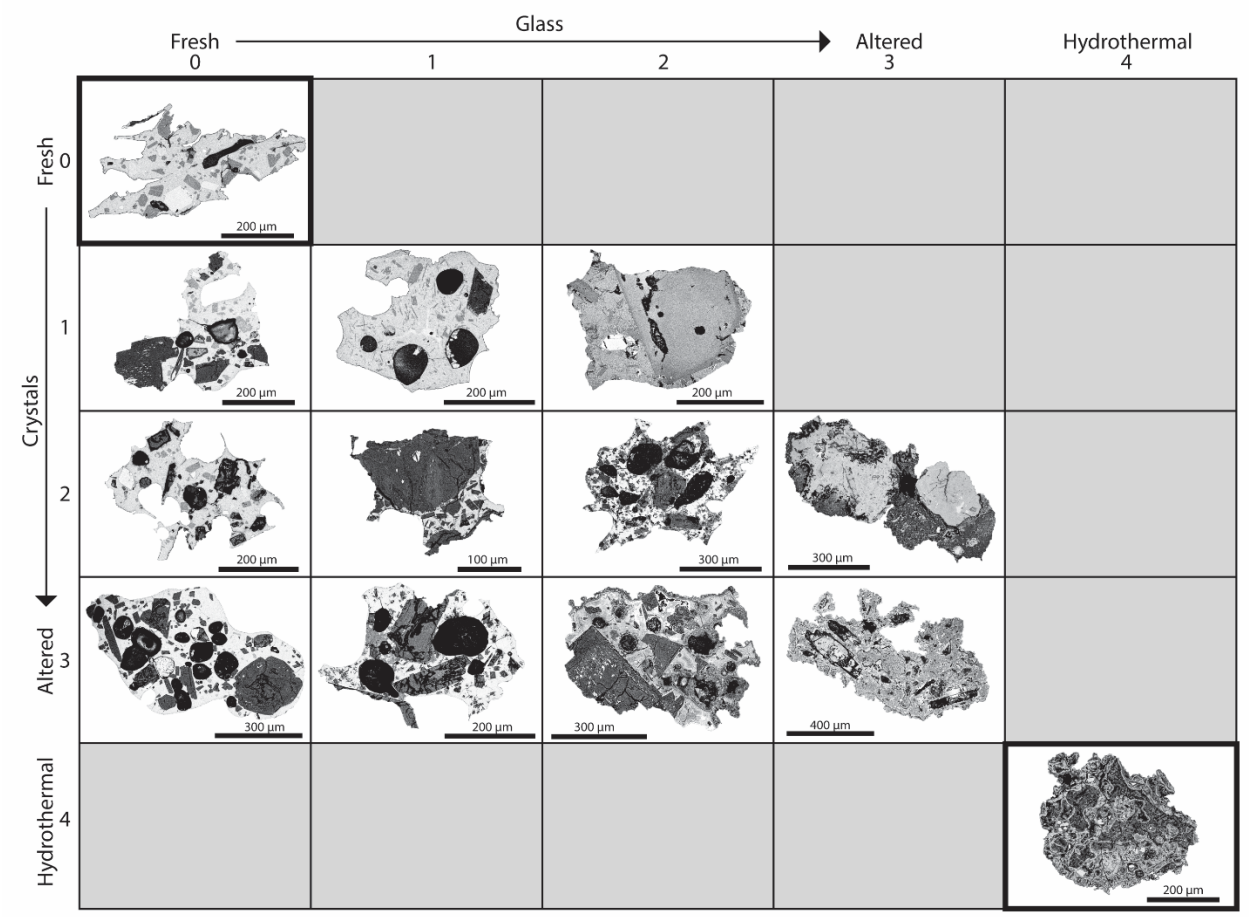

Figure 18. Semi-quantitative alteration scale used for classifying ash particles, with alteration of the glass in the x-axis and of the crystals in the y-axis. Note that a juvenile particle has a 0 on both axes, whereas a hydrothermal particle has a 4 on both axes. Intermediate values correspond to an altered particle.

We also used cross-sectional SEM images (SEM-CS) to reclassify particles, thus

potentially correcting any misinterpretation originally based solely on stereomicroscope observation (e.g., a 'juvenile' particle under the stereomicroscope showing alteration of its glass and/or crystal under the SEM was re-categorized as an 'altered' particle). This step also allowed us to classify each 'red' particle from the 2014 and 2015 eruptions as either a juvenile, altered, lithic, or hydrothermal particle.

2.3 Morphology

To quantify particle morphology, we followed the shape analysis protocols optimized by Liu et al. (2015) and Nurfiani and Bouvet de Maisonneuve (2018). For each eruption sample (October 30, 2014; April 7, 2015; November 6, 2015; and May 4, 2016), we measured shape parameters on 118–150 individual particles to ensure statistically representative datasets (545 particles analyzed in total).

Figure 19 shows all three types of images (stereomicroscope, SEM-PA, and SEM-CS) for a randomly chosen particle and the shape parameters calculated using those images. We first generated binary images of the particle and then we measured the particle area (A_p), perimeter (P_p), convex hull area (A_h), convex hull perimeter (P_h), and the major (A) and minor (B) axes of the best-fit ellipse. Following these measurements, we calculated the four shape descriptors, solidity ($S = A_p / A_h$), convexity ($C = P_h / P_p$), axial ratio (AxlR = B / A), and form factor ($FF = 4\pi A_p / P_p^2$), which have been shown to capture the majority of morphological variance in volcanic ash (Liu et al., 2015; Nurfiani and Bouvet de Maisonneuve, 2018). Normalization of these parameters between 0 and 1 allows for a direct comparison among samples and descriptors. Co-variation in solidity and convexity is particularly useful for distinguishing juvenile clasts from dense lithic fragments, while axial ratio and form factor provide complementary constraints on particle elongation and edge irregularity (Liu et al., 2015a).

Following Nurfiani and Bouvet de Maisonneuve (2018), we further applied fractal perimeter analysis to capture the multi-scale roughness of the particle outlines. We first computed the Euclidean Distance Transform of the binarized image of each particle. We then binarized the EDT from the particle boundary at distance intervals of $\varepsilon_i = 2^i$, where i is the iteration number (from 1 to 4). The width ε_i and the area, $A(\varepsilon_i)$ of the dilated boundary were calculated at every iteration and the fractal dimension calculated as FD = 2-α, where α is the local slope of the curve $A(\varepsilon_i)$ as a function of ε_i when plotted on a double logarithmic scale (see Fig. 2 of Nurfiani and Bouvet de Maisonneuve, 2018; see also Maria and Carey, 2002). We used 4 iterations from i=1 to i=4 to give four individual FD per particle, and per type of image.

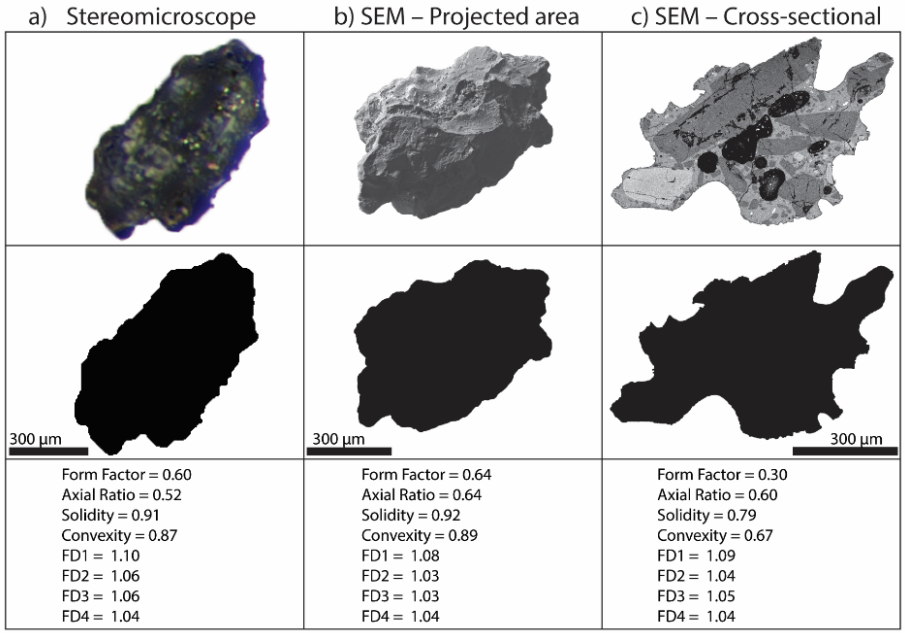

Figure 19. Example of one particle shape analysis using images taken via stereoscope (left), SEM-PA (center) and SEM-CS (right), together with, the values of the four main shape factors used by Liu et al. (2015a) and those of the four first fractal dimensions obtained following Nurfiani and Bouvet de Maisonneuve (2018).

3. Results

3.1 Componentry

Stereomicroscope-based classifications show that all the samples have roughly similar componentry at the 250-500 µm fraction (Figure 20). They are dominated by hydrothermal (37–

57%) and lithic (27–40%) particles, with altered material accounting for another 12–20% of the sample. The stereomicroscope-based componentry suggests that juvenile components are present as early as 2014 in the eruptive sequence (Figure 20), even if representing a very small proportion of the ash sample at this size fraction (1% in 2014, and then up 3% in 2015 and 2016).

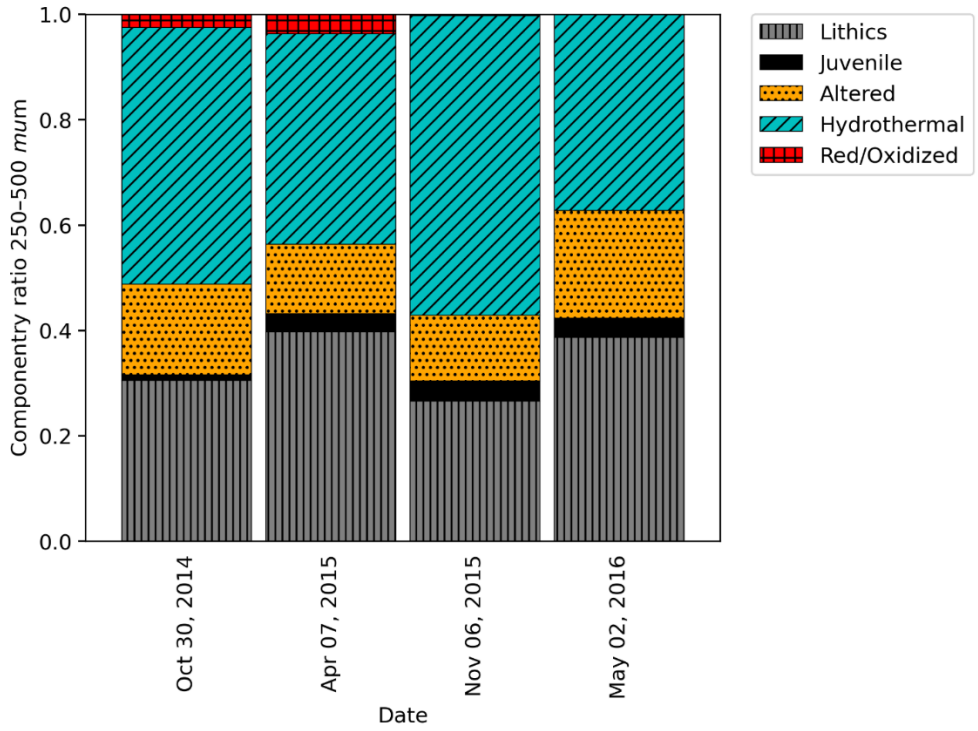

Figure 20. Componentry realized on the 250–500 um fraction of samples from four eruptions between 2014 and 2016, based on stereomicroscope images.

Our analyses show how particles classified as 'juvenile' (i.e., appearing fresh and glassy) under the stereomicroscope, and even on the SEM-PA images, show signs of alteration when their polished cross-section is observed under the SEM. Alteration was observed in the groundmass glass and within crystals (microlites, microphenocrysts, and/or phenocrysts) in a significant fraction of the juvenile fragments. This discrepancy is highlighted in Figure 21 that presents confusion matrices whereby the classification based on stereomicroscope images is compared with that made using the SEM-CS images that we consider give the 'true' (correct) componentry.

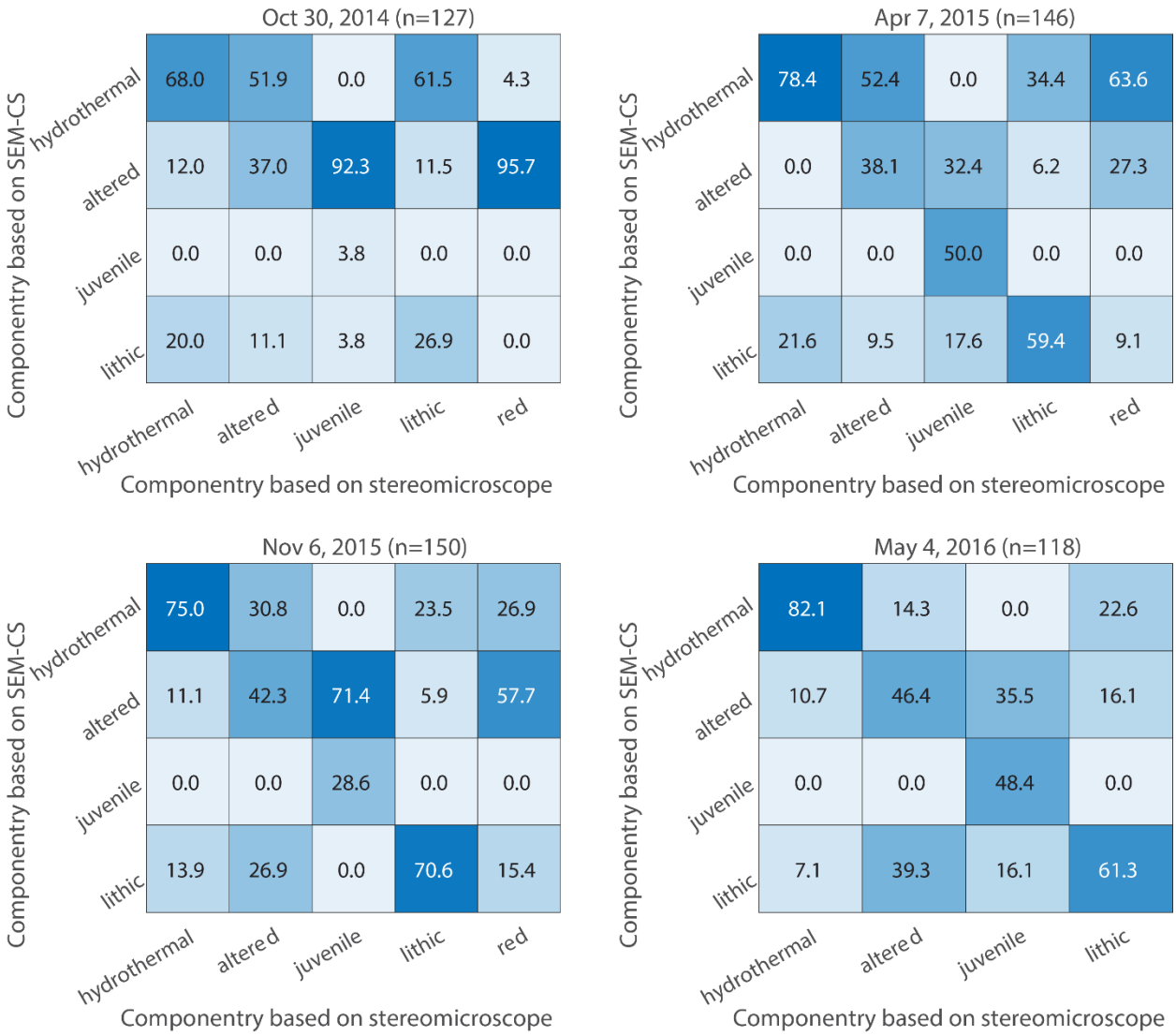

Figure 21. Comparison of the componentry based on stereomicroscope and SEM-CS for the four eruptions studied.

We applied two different criteria to classify a particle as 'juvenile' to evaluate how allowing for limited alteration can impact our componentry results:

Classification with no alteration of the glass and nor the crystals whatsoever in juvenile particles (middle bar in Figure 22)

This classification only considers particles as juvenile if they are alteration free (i.e., Glass = 0 and Crystals = 0 in the alteration scale; see Figure 18). This criterion excludes any particle that shows internal alteration. This is the most conservative definition of 'juvenile' ensuring we only

count pristine material.

Classification accounting for light alteration of glass and/or crystals in ‘juvenile’ particles (right bar in Figure 22)

Some studies classify particles as juvenile even if they show a slight alteration (Gaunt et al., 2016). Following this approach, we reclassified as ‘juvenile’ particles that have alteration values ≤1 on the glass and crystal in the alteration scale (Figure 18). This allows the inclusion of slightly altered juvenile fragments while excluding strongly altered or hydrothermal material.

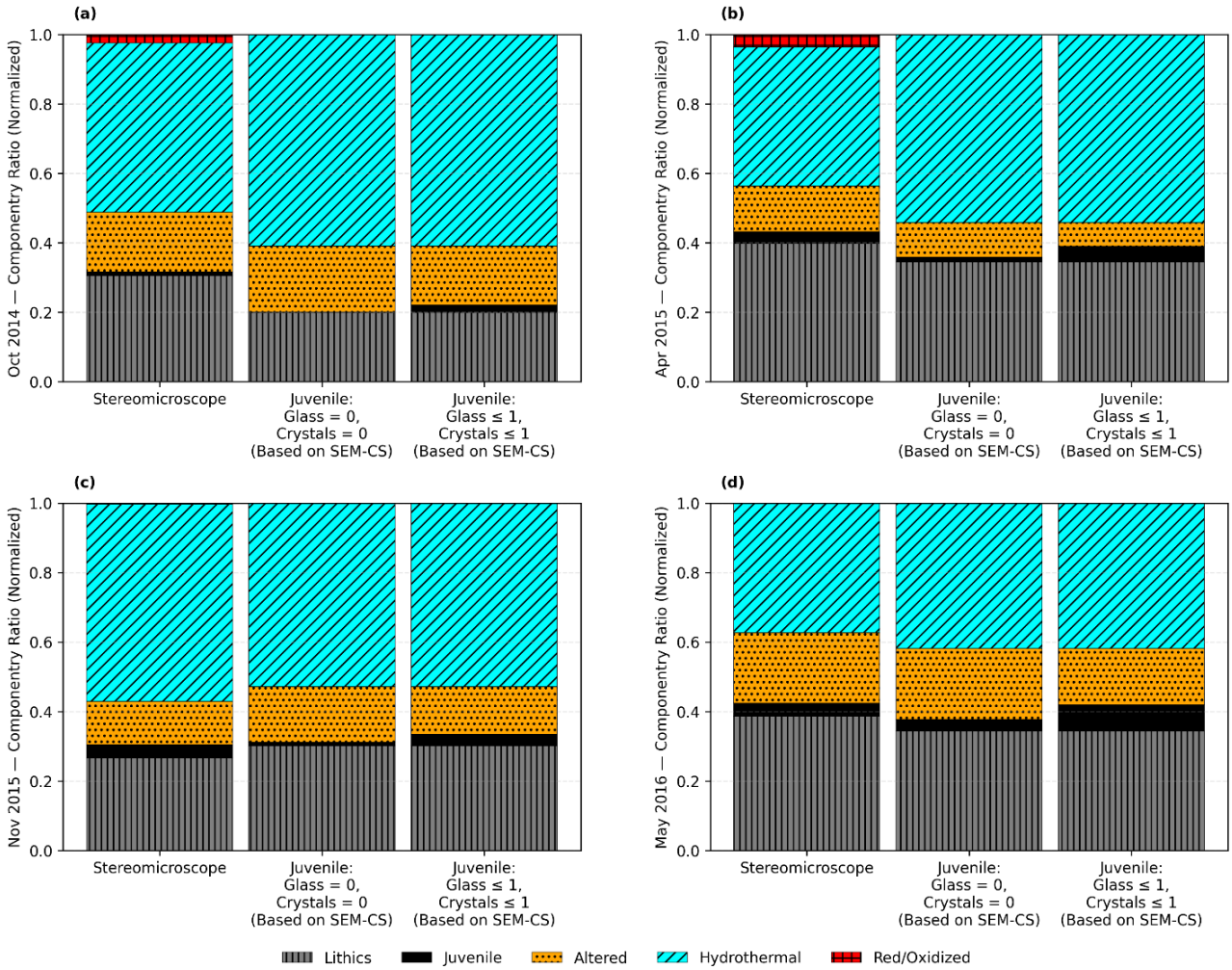

*Figure 22. Componentry comparison of the 4 eruptions using three classifications. 1. **Left bar**: Original componentry classification. 2. **Middle bar**: Juvenile component including only particles with no alteration (Glass = 0, Crystals = 0). 3. **Right bar**: Juvenile component allowing minor alteration (Glass ≤ 1, Crystals ≤ 1). (a) Componentry percentage for the Oct 30, 2014, eruption (b) Apr 4, 201,5 eruption (c) Nov 11, 2015, eruption and (d) May 5, 2016, eruption.*

Figure 21 is an example of the confusion matrix used based on our classification of with zero alteration allowed on glass and crystals juvenile particles. Overall, based on the classification with zero alteration allowed on glass and crystals juvenile particles, the SEM-CS demonstrate that stereomicroscope observations systematically overestimate the proportion of juvenile material. In total, of the 119 particles identified as 'juvenile' under the stereomicroscope, 78 (i.e., 66%) were reclassified as another component when inspected using SEM-CS images. Misclassified 'juvenile' were in fact 'altered' (85%) or 'lithic' (15%), but never 'hydrothermal'. For example, in the 2016 eruption, 48% of the 'juvenile' material remains 'juvenile' after inspection on SEM-CS images, whereas 36% have been re-classified as 'altered' and 16% as 'lithic' (Figure 22). Thus, importantly, the amount of 'juvenile' particles determined by the stereomicroscope always represents a maximum, as no additional 'juveniles' were identified by SEM analysis. The red particles, which represent 17% of the componentry in 2014 and 2015 (<1% in Nov, 2015, and absent in 2016), are a mix of 'altered' (27–96%), hydrothermal (4–64%) and 'lithic' (0–15%) particles, when observed in SEM-CS (Supplementary Figure 6).

We used confusion matrices comparing our classifications (stereomicroscope-based and SEM-CS-based) to derive correction factors and re-calculated the true componentry of the 250–500-µm fraction of each eruption (Figure 22). Altogether, the SEM-CS-based componentry shows only minor differences from the stereomicroscope-based componentry, mainly because the number of particles identified as juvenile under the stereomicroscope (the most often misclassified type of particle) is very low to begin with. Importantly, however, after this correction has been applied, the Oct 2014 eruption re-classified componentry loses the juvenile particles altogether (Figure 22a, middle bar).

3.2 Morphology

We produced several sets of shape descriptors: a semi-quantification of the surface and edge roughness based on inspection of the SEM images of the projected area (Section 2.2.2), and a quantification of the convexity, axial ratio, solidity, form factor, and a fractal analysis of each particle for each of the three imaging techniques (Section 2.3). We first compare our semi-quantification of the surface and edges roughness of the particles with the componentry, before investigating whether a detailed quantification of shape parameters could help differentiate components and thus accelerate componentry analysis.

3.2.1 Surface and edge roughness vs. componentry

We classified components under the stereomicroscope using a combination of color, luster, and shape of each particle into one of the four original component categories (juvenile, hydrothermal, altered, lithic; we do not use the 'red' category here because of its reclassification). The roughness of the surface and edges of each particle was then estimated using its SEM-PA image (values 0–3, see Figure 17) and, if needed, the particle was finally re-classified in its 'true' component category after examination of its SEM-CS image. Section 3.1 showed that the componentry based on stereomicroscope images alone can lead to an overestimation of the juvenile componentry by 67–2400% because of misclassification of particles (Figure 21). The goal of this section is to examine whether the true nature of a particle, as determined using the cross-section image, can be assessed relatively rapidly using a semi-quantification of the roughness of both its surface and edges using SEM-PA images, without having to embed particles in resin and polish them, which is time-consuming and thus not ideal from a monitoring perspective.

Figure 23 shows that juvenile particles tend to exhibit smoother surfaces (average index of 1.31±0.47 on averages) and sharper edges (2.58±0.73) compared to other components, reflecting angular or fractured boundaries. Altered particles, which are juvenile particles that endured some

alteration of their glass and/or crystals, have slightly more rugged surfaces (1.70±0.6) and smoother edges (1.72±0.85), whereas hydrothermal clasts have smooth edges (1.34±0.71) and even more rugged surfaces (2.36±0.55). It is interesting to note that from juvenile to altered to hydrothermal, overall, there is a smoothening of the edges of the particles (2.58>1.72>1.34) and an increase in the roughness of the surface (1.31<1.70<2.36), which is expected if we interpret them as a spectrum of post-eruptive modification. Lithics have intermediate surface roughness (1.95±0.60) and the smoothest edges, on average (1.24±0.78). These distributions show that the roughness of the particles' surface and edges can help discriminate more effectively between component types, but, given the large overlap between the distributions of all components, cannot be used as a standalone technique to classify individual particles.

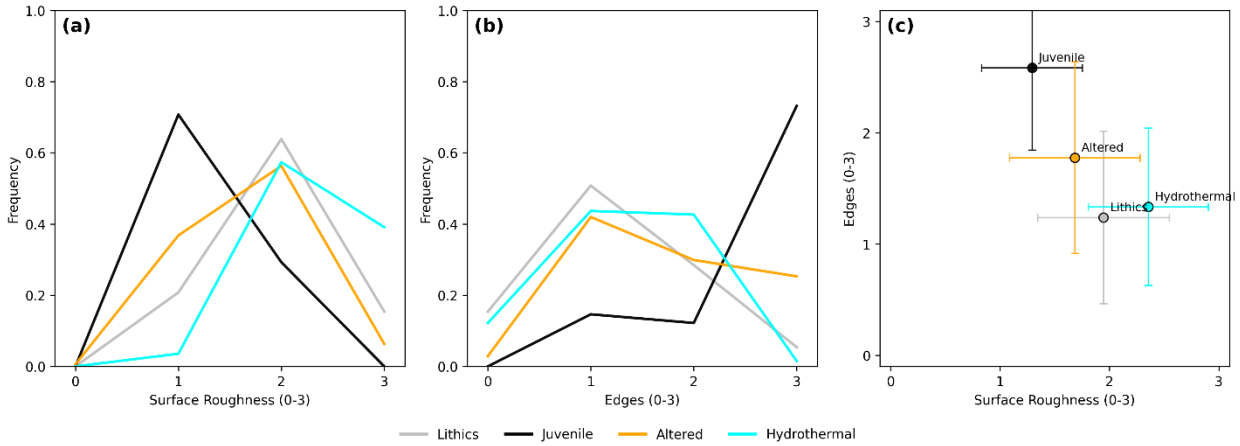

Figure 23. Visual (a) surface roughness, (b) edges from SEM-SE, and (c) average (± St. dev.) roughness vs. edges for each component.

3.2.2 Shape parameters

We calculated shape parameters across the three imaging approaches, allowing direct comparison of the componentry with the morphological features of particles. Comparisons of shape descriptors using frequency distributions (Figure 24a) and cumulative curves (Figure 24b) highlight consistent differences among methods.

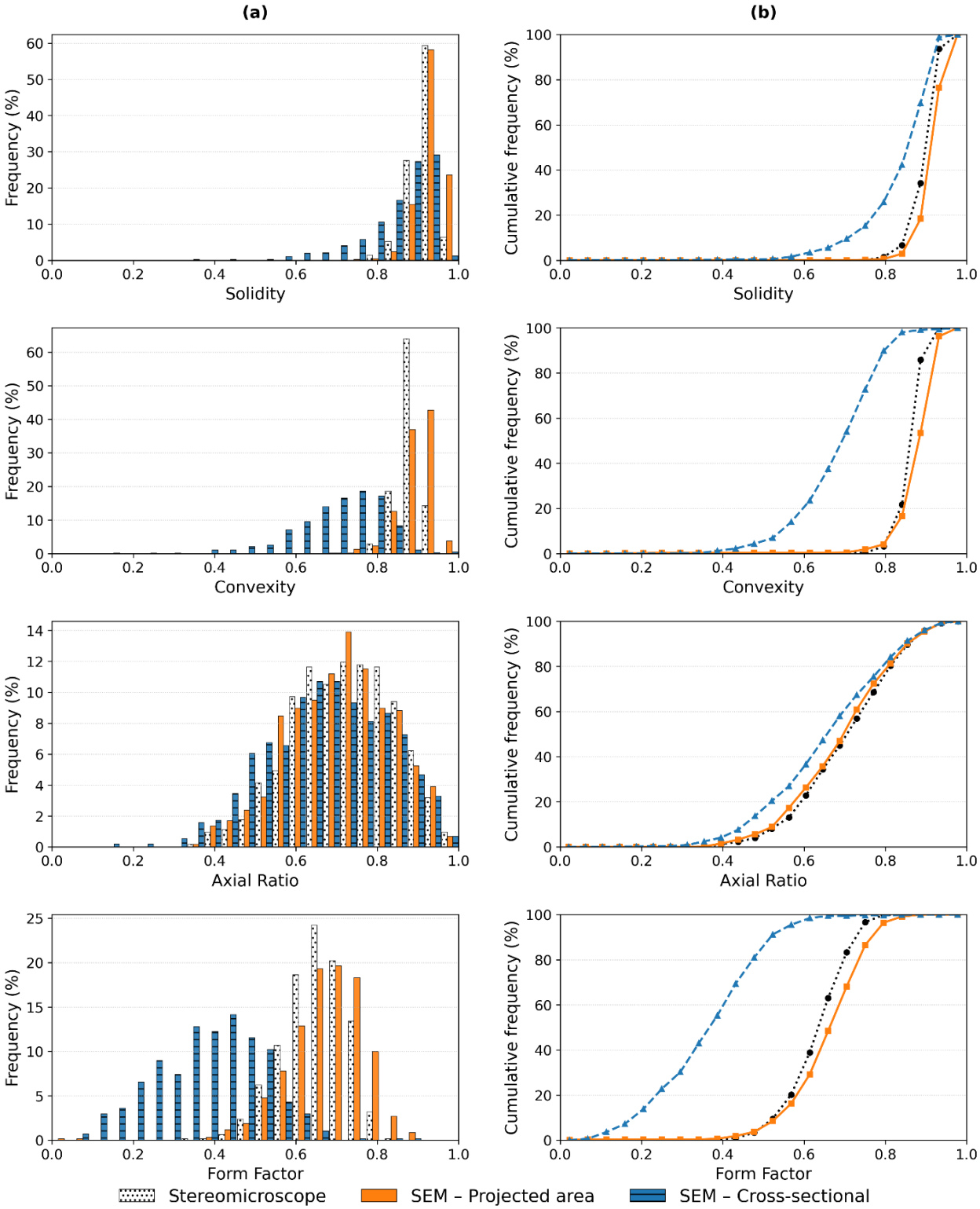

Figure 24. Frequency distribution in our samples of the four shape parameters (solidity, convexity, axial ratio, and form factor) that effectively account for the morphological variance within most ash samples according to Liu et al. (2015a), for the three imaging techniques used in our study.

All distributions across shape parameters and imaging techniques are unimodal. In general, distributions made using SEM-CS images exhibit a broader range and lower modes than those made using projected area (stereomicroscope and SEM-PA). The mode of the distributions of all the three imaging techniques is roughly the same for solidity (0.93) but significantly lower for the SEM-CS for convexity (0.75 compared to 0.89–0.93 for the other two techniques), axial ratio (0.65 compared to 0.73) and form factor (0.43 to 0.66–0.70). SEM-PA consistently yields slightly higher values than stereomicroscope, except for axial ratio, where the two methods overlap (Figure 24). We note that these results are consistent with those presented by Liu et al. (2015a) for different clasts, thus confirming this general trend across eruption type, magma composition, fragmentation processes, etc.

Following Liu et al. (2015a) and Nurfiani and Bouvet de Maisonneuve (2018), we then use plots of convexity as a function of solidity (Figure 25a) and axial ratio as a function of form factor (Figure 25b) to characterize shape variation between components. These and other shape parameters derived from the three imaging techniques overlap significantly (Supplementary Figure 7).

Despite large overlaps between shape parameters of particles in each component there are variations between average shapes. On average, juvenile particles have lower solidity, convexity, form factor and axial ratio, as already suggested by the semi-quantitative estimation of the roughness of the edges realized on the SEM-PA images (Figure 23). However, juvenile particles do not form a distinct cloud of data in Figure 25a-b nor Supplementary Figure 7 that would allow us to individually distinguish them from the other components based on shape alone, and all components values largely overlap.

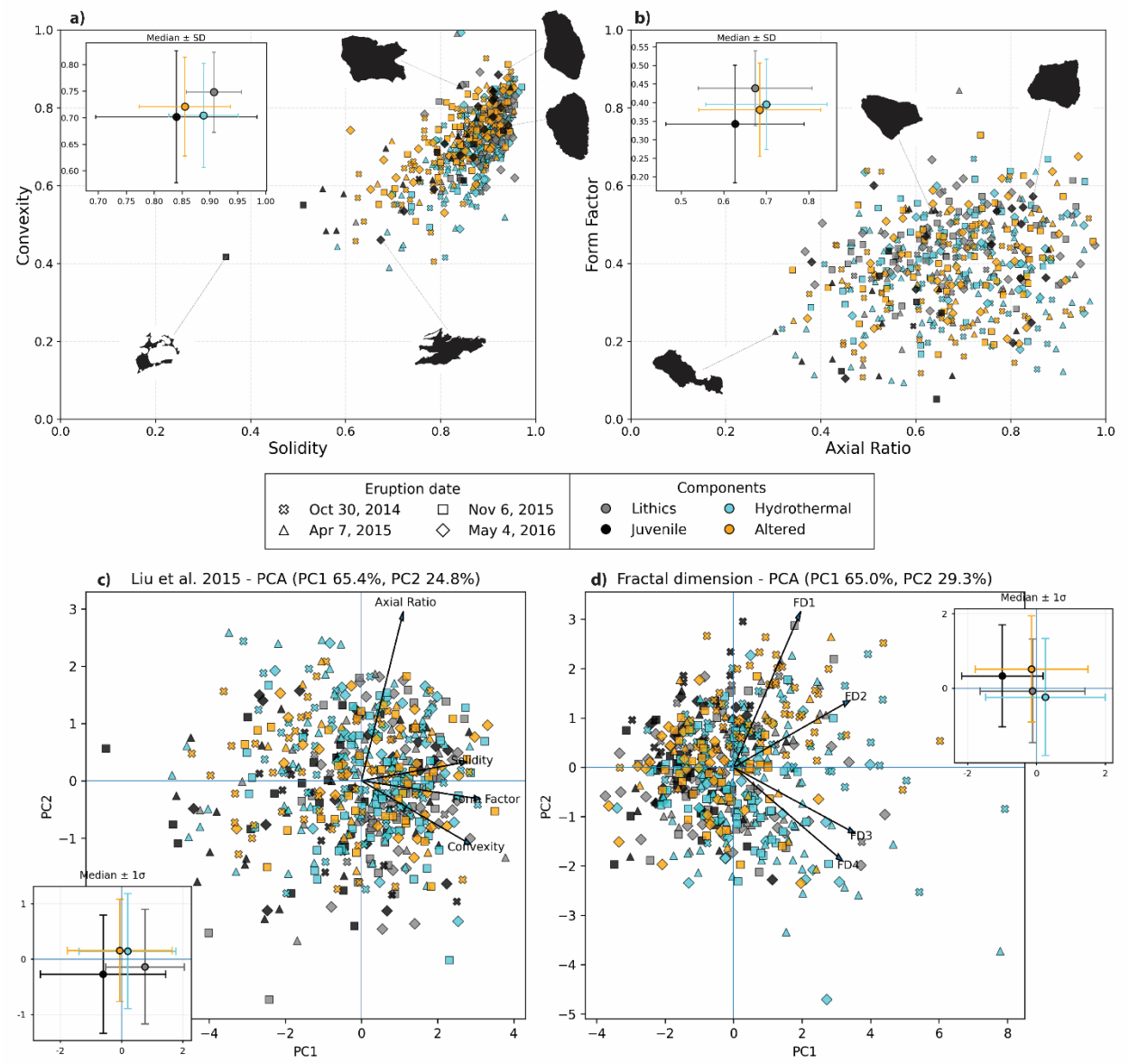

Figure 25. Shape parameters. a) Convexity vs Solidity plot for all the particles and eruptions of our study with examples of different shapes, inset with the median and one standard deviation for our four main components. b) Axial Ratio vs Form Factor parameters with examples of different particles shapes and inset with the median and one standard deviation as b). c) Principal component for the fractal dimension based on Nurfiani and Bouvet de Maisonneuve (2018). d) Principal component analysis based on the four main parameters from Liu et al. (2015a).

We performed principal component analysis (PCA) using these four shape descriptors to reduce the dimensionality and tentatively visualize the complex patterns formed by the data. Figure 25c shows that the first three principal components explain 95% of the variance (and PC1 = 65.4%, PC2 = 24.8%), with PC1 being primarily influenced by the axial ratio, separating elongated from

equant particles, and PC2 being dominated by convexity, solidity, and form factor, reflecting compactness and boundary smoothness. However, there remains no clear distinction between components using this PCA, with all four clouds of component data overlapping (Figure 25c).

The principal component analysis of the four fractal dimensions calculated following Nurfiani and Bouvet de Maisonneuve (2018) explains 94.3% of the total variance (PC1 = 65%, PC2 = 29.3%). PC1 is controlled by the first and second fractal dimensions, while PC2 is influenced by the 3rd and 4th fractal dimensions. Although juvenile particles tend to have negative or low PC1 values, using the fractal method does not allow to distinguish between the different components, like for the other shape parameters.

4. Discussion

4.1 Componentry

Our results demonstrate that componentry is highly vulnerable to misinterpretation for these relatively small ash eruptions The confusion matrices created in Figure 21 help calculate correction-factors to be applied to the component proportions in the stereomicroscope componentry and thus retrieve the 'true' proportions of a given eruption. However, if some tendencies apply across all eruptions (e.g., a hydrothermal particle is never misinterpreted for a juvenile, and vice versa), the correction factors vary from one eruption to the another and thus cannot be used across these four eruptions and beyond.

Our findings show, however, that stereomicroscope-based classifications systematically overestimate the proportions of juvenile as many clasts that appear juvenile under the stereomicroscope reveal different degrees of internal alteration of their glass and/or crystals once observed on cross-section under the SEM. This is the case for 67% of our 'juvenile' particles, on average, but this number varies between 50–96% depending on the eruption, a number particularly

important for eruptions dominated by hydrothermal or altered fragments (2014 eruption, Figure 22). Misclassification can thus lead up to an overestimation of the juvenile fraction by up to a factor of 26 in the case of the 2014 eruption, and robust evaluation of fresh magma involvement unfortunately requires the imaging of the internal texture of the particles (Figure 21). The proportion of juvenile material, as determined based using a stereomicroscope, should thus always be considered a maximum. This is consistent with previous observations at Turrialba and other volcanoes where external appearance alone is inconclusive of juvenile fresh magmatic input (e.g., Alvarado et al., 2016b; Pardo et al., 2014).

So far, we have considered that juvenile particles should exhibit no alteration of their glass nor their crystals. Using this condition, juvenile particles are always a minor component of the 250–500-µm particles in the eruptions in 2015 and 2016 (1–2%) and are almost absent of the 2014 eruption (one particle only). Because we have gone through the exercise of classifying the degree of alteration of both the glass and the crystals in all particles, we can evaluate whether the proportion of juvenile would change if we are slightly more flexible in the definition of 'juvenile', allowing for the degree of alteration of 'juvenile' particle to arbitrarily be up to 1 for both the glass and the crystals. Using this new definition of 'juvenile' more than double the overall proportion of juvenile across eruptions (from 41 to 84 particles), multiplying the proportion by a factor of 8 for the 2014 eruption (from 1 to 8 particles) and leading to an increase of 59–188% for the 2015–2016 eruptions, always to the expense of the proportion of altered material. . However, given the low amount of 'juvenile' in the componentry of all four eruptions overall, this leads to only a small increase in the proportion of juvenile in the material from eruptions in 2015–2016 (from 1–2% to 3–4%, Figure 22 right bar on each plot). We note that the proportion of juvenile (strictly-speaking) should be investigated for different size fractions and depending on the overall grain size

distribution of a sample, relaxing the definition of juvenile regarding their degree of alteration can increase the proportion of juvenile material altogether.

Furthermore, experiments show that in contact with hyper acidic volcanic lake water, plagioclase and pyroxene are altered to opaline silica, but the matrix glass remains largely unaffected (Lowenstern et al., 2018; van Hinsberg et al., 2020). Across the four eruptions studied, we identified 71 particles that do not show any sign of alteration of their matrix-glass. If 76% of them do not show alteration of their crystals either (considered juvenile), 24% of these glass-fresh particles exhibit different degrees of alteration of their crystals. This type of reaction thus affects the products of Turrialba volcano where the hydrothermal system is active and strong, especially during the 2010–2016 eruptions (Alvarado et al., 2016b; de Moor et al., 2016a; Lücke and Calderón, 2016; Mick et al., 2021).

4.2 Morphology

Nurfiani and Bouvet de Maisonneuve (2018) showed that combining classic descriptors (solidity, convexity, axial ratio, form factor) with fractal metrics effectively discriminates eruption styles and highlights blocky/vesicular contrasts. In the case of Turrialba volcano, however, shape descriptors only provide complementary but limited insights (Figure 25). The large overlap amongst components across all metrics analyzed indicates that morphology alone is not diagnostic in these small eruptions. The SEM-CS dataset shows a broader distribution than the other two techniques, but this variability does not resolve distinct component groups (Supplementary Figure 7). Hydrothermal particles, for example, show the widest range of values, in most shape metrics, and their distributions still overlap with altered and lithics clasts (Figure 25). This highlights the complexity of relying on shape as a diagnostic tool in hydrothermally influenced eruptions.

Principal component analyses further illustrate this limitation. Both the shape descriptor

PCA and the fractal dimension PCA capture the majority of morphological variance, yet neither yield clustering related to the componentry (Figure 25 c, d). We note here that we have calculated several other shape parameters (e.g., circularity, elongation, rectangularity, compactness, following e.g., Büttner et al. (2002); Liu et al. (2015a); Nurfiani and Bouvet de Maisonneuve (2018)), plotted them using many combinations (e.g., compactness × elongation vs. circularity × rectangularity; see Murtagh and White (2013) and Supplementary Figure 7), trying PCA on all these shape parameters combined or using subsets of these shape parameters, with or without including the fractal dimension analysis, and never found any relationship between combination(s) of shape parameters and the nature of a particle in these samples. The absence of componentry-based groupings in these shape parameters plots thus suggests that shape metrics are not reliable indicators to identify juvenile material during the 2014–2016 eruptions at Turrialba volcano. Instead, they reflect the broad spectrum of particle irregularity and texture generated by phreatic to phreatomagmatic fragmentation. For operational monitoring, this implies that ash shape data alone cannot resolve eruptive transitions at Turrialba.

4.3 Combining techniques

Taken together, the combined approach of imaging the surface and investigating the internal textures of ash particles using semi-quantitative alteration scales provides a robust basis for componentry classification. Our results demonstrate that early eruptions in 2014, 2015 and 2016 were all dominated by altered and hydrothermal particles, with only a minor contribution of juvenile material, which increases between 2014 (anecdotal) and later eruptions (1–3%). This agrees with the interpretations based on gas monitoring, which identified the onset of magmatic influence in 2015 (de Moor et al., 2016a) and slightly contrasts with studies suggesting juvenile involvement of juvenile magma since 2010 (Alvarado et al., 2016b). By May 2016, our

componentry shows the unambiguous presence of juvenile particles, supporting the conclusion that fresh magma input reached the surface (albeit in small amount in the 250–500-µm size fraction, 3%).

Further, machine learning studies show promise in classifying ash particles rapidly with feature-based models achieving strong performance (Benet et al., 2024). However, these approaches rely on training datasets dominated by eruptions with clear juvenile-non juvenile contrasts. In small phreatic and phreatomagmatic eruptions, where altered and recycled particles dominate and often look alike under the stereomicroscope, machine learning risks overfitting to surface features (color, roughness, shape) and misclassifying fresh-looking clasts as juvenile. Thus, machine learning should be used cautiously in hydrothermal-rich systems, trained on volcano-specific datasets, and paired with personnel oversight, unless the automated classification is done using cross-sectional images of the grains acquired using an SEM, in which case the recognition of internal texture should lead to much better and more reliable results.

Finally, reliability for probabilistic event trees depends on the accurate identification of fresh juvenile magma. Inconclusive or ambiguous classification of juvenile particles can prematurely bias the event tree toward magmatic escalation. Wright et al. (2019) emphasized how, for the eruption of Sinabung volcano since 2013, Indonesia, event trees were revised iteratively as new results of the componentry happened. In the case of Turrialba volcano, and probably for most open-system volcanoes producing small scale explosions like these studied here, our results show that the most reliable and fastest way to identify juvenile magma is to embed in resin and polish at least several tens of juvenile-looking particles that were rapidly collected after the eruption for further observations under the SEM, focusing on the degree of alteration of the crystals and the matrix glass to identify.

5. Conclusions

Our study demonstrates the importance of integrating multiple imaging techniques and quantitative morphology descriptors to improve ash componentry analysis during volcanic crises. At Turrialba volcano, for eruptions in 2014–2016, stereomicroscope-based classifications systematically overestimated the abundance of juvenile material. SEM cross-sections revealed that many particles initially classified as juvenile were in fact altered or lithic, underscoring the risk of misinterpretation when relying solely on external appearance. Such errors are particularly problematic in low-energy or hydrothermal-dominated systems, where the first signals of magmatic involvement can be subtle but critical for hazard assessment.

We show that semi-quantitative measures of surface and edge roughness, combined with particle shape descriptors such as convexity, solidity, and fractal dimensions, provide valuable constraints on particle classification. Although none of these metrics alone can unambiguously distinguish components, together they allow trends to be identified that improve the reliability of rapid analyses. In particular, the progressive transition from sharp-edged, smooth-surfaced juvenile clasts to increasingly rough, smoothed altered and then hydrothermal particles highlights how shape data can help track alteration processes and eruptive evolution.

Our findings suggest that operational ash monitoring can benefit from the use of streamlined shape analysis and targeted SEM observations, enabling faster and more accurate detection of juvenile magma in eruptive products. By establishing correction factors for stereomicroscope classifications and by evaluating the reproducibility of shape parameters across imaging techniques, this study provides a framework to refine componentry protocols. Applied in real time, such approaches can strengthen the early recognition of eruptive transitions, improve event tree parameterization, and thus enhance volcanic hazard forecasting during unrest.

Future work should further evaluate the utility of automated image analysis and machine learning approaches to reduce subjectivity and accelerate component classification. Broader application across volcanoes of different compositions and eruptive styles will be necessary to confirm the generality of these results and to optimize their integration into operational monitoring strategies. Concerning Turrialba volcano and the series of eruptions studied here, performing componentry on both finer and coarser scales while coupling it with grains size distributions will allow a real quantification of the proportion of juvenile material ejected during this transitional phase of Turrialba eruptive activity. This work, together with similar analysis of other eruptive products ejected before and after 2014–2016, is in progress.

6. Bridge

Chapter 3 established a framework for ash componentry analysis by validating stereomicroscope classifications with multiple imaging techniques and incorporating morphological measurements. This approach revealed that componentry in small eruptions is more nuanced and requires integrating additional methods to confidently categorize juvenile particles. These methodological advances provide a more robust foundation for interpreting ash records and linking them to eruptive processes.

In Chapter 4, I apply the methods from previous chapters to study a decade of eruptions at Turrialba (2010–2019) volcano. Here, I examine how ash physical properties (grain size, componentry, and density) relate to eruptive and monitoring signals across multiple eruptive phases. This chapter shows how ash analysis can explain temporal changes in eruption dynamics and support operational forecasting for small, hydrothermally influenced eruptions.

CHAPTER IV

4. ASH COMPONENTRY, DENSITY, GRAIN-SIZE AND FRACTAL DIMENSION TRACK ERUPTIVE TRANSITIONS AT TURRIALBA VOLCANO (2010–2019), COSTA RICA

1. Introduction

Volcanic ash produced by explosive eruptions is one of the most widespread and persistent volcanic hazards. Even low-intensity explosive activity can disrupt transportation, contaminate water and air supplies, damage infrastructure, and impact communities (Cioni et al., 2014; de Moor et al., 2016a). From a volcanological perspective, fine-grained tephra deposits preserve time-sensitive records of subsurface dynamics, offering unique insights into the evolution of magma–hydrothermal systems and fragmentation mechanisms (Matsumoto and Geshi, 2021; Miwa et al., 2013).

The physical and compositional properties of ash particles are direct manifestations of the conditions within the volcanic conduit and shallow hydrothermal system (Cascante et al., 2025). Ash properties can reflect not only the style and efficiency of magma fragmentation, but also changes in magma ascent, interaction with external water, and hydrothermal sealing and pressurization. Consequently, detailed characterization of ash is increasingly being integrated into petrological monitoring frameworks at volcano observatories worldwide (Alvarado et al., 2016b; Cashman and Hoblitt, 2004; Dellino et al., 2012; Hamzah et al., 2025; Iguchi et al., 2019).

Many volcanoes with active hydrothermal systems experience sequences that begin with phreatic eruptions, often triggered by the pressurization of shallow sealed systems (Stix and de Moor, 2018). These eruptions may transition to phreatomagmatic or magmatic activity as they evolve, and magma potentially rises toward the surface. Such transitions are recorded in the physical characteristics of volcanic products, making them a valuable monitoring tool. Previous work has shown that changes in grain-size distributions, componentry, and particle density can

reflect shifts in eruption style (Alvarado et al., 2016b; Cascante et al., 2025; Hamzah et al., 2025; Maeno et al., 2023).

Despite this potential, interpreting ash records in small, hydrothermally influenced eruptions remains challenging (Alvarado et al., 2016b; Pardo et al., 2014). Deposits are often dominated by hydrothermal and altered material with only minor fresh-looking juvenile content, making it difficult to detect magma involvement. Furthermore, time-consuming analytical workflows can delay critical hazard assessments. There remains a pressing need to refine rapid, reproducible, and operationally relevant ash characterization approaches that can reliably detect subtle magmatic signals during unrest (Benet et al., 2024; Iguchi et al., 2019; Shoji et al., 2018).

Turrialba volcano, Costa Rica, offers an exceptional opportunity to address these questions. Between 2010 and 2020, Turrialba experienced a decade-long phase of unrest characterized by frequent, small ash-producing explosions, punctuated by transitions from phreatic to phreatomagmatic activity and culminating in persistent open-vent degassing (van der Laat et al., 2022). This sequence is one of the most thoroughly documented episodes of unrest in Central America, supported by a dense multidisciplinary monitoring network that includes seismic, gas, and geochemical measurements (Alvarado et al., 2016b; Avard et al., 2021; de Moor et al., 2016a; DeVitre et al., 2019; van der Laat et al., 2022).

Similarly, recent work at Poás volcano, another hydrothermally influenced system in Costa Rica, has shown that systematic variations in ash properties can trace transitions from phreatic to phreatomagmatic and recycled-ash phases across eruptive cycles (Cascante et al., 2025). Together, Poás and Turrialba exemplify long-lived, open-vent volcanoes with hydrothermal systems where small-scale explosive activity can provide early warnings of magmatic involvement if interpreted correctly.

In this study, we focus on the physical characteristics of ash produced during the 2010–2019 eruptive sequence at Turrialba volcano. Our objectives were to characterize how ash properties evolve through phases of unrest at Turrialba volcano and to link these changes to subsurface processes. Additionally, we aimed to assess the diagnostic value of ash characteristics for monitoring and forecasting eruptive transitions by combining ash data with monitoring observations.

1.1 Turrialba volcano

Turrialba is a stratovolcano located at the southern end of the Central America Volcanic Front, approximately 35 km east of the San José International Airport in Costa Rica (Figure 26). The summit of Turrialba consists of three craters (West, Central and East), and a graben structure (Alvarado et al., 2016b; van der Laat et al., 2022). Prior to the 2010–2019 activity, the last eruption occurred in 1864–1866 (Di Piazza et al., 2015; Reagan et al., 2006). Signs of volcanic reawakening started in 1996 with increased seismicity (Martini et al., 2010), particularly shallow volcano-tectonic (VT) earthquakes, which indicated brittle fracturing of the edifice. The gas flux before 2001 was low and occurred mainly in the Central and West crater (Tassi et al., 2004). From 2005 to 2008 a progressive increase in both fumarolic gas flux and seismic activity resulted in new fumarolic vents in distal areas (Vaselli et al., 2010).

Gas measurements of SO_2 showed an increase in emission rate from ~350 tons/day to ~3,500 tons/day within a year, leading up to an eruptive period in 2010 (Conde et al., 2014; de Moor et al., 2016a). During 2010, seismic records revealed the onset of long-period (LP) events and early tremor episodes, both typically interpreted as the response of a sealed hydrothermal system to fluid pressurization and movement at shallow levels (Table 3, Stix and de Moor 2018; van der Laat et al. 2022).

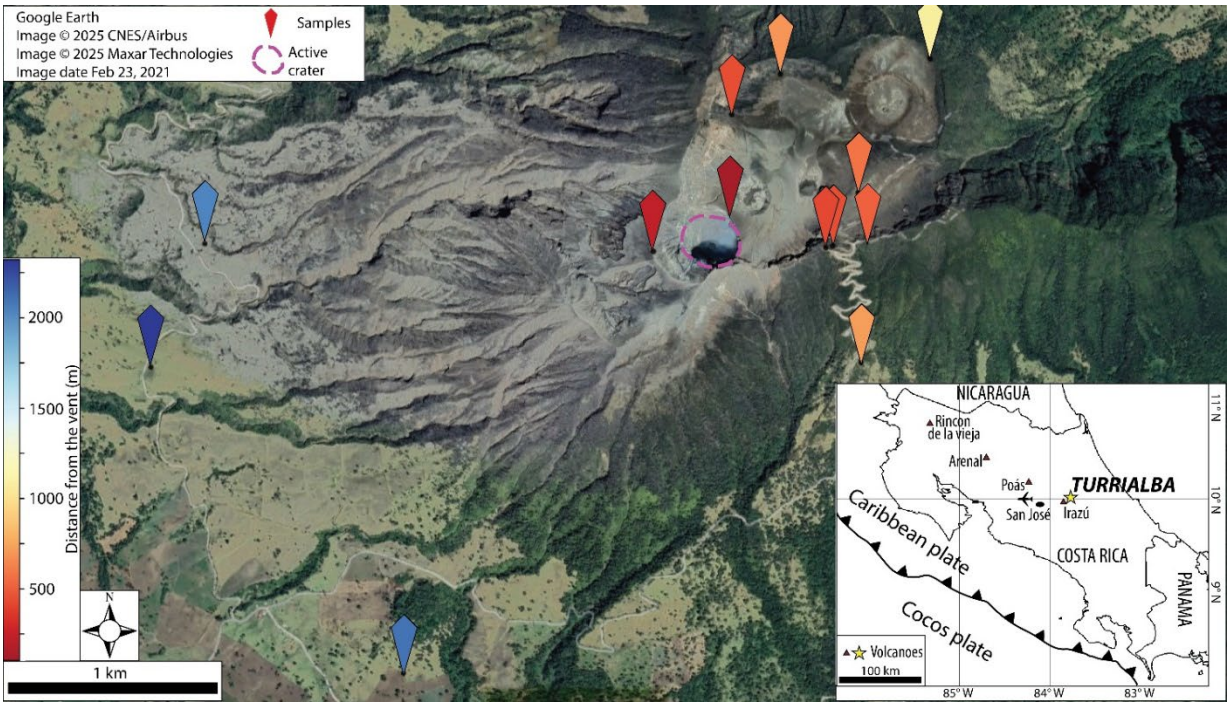

Figure 26. Turrialba volcano aerial view and insert map of location in Costa Rica. Sample location by color indicating distance from the vent in meters. Color coding of the symbols is consistent throughout the figures in this chapter. Google Earth© imagery date Feb 23, 2021.

Furthermore, de Moor et al. (2016a) observed variations in CO_2/SO_2 and H_2S/SO_2 gas ratios and proposed that variations in these gas ratios were due to the relative contributions of distinct gas sources, where CO_2 exsolved from deep magma, SO_2 from shallow magma, and H_2S was a hydrothermal gas. Of particular interest, H_2S/SO_2 variations were attributed to differing contributions of either the hydrothermal or magmatic gas sources, respectively (Stix and de Moor 2018). Increased unrest culminated in sporadic phreatic and phreatomagmatic eruptions occurring between 2010–2014 (Alvarado et al., 2016b, 2016a; Lücke and Calderón, 2016). Eruptive style then shifted from phreatomagmatic to magmatic mid-2015 to 2016 and generated basaltic-andesite to andesitic products (Alvarado et al., 2016b; DeVitre et al., 2019; Rizzo et al., 2016; Stix and de Moor, 2018). Discontinuous eruption episodes persisted until 2020 and caused the closure of 12 schools, the evacuation of farms within 4 km of the crater, and ~110 flight cancellations at San José International Airport, affecting ~7000 passengers (de Moor et al., 2016a).

Table 3. Summary of monitoring data and interpretation from 2010-2019.

Period	Eruption Type	Plume Height (km)	Seismicity (van der Laat et al., 2022)	Gas flux and ratios (de Moor et al., 2016)	Interpretation	References
Early 2010	Phreatic	≤1	First signs of increased seismic activity	SO_2 ~350→1000 t/d. CO_2/SO_2 high. H_2S/SO_2 high. Hydrothermal dominant	Hydrothermal pressurization and vent opening	Martini et al., 2010 Vaselli et al., 2010 de Moor et al., 2016 van der Laat et al., 2022
2011–2013	Phreatic	≤1	Persistent background seismic tremor begins. Early tornillo-type signals appear but not always followed by eruptions	Moderate SO_2 (~800–1500 t/d). High H_2S/SO_2. Increasing CO_2/SO_2	Hydrothermal sealing cycles with incipient magmatic? input	Vaselli et al., 2010 de Moor et al., 2016 van der Laat et al., 2022
Late 2014	Phreatic–phreatomagmatic?	1–2	Tremor energy increases. Tornillo signals reach their highest frequencies.	SO_2 >3000 t/d. Sharp rise CO_2/SO_2. Fluctuating H_2S/SO_2	Magma degassing through sealed hydrothermal zone. Increased overpressure	Lücke & Calderón, 2016 Alvarado et al., 2016a de Moor et al., 2016 van der Laat et al., 2022
Early 2015	Phreatic–phreatomagmatic?	1–3	Swarms VT and LP. Increased tremor	SO_2 sustained >3000 t/d. Rising CO_2/SO_2. H_2S/SO_2 dropping	Progressive hydrothermal seal failure, magma rising	Alvarado et al., 2016a de Moor et al., 2016 van der Laat et al., 2022

Mid 2015	Phreatomagmatic-Magmatic?	≤4	Tremor, LP and VT seismicity high. Tornillo drops	SO_2 ~3500 t/d. Max CO_2/SO_2. Low H_2S/SO_2	Conduit fully opened. Major magmatic input	Alvarado et al., 2016b Rizzo et al., 2016 Stix & de Moor, 2018 de Moor et al., 2016 van der Laat et al., 2022
2016	Magmatic	0.5–2	LP and Tornillo swarms. VT migration (Tectonic earthquake Mw 5.5)	Sustained high SO_2. Stable CO_2/SO_2. Low H_2S/SO_2	Magma input and open conduit establishment	de Moor et al., 2016 van der Laat et al., 2022
2017	Open-vent magmatic	0.5–2	Harmonic tremor and drumbeats.		Stable open-vent degassing with periodic explosions	van der Laat et al., 2022
2018–2020	Open-vent magmatic	≤2	Low tremor energy. Fewer VT swarms		Low-level degassing, no major magmatic input	van der Laat et al., 2022

2. Methodology

Our physical characterization of ash samples involved three main analytical techniques: grain-size analysis by laser diffraction, componentry analysis by stereomicroscope classification, and density measurements by helium pycnometry. Not all methods were systematically applied to every collected sample (Table 4 summarizes which analyses were performed on each sample). Analytical procedures closely followed those applied for Poás volcano by Cascante et al. (2025) but were modified to reflect differences in sample condition, preparation, and availability of material.

2.1 Sample collection

The pyroclastic products of individual explosive events at Turrialba volcano were collected during the 2010–2019 eruptive activity. While most samples weighed between 0.1 and 0.8 kg, five were smaller, ranging from 0.025 to 0.085 kg. Sampling was carried out within a maximum of four days after deposition, but most samples were collected the same day as the eruption. A total of 13 sites were sampled at distances ranging from 100 m to 2300 m from the vent, distributed both upwind and downwind of the volcano to capture spatial variability in ash dispersal. All samples were unconsolidated at the time of collection and consisted of mostly ash deposits. Site selection prioritized accessibility, safety, monitoring station sites, and coverage of different dispersal sectors. Table 4 provides sample collection details, including collection date, eruption date, location, distance from the vent, plume height, and information on which technique was applied for each sample.

For samples used in componentry and density analyses, wet sieving was done prior to further processing. Samples were gently sonicated to help with disaggregation, with ultrasonic applied in 30-second intervals to minimize breakage. The samples were then wet sieved in whole φ intervals, where $\varphi = -\log_2(d)$ and d is the particle diameter in millimeters, creating eight size

fractions ranging from >2000 μm to <32 μm. Each fraction was later dried at approximately 60°C for 24 hours and then weighed.

Table 4. Sample date of collection, eruption date, coordinates, distance from the vent, plume height, and the technique that was performed. Plume height was estimated by visual and seismic data from the Costa Rican Volcano Observatory. No plume height means no observation.

Sample collection date	Eruption date	Easting Zone 17	Northing Zone 17	Distance from vent (m)	Plume height (m)	Laser diffraction	Compo-nentry	Density
Jan 5, 2010	**Jan 5, 2010**	195743	1106995	2103	1000	X		
Jan 8, 2010	**Jan 5, 2010**	196749	1108686	220	1000	X	X	X
Jan 19, 2012	**Jan 18, 2012**	196749	1108686	220	1000	X		X
May 21, 2013	**May 21, 2013**	196749	1108686	220	1000	X		X
May 21, 2013	**May 21, 2013**	196749	1108686	220	1000			X
Oct 30, 2014	**Oct 30, 2014**	197122	1108620	175	4000	X		
Oct 30, 2014	**Oct 30, 2014**	197538	1108274	714	4000	X		
Oct 30, 2014	**Oct 30, 2014**	196749	1108686	220	4000	X	X	X
Apr 7, 2015	**Apr 7, 2015**	196749	1108686	220	2000		X	
May 6, 2015	**May 6, 2015**	197037	1109186	487	500	X		
Nov 6, 2015	**Nov 6, 2015**	194933	1108727	2035		X	X	X
Feb 11, 2016	**Feb 11, 2016**	196749	1108686	220	1000		X	X
May 2, 2016	**May 2, 2016**	197538	1108274	714	1000		X	X
May 4, 2016	**May 4, 2016**	197407	1108707	439	500	X	X	X
May 4, 2016	**May 4, 2016**	197219	1109341	685	500	X		
Oct 3, 2016	**Oct 3, 2016**	197407	1108713	439	1000		X	X
Oct 24, 2016	**Oct 24, 2016**	197037	1109186	487	100		X	X
Oct 24, 2016	**Oct 24, 2016**	197219	1109341	685	100	X		
Nov 1, 2016	**Nov 1, 2016**	194697	1108224	2321	500			X
Nov 1, 2016	**Nov 1, 2016**	197037	1109186	487	500	X		
Nov 7, 2016	**Nov 7, 2016**	194697	1108224	2321	500			X
Nov 7, 2016	**Nov 7, 2016**	194933	1108727	2035	500			X
Nov 9, 2016	**Nov 9, 2016**	197509	1108727	541	1000			X
Nov 10, 2016	**Nov 10, 2016**	197383	1108701	415	200			X
Nov 16, 2016	**Nov 16, 2016**	197507	1108903	575	200			X
Nov 22, 2016	**Nov 16, 2016**	194697	1108224	2321	300			X
Feb 22, 2017	**Feb 18, 2017**	197037	1109186	487		X		
Mar 9, 2017	**Mar 9, 2017**	196898	1108628	103	100		X	X
May 15, 2017	**May 15, 2017**	197037	1109186	487		X		X
Sep 21, 2017	**Sep 21, 2017**	197037	1109186	487		X		
Mar 2, 2018	**Mar 2, 2018**	194697	1108224	2321	100	X		
Oct 9, 2018	**Oct 5, 2018**	197780	1109402	1071		X	X	X
Feb 12, 2019	**Feb 12, 2019**	197037	1109186	487				X
Mar 26, 2019	**Mar 26, 2019**	197383	1108701	415				X
Apr 11, 2019	**Apr 11, 2019**	197022	1108795	106			X	X

2.2 Grain Size Distribution

Grain-size distributions were obtained using laser diffraction following dry-sieving

preparation. After drying overnight in the oven at 35°C to remove moisture, each sample was first passed through a 1 mm sieve to remove larger clasts and prevent clogging in the laser diffractometer. The instrument we used was a Beckman Coulter LS 13320 at the U.S. Geological Survey Cascades Volcano Observatory in Vancouver, Washington, USA. Measurements were made using a refractive index of 1.58 and an absorption coefficient of 0.01 (Romero et al., 2020). Refractive index and absorption coefficient are important because laser diffraction measures the pattern of scattered light and then uses a physical model to infer particle-size distribution. The model uses optical constants (refractive index and absorption coefficient) to determine how particles interact with the laser. Laser diffraction cannot properly interpret scattering curves without knowing how strongly light bends (refractive index) and how much light is lost inside the particle (absorption coefficient). The instrument measured light scattering of particles circulating in water, providing the relative volume fraction of particles separated into 93 logarithmic size bins ranging from 0.3 μm to 2000 μm. Instrument calibration was performed with 500 μm glass bead manufacturer standards. Raw data were processed to obtain volume-based grain-size distributions and key metrics such as median diameter (D50) and distribution modality.

2.3 Componentry

Componentry analysis was conducted on all size fractions >125 μm of a selected subset of samples (Table 4). The number of grains analyzed per size fraction for each sample are listed in Table 5. Each sample was then subdivided into representative workable aliquots using a splitter. The aliquots were then wet sieved in whole φ intervals. High-resolution images of each aliquot were taken at a fixed magnification for each sieve size to maintain consistency across samples. All visible clasts within each image were analyzed using a binocular stereomicroscope, and the entire image area was used for classification to minimize bias. A minimum of 150 grains were classified

per size fraction whenever material availability allowed; when fewer than 150 grains were present, all available grains were counted. Clasts were classified into categories modified from Cascante et al. (2025, and from Chapter III Section 3.1): juvenile, lithic, hydrothermal, altered, aggregates, free crystals, and red/oxidized fragments. We use color, shape and luster to define the components then used in the analysis:

- Juvenile: Dark or transparent particles characterized by a glassy, vitreous luster and sharp, angular edges.
- Altered: Dark particles exhibiting a glittery surface sheen and subrounded edges, indicative of incipient alteration.
- Hydrothermal: White to yellow–orange, dull particles with rounded to subrounded edges, consistent with intense hydrothermal alteration.
- Lithic: Gray, dull particles with subrounded to angular edges, representing fragments of pre-existing country rock.
- Red: Distinctly red particles that cannot be readily assigned to the categories above based on macroscopic characteristics.

Table 5. Number of grains analyzed for componentry. Note that number of grains analyzed <150 means that all grains available were analyzed. No sample = no physical sample available

Sample collection date	Number of grains analyzed for componentry				
	>2000 µm	2000-1000 µm	1000-500 µm	500-250 µm	250-125 µm
Jan 8, 2010	51	348	176	286	341
Oct 30, 2014	122	368	292	276	329
Apr 7, 2015	73	353	267	375	431
Nov 6, 2015	36	190	373	417	332
Feb 11, 2016	no sample	38	429	466	518
May 2, 2016	no sample	no sample	174	469	412
May 4, 2016	no sample	no sample	96	370	449
Oct 3, 2016	no sample	5	422	341	289
Oct 24, 2016	no sample	41	427	372	297
Mar 9, 2017	59	357	322	425	236
Oct 9, 2018	no sample	no sample	85	643	345

Apr 11, 2019	no sample	8	424	631	329

2.4 Particle Density Measurements

Particle density was determined using a high-precision balance (±0.1 mg) in combination with a Micromeritics AccuPyc II 1340 helium pycnometer in selected samples (Table 4). High-purity helium was used as the working gas to measure the volume of the solid phase and closed porosity, as helium can fill between grains and into open pore spaces, but not into closed pores. For each sieve fraction, the dry mass was measured on the balance, and the corresponding volume was obtained using the pycnometer. Each volume measurement was repeated five times to ensure reproducibility, and the average value is reported. The uncertainty on the density combined the error associated with both mass and volume measurements and was less than 0.01 $g \cdot cm^{-3}$ for all reported values.

3. Results

3.1 Grain Size Distribution

Grain-size distributions for the <1 mm size fraction were obtained for 18 eruptions between 2010 and 2019 at Turrialba volcano (Table 4) and are shown in Figure 27a. For each sample, the distribution is normalized to the mass fraction of grains <1 mm, which varies between 61–100% for the 18 samples, with 10 samples having only particles <1 mm. The volume percentage distributions can be categorized into three types based on variations in distribution shapes and modes according to their equivalent diameter (*d*). The first type of distribution is unimodal with a well-defined peak between 205 μm and 430 μm equivalent diameter (Figure 27a, b). There are seven samples that show this trend; while all of them were collected less than 715 m from the vent, some of them were also upwind from the main wind dispersal axis. Most of these samples also have 10–30 wt. % of material >1 mm (see Figure 28). The second type of distribution displays broader features, with less distinct peaks between 170–390 μm. This distribution type includes six

samples and also exhibits a subtle shoulder or secondary mode in the finer fractions. The last set of distributions are wider with poorly defined peaks between 38–97 µm equivalent diameter (Figure 27b).

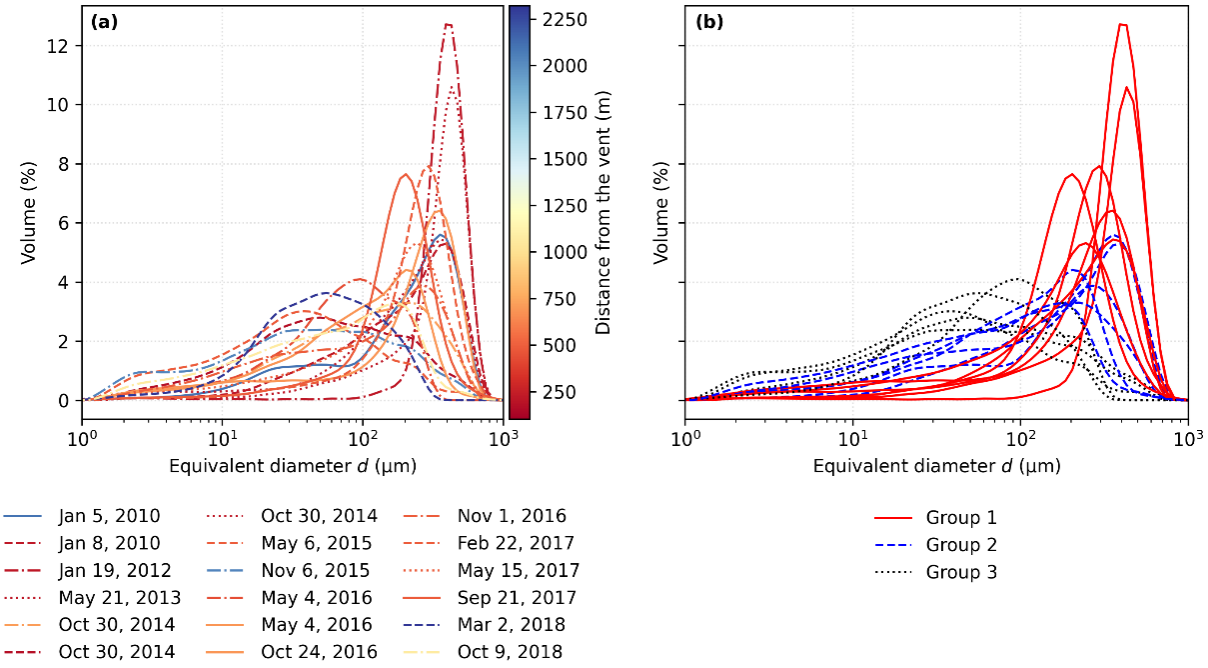

Figure 27. Grain size distribution of all the samples in volume percentage of the whole sample and equivalent diameter (d) in µm. (a) Colors represent the distance from the vent. (b) Colors represent separate groups.

Cumulative volume curves (Figure 28) show steep slopes for most proximal samples, with narrow distributions dominated by coarser sizes. The steepest slopes come from the Jan 19, 2012, and Sep 21, 2017 samples, and have a median diameter of 413 and 175 µm, respectively. The samples from Nov 6, 2015 and Oct 9, 2018 show the broader slopes, and a median diameter of 55 and 60 µm, respectively. The error bars in Figure 29 correspond to the 25th and 75th quartile (D25 and D75, respectively).

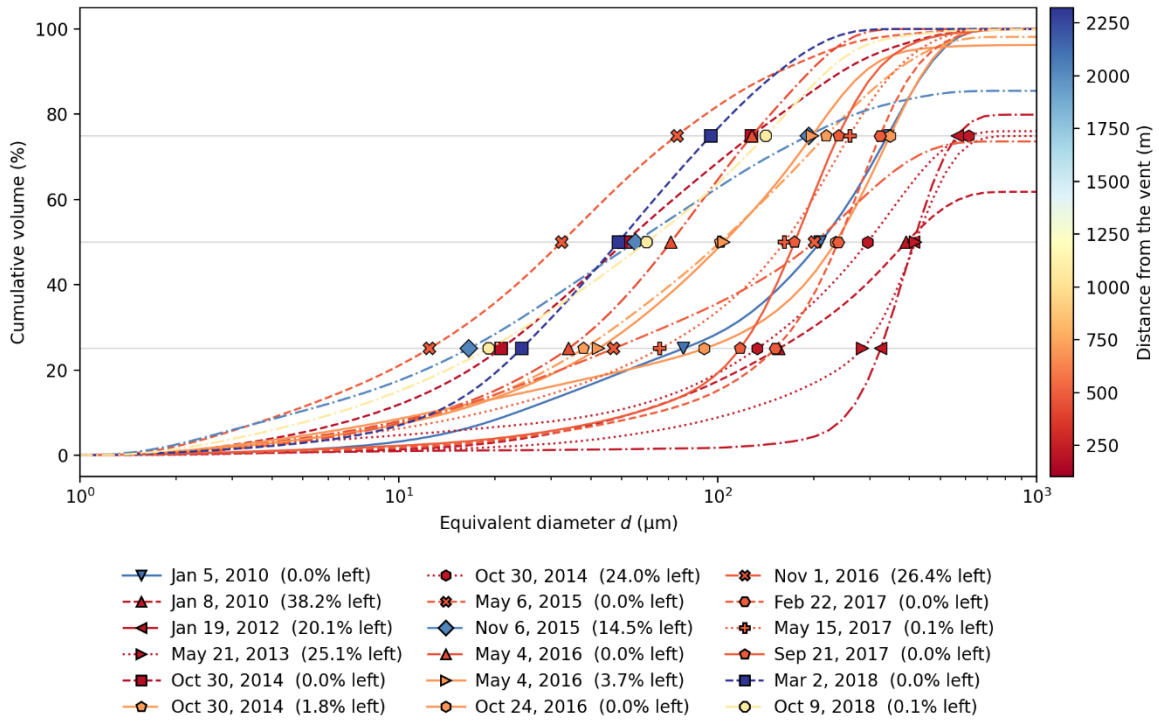

Figure 28. Cumulative volume fraction of all the samples as a function of equivalent diameter (d). The three horizontal lines are D25, D50 and D75. The symbols show the intercepts to the samples' curves. Because laser diffraction does not analyze >1000 µm sizes; we added the masses of the all the fraction <1000 µm and divide by the total mass. For this reason, some samples do not have D75. Legend shows the percentage left to reach the 100 % of the volume for every sample.

The median grain sizes (D50) for the samples span one order of magnitude, ranging from 32 µm to 418 µm (Figure 29). Early eruptions (2010–2013) display some of the coarser median sizes, with the coarsest being from May 21, 2013, collected 220 m downwind from the vent. Conversely, later events (2016–2019) generally exhibit intermediate to fine median grain size, although the finest sample (D50 = 32 µm) is from May 6, 2015, and was collected 487 m upwind from the vent (Figure 30).

Figure 29 illustrates the temporal evolution of D50 values over the eruptive sequence. The error bars correspond to D25 and D75. One of the finer samples from (May 15, 2017) was collected 500 meters from the vent (Figure 29); this particular sample is proximal however is was collected upwind from the main wind direction (Figure 30). In 2010, two samples were collected either immediately after (Jan 5; 2100 m downwind; D50= 21 µm) or three days after (Jan 8; 220 m

downwind; D50 = 391 µm) the same eruption. On Oct 30, 2014, three samples from the same eruption were collected in three different locations. The closest but upwind was 175 m from the vent and a D50= 51 µm, followed by another one at 220 m downwind from the vent with D50= 295 µm and, the furthest from the vent was at 714 m downwind with D50 = 102 µm.

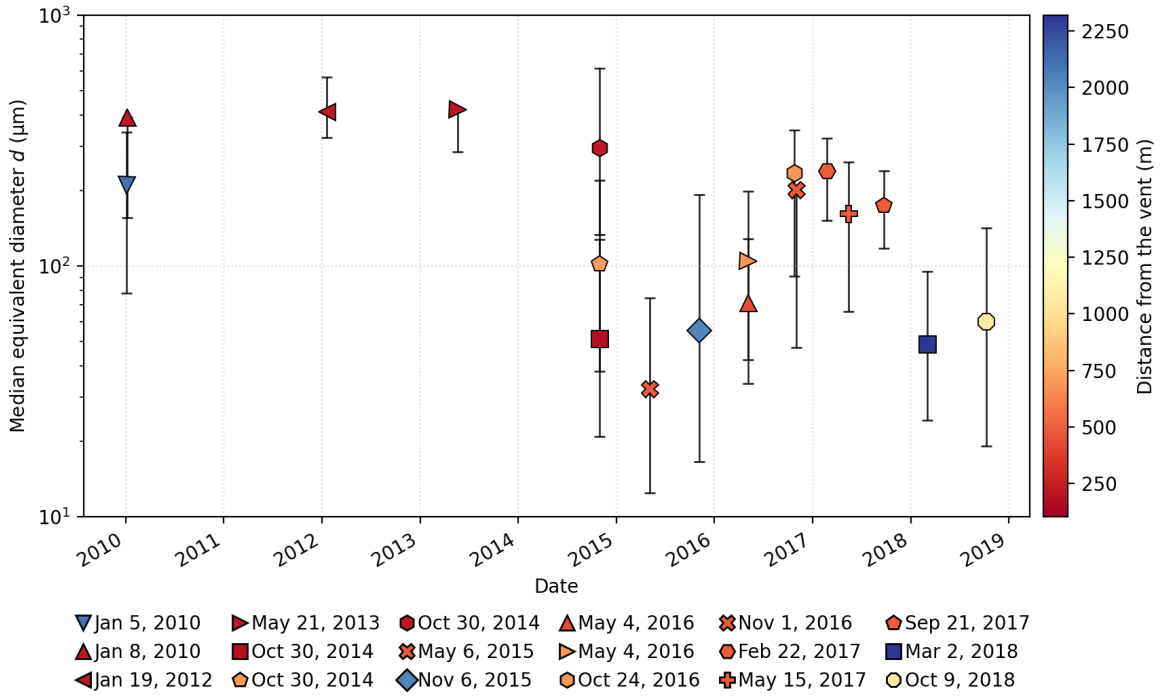

Figure 29. Median equivalent grain diameter (d) as a function of date and color of the symbols are distance from the vent in meters. The error bars correspond to D25 and D75.

Figure 30 shows the median grain size (D50) of each sample as a function of the distance from the vent, whether the sample was collected upwind or downwind, and the plume height. As expected, D50 roughly decreases with distance on either side of the vent. Proximal samples collected downwind from the vent indeed exhibit notably coarser D50 values, including the highest value (418 µm) from May 21, 2013 collected at 220 m downwind from the vent. However, the sample collected at more than 2 km downwind from the vent (second furthest) on Jan 5, 2010, and that was produced by an intermediate size plume (1 km), still exhibits one of the coarsest D50 (210 µm). Conversely, the sample collected the closest upwind from the vent on Oct 30, 2014, and

which was produced by the highest plume measured (4 km), is one of the finest, with a median diameter of 51 µm. Thus, there seems to be no strong correlation between plume height, distance from the vent and median diameter in our samples.

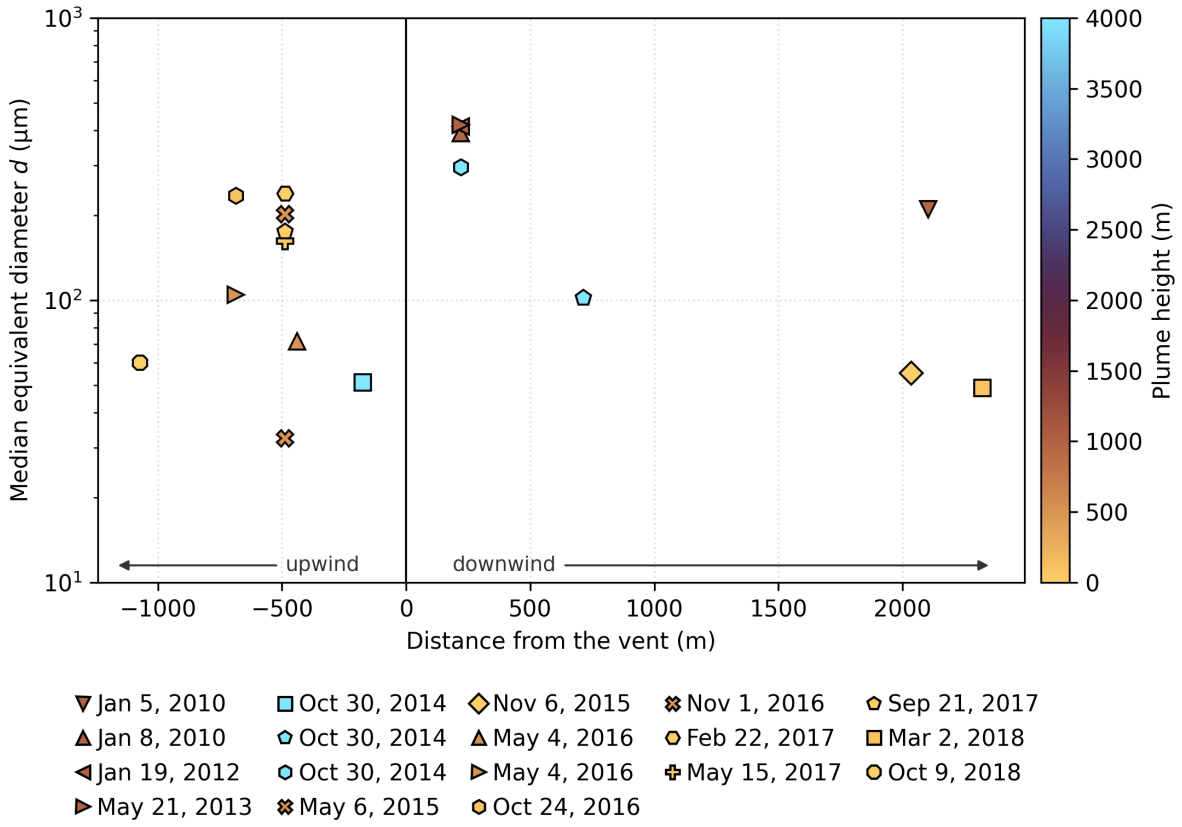

Figure 30. Median equivalent diameter (d) (µm) vs distance from the vent in meters, where negative numbers represent samples that were collected upwind and positive numbers are samples collected downwind from the vent. Symbol colors indicate plume height in meters; cyan colors denote 4000 meters above the crater floor and yellow colors represent the smallest plumes recorded.

3.2 Componentry

Componentry analysis was performed on five size fractions from 125–250 µm to >2000 µm for twelve samples collected between 2010 and 2019 (Figure 31). Using the relative mass for each fraction, the weighted-average componentry was calculated for grains >125 µm (Figure 32). Across all size fractions, the componentry is dominated by lithic, altered, and hydrothermal material, with juvenile, and red/oxidized clasts representing smaller but variable proportions.

In the 125–250 µm and 250–500 µm size fractions, hydrothermal particles and lithics are

consistently the dominant components, together accounting for 60–90% of the all the components. Juvenile material is present in low proportions in these size fractions for most events (<10%), with a notable peak on March 9, 2017 where it reaches up to 28%. Note that the altered fraction for this event is also relatively high, reaching 40%. In these two smallest (125–500 µm) fractions, the hydrothermal component tends to decrease over time after early 2016 dropping from 48% to 15% and staying low until at least 2019. In the 500–1000 µm size fraction, lithics are the most abundant component for most eruptions, often exceeding 50%, while hydrothermal material is still present but with a slightly reduced proportion compared to finer fractions. In this 500–1000 µm size fraction, the juvenile content remains variable and generally low, except for higher proportions observed on Mar 9, 2017, and Oct 9, 2018. In the >1000 µm size fractions, hydrothermal and lithic clasts dominate, while juvenile material makes up a minor component. Note that only a limited number of events had sufficient coarse material to analyze these larger size fractions.

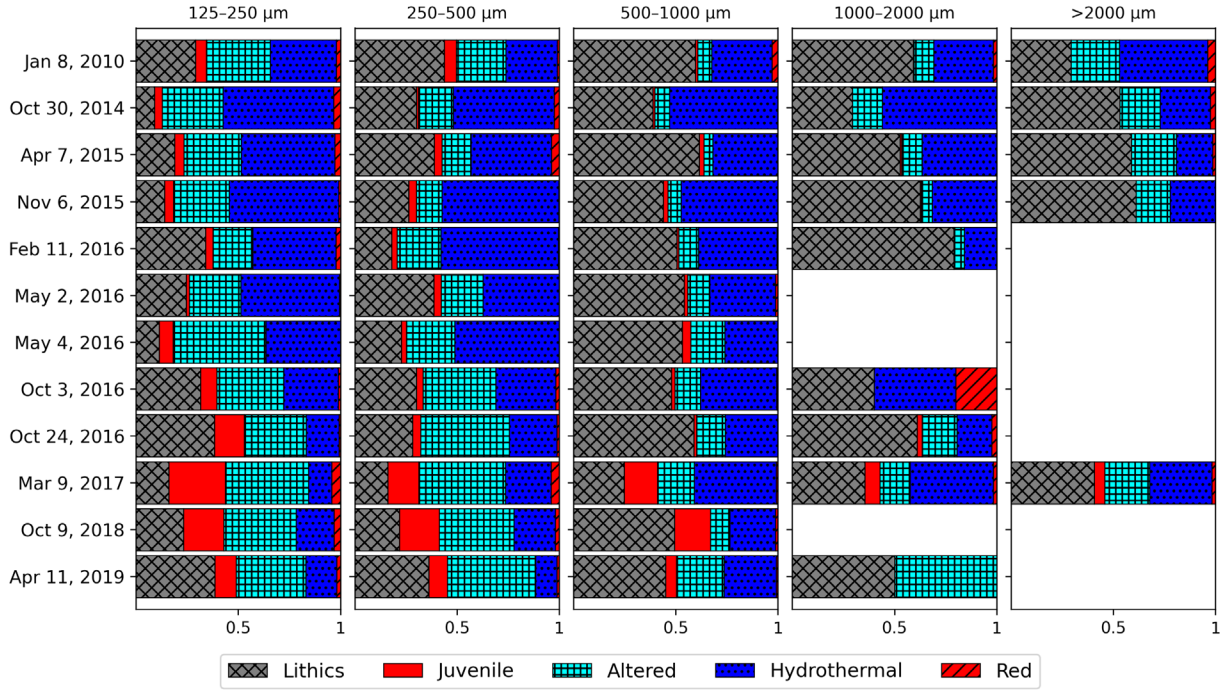

Figure 31. Componentry of individual size fractions for all the samples analyzed. Note that blank spaces mean that there was no physical sample to analyze.

When calculating a weighted averaged for particles >125 µm for each sample (Figure 32), lithics and hydrothermal clasts together represent the majority of the material throughout the entire eruptive sequence (45–24% and 52–16%, respectively). Hydrothermal material is especially prominent from 2010 to 2016. Conversely, juvenile fractions are generally low (<5%) in earlier events and increase up to 10–20% during later events (2017–2019), with two events (Mar 9, 2017, and Oct 9, 2018) exhibiting especially high juvenile components (15–20%). Altered clasts are present throughout the analyzed period, ranging from 11–35% and reaching their highest values toward the end of the analyzed period. Finally, red/oxidized material remains minor throughout (< 4%).

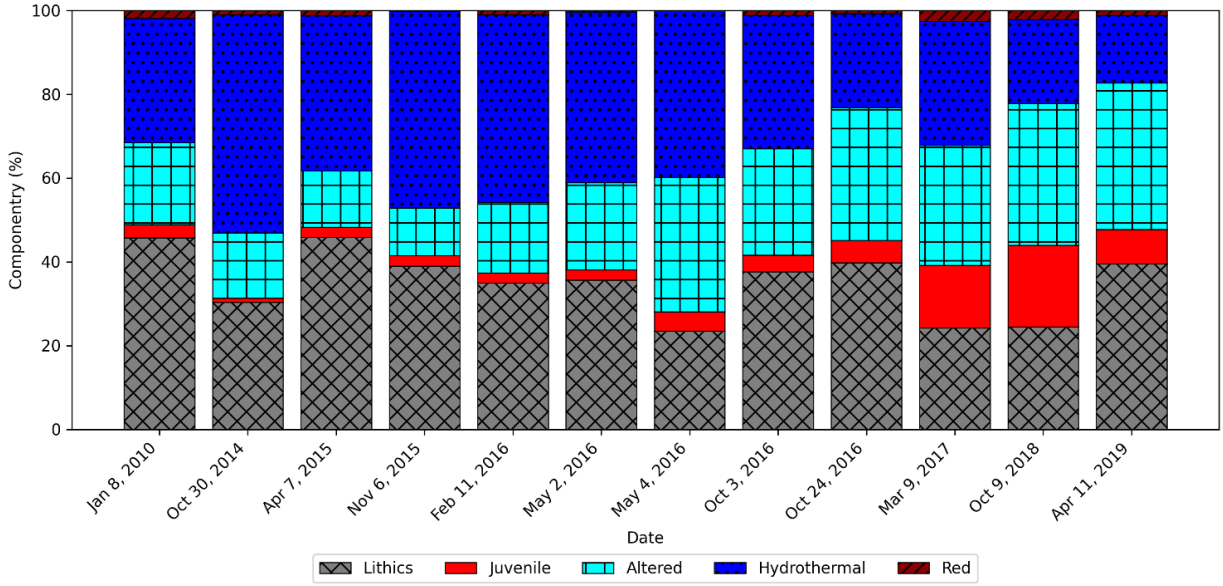

Figure 32. Componentry percentage of the whole samples obtained via weighted average using the componentry of each size fraction and its relative volume contribution to the whole sample.

3.3 Density

Average particle densities range from 2.3 to 2.8 g·cm^{-3} throughout the eruptive sequence (Table 6). During the 2010–2013 interval, densities are lower (2.3–2.6 g·cm^{-3}) and show the highest variation (10.1 %), reflecting less uniform material properties in early deposits (Figure 33).

Table 6. Density measurements. np= not possible, no sample = no particle in that grain size fraction.

Sample collection date	Density ($g \cdot cm^{-3}$)							
	>2000 µm	2000-1000 µm	1000-500 µm	500-250 µm	250-125 µm	125-63 µm	63-32 µm	<32 µm
Jan 8, 2010	2.59	2.70	2.67	2.67	2.58	2.46	np	np
Jan 19, 2012	np	2.58	2.59	2.54	2.39	np	np	np
May 21, 2013	np	2.29	2.28	2.29	2.27	2.22	np	np
May 21, 2013	2.59	2.59	2.60	np	np	np	np	np
Oct 30, 2014	2.43	2.48	2.48	2.46	2.48	2.51	2.63	2.69
Nov 6, 2015	2.79	2.64	2.55	2.54	2.52	2.51	2.50	2.55
Feb 11, 2016	no sample	np	2.43	2.46	2.46	2.47	2.54	2.55
May 2, 2016	no sample	no sample	np	2.52	2.46	2.49	2.53	2.60
May 4, 2016	no sample	no sample	np	2.52	2.55	2.61	2.55	2.61
Oct 3, 2016	no sample	np	2.49	2.56	2.62	2.58	2.59	2.62
Oct 24, 2016	no sample	np	np	2.65	2.70	2.68	2.68	2.66
Nov 1, 2016	no sample	np	2.55	2.68	2.73	2.74	2.73	2.73
Nov 7, 2016	no sample	no sample	2.53	2.67	2.70	2.71	2.71	2.70
Nov 7, 2016	no sample	no sample	np	2.69	2.75	2.76	2.77	2.75
Nov 9, 2016	no sample	no sample	2.64	2.69	2.76	2.76	2.72	2.75
Nov 10, 2016	no sample	no sample	2.65	2.77	2.80	2.80	2.79	2.81
Nov 16, 2016	no sample	np	2.69	2.77	2.78	2.80	2.77	2.77
Nov 22, 2016	no sample	no sample	np	2.62	2.68	2.69	2.66	2.64
Mar 9, 2017	2.69	2.67	2.68	2.72	2.84	2.73	2.72	2.64
May 15, 2017	no sample	no sample	np	2.69	2.72	2.72	2.69	2.66
Oct 9, 2018	no sample	no sample	np	2.64	2.69	2.67	2.64	2.56
Feb 12, 2019	no sample	no sample	no sample	np	2.61	2.64	2.64	2.64
Mar 26, 2019	no sample	no sample	no sample	2.60	2.70	2.71	2.71	2.71
Apr 11, 2019	no sample	np	2.61	2.69	2.74	2.70	2.69	2.67

From late 2014 through 2017, densities increase from 2.4 $g \cdot cm^{-3}$ to 2.8 $g \cdot cm^{-3}$ with less variability and, most samples clustering with around 2.7±0.5$g \cdot cm^{-3}$ in the late 2016 and early 2017. Later in 2017 and in 2018–2019, densities stabilize further (2.6±0.5 $g \cdot cm^{-3}$). The inset plot in Figure 33 highlights the March 2016–March 2017 period, during which densities increased from 2.4 to 2.8 $g \cdot cm^{-3}$ from Feb 2016 to Dec 2016 and then decrease in 2017 to ~2.7 $g \cdot cm^{-3}$. Over all samples, densities tend to decrease with sieve fraction. No systematic relationship was observed between vent distance and density, as both low and high values occur across all distances and size classes.

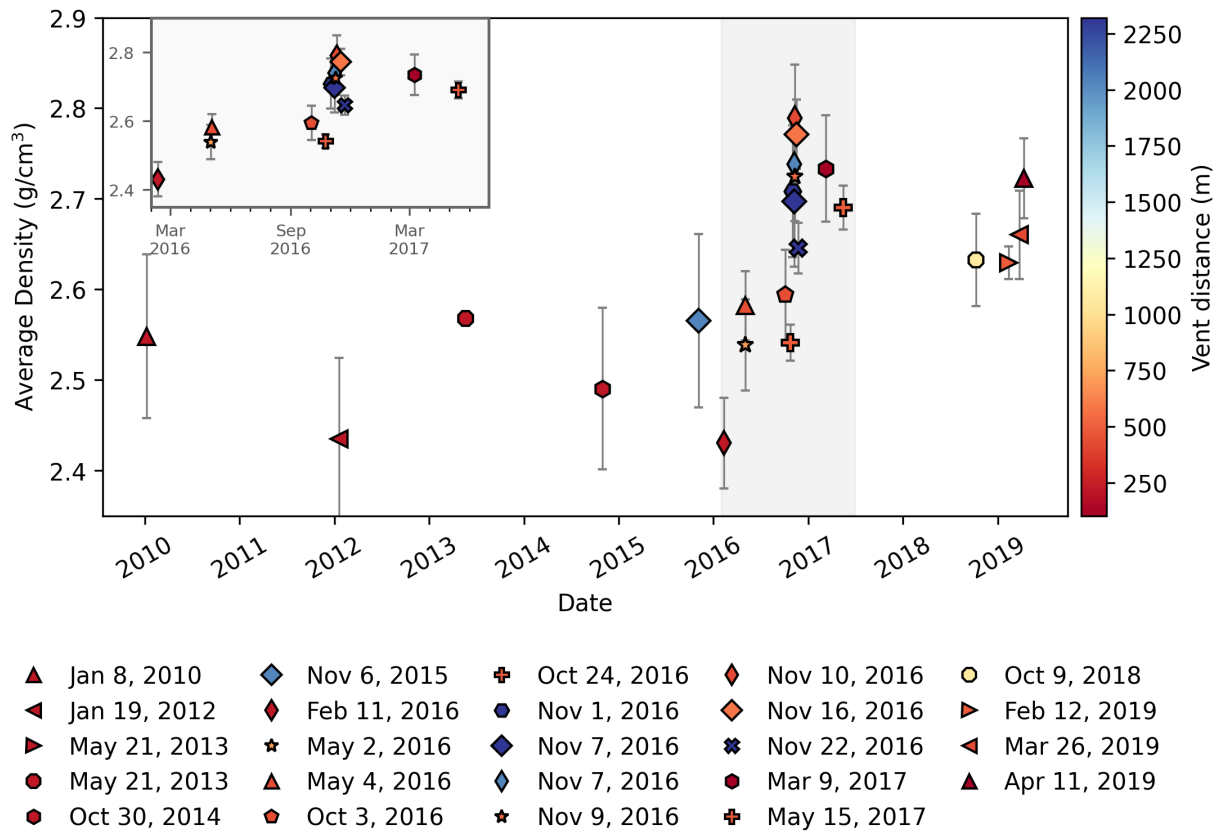

Figure 33. Density averaged over all grain sizes with one standard deviation shown in gray bars. Where not visible, the error bar is smaller than the symbol itself. The inset plot is a closeup view of the gray area in the main plot.

4. Discussion

We discuss here the main trends described in Section 3, the relationships between particle parameters (size, componentry, density), and their evolution with time during the 2010–2019 period covered. We compare these trends to those observed during the 2016-2019 eruptive period at Poás volcano (Cascante et al., 2025) and provide preliminary interpretations concerning sub-surface processes.

4.1 Influence of sample location on ash physical parameters

In general, ash size, componentry, and density all vary with plume height, distance from the vent at which samples are collected, wind direction, and wind intensity. Above the crater at Turrialba volcano, the mean wind heading is about 90-110 (i.e., blowing to the W-WNW) during

the period analyzed, and its intensity is relatively low (~6-12 m/s, ECMWF Reanalysis v5). In our sample collection, although downwind proximal sites (0–500 m W of the volcano) indeed host the coarsest D50 values (e.g., ~ 400 μm at distances of 220 m), and upwind samples are finer at comparable ranges (e.g., 51 μm at 175 m NE of the vent), one of the furthest samples collected at >2 km downwind from the vent on Jan 5, 2010 and deposited from an intermediate size plume (1 km), still exhibits one of the coarsest median diameters (210 μm). Conversely, the sample collected the closest site upwind from the vent on Oct 30, 2014, and which was produced by the highest plume measured (4 km), is one of the finest, with a median diameter of 51 μm. Thus, although they exist, there needs to be more analysis of the different samples from the same eruption to fully establish correlations between plume height, distance from the vent and median diameter in our samples.

4.2 Componentry and density

Turrialba componentry for the period of study (2010–2019) is persistently dominated by lithic, hydrothermal, and altered material across size fractions, with juvenile generally accounting for <10% of the particles early, and increasing to only 10–20% in some 2017–2019 events (Figure 31). Weighted averages show hydrothermal dominance through 2016 but continuously decreasing from Oct 2014 to until at least 2019. There is a modest rise in juvenile component in 2017–2018, following an increase in lithic component in Oct 2016. The proportion of altered clasts increases from 2016 to 2019 (Figure 32). Particle densities of early deposits are lighter (2.35–2.60 $g \cdot cm^{-3}$; 10% variation), by mid-sequence particles are denser (2.55–2.80 $g \cdot cm^{-3}$; 9% variation), and post-2017 densities somewhat stabilized (2.55–2.70 $g \cdot cm^{-3}$; ~6% variation) (Figure 33).

During the 2016–2019 period of unrest, Poás volcano exhibits a more pronounced change in componentry than at Turrialba volcano; hydrothermal-rich ash (Aug 2016 average ash density of

2.3 g·cm^{-3}) followed by juvenile-rich components in 2017 that also show an increase in the density to 2.6 g·cm^{-3} by April 14, implying dry-magmatic pulses in 2017 (juvenile 70%), before settling into a steady recycled-rich, with fines-dominated activity in 2019, with density lower than in 2017 (2.3–2.5 g·cm^{-3}) (Cascante et al., 2025). Thus, although not as noticeable as at Poás volcano, the overall trend in componentry and density at Turrialba is the same: decrease in hydrothermal component throughout the period studied, increase in lithic component before a 'magmatic' phase corresponding to an increase in density, and an increase in altered material after the magmatic phase.

4.3 Fragmentation processes

As seen in Chapter II, explosive magmatic fragmentation produces particle size distributions that can be describe by a power-law relationship of the form $N = \lambda d^{-D}$, where N is the number of particles greater than size d, λ is a scaling factor, and D is the fractal dimension (Kaminski and Jaupart, 1998; Turcotte, 1997). Primary fragmentation typically yields D values around 2.5 ± 0.3 (e.g., Giachetti et al., 2021; Gonnermann, 2015; Kueppers et al., 2006), while secondary fragmentation can increase D beyond 3 (Dufek et al., 2012; Kaminski and Jaupart, 1998). The cumulative number distributions for Turrialba (Figure 34, the fractal dimension D is obtained as the slope of the log(N) when plotted as a function of log(d)) exhibit exponential trends with power-law segments at sizes <250 μm. We calculate the fractal dimension for every sieve size between 2–250 μm (i.e., 2–63 μm; 63–125 μm; 125–250 μm; 250–500 μm; Figure 34).

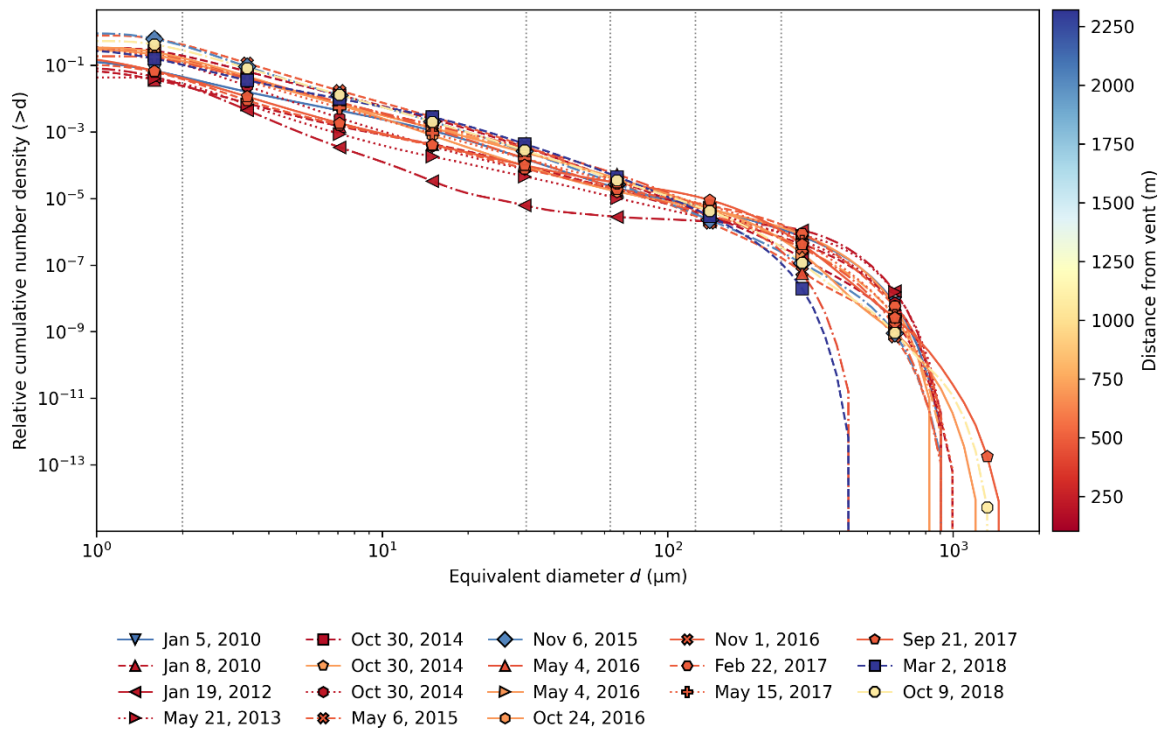

Figure 34. Relative cumulative number density of particles greater than d per m³. Dotted lines correspond to the <250 μm fraction over which we calculate the fractal dimension (D).

At Poás volcano the fractal dimension (D) is directly related to the componentry (Cascante et al., 2025). D = 2.2–2.8 when the samples are dominated by fresh juvenile material, consistent with primary magmatic fragmentation, whereas hydrothermal-dominated samples reach D ~ 3.2, and recycled-rich ash systematically exceed D > 4, pointing to more efficient secondary fragmentation (abrasion/milling, wall collisions) and/or magma–water interaction.

Like Poás, the fractal dimension at Turrialba is also correlated with the median diameter of the particles, being higher (>3) for D50 ≲ 70 μm and below 2 for D50 ≳ 250 μm. Coarse material (D50= 376–207 μm) corresponds to early events (2010–2014), and has average fractal dimensions <2.3 (Figure 35); whereas broad, fines-rich ash (D50 = 32–71 μm) are samples from 2015 and 2018 and have average D >3 (Figure 35), showing enhanced secondary comminution and/or wet fragmentation.

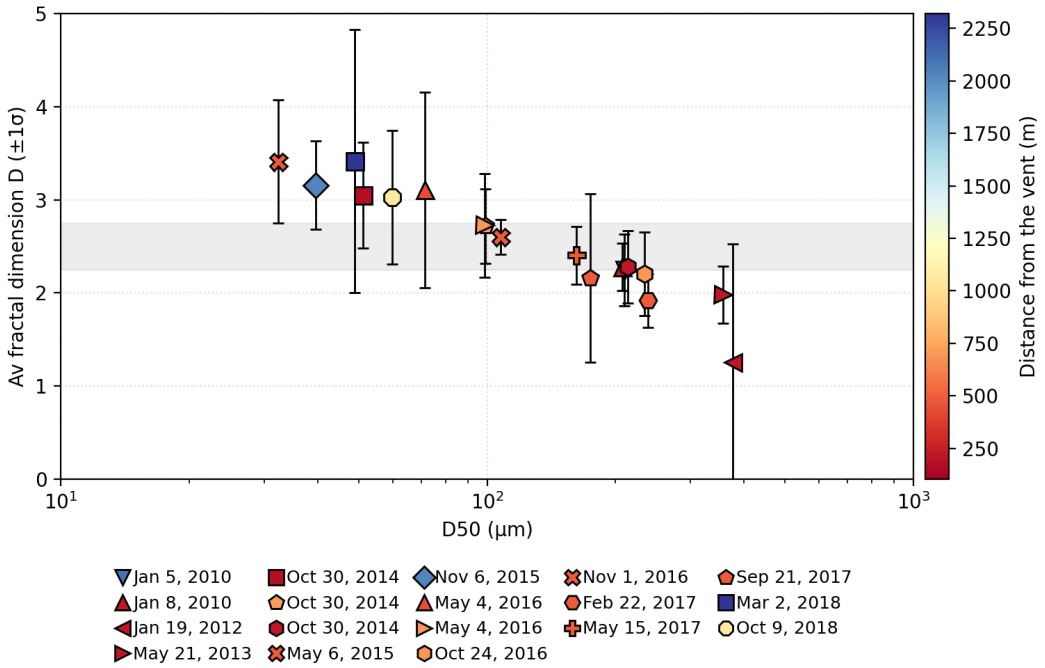

Figure 35. Average fractal dimension (D) versus median equivalent diameter (D50) in μm. Error bars are equal to one standard deviation. Rectangle corresponds to the values in which the fractal dimension equals primary fragmentation.

The componentry at Turrialba volcano does not cover the entire size range. However, we can compare the average weighted componentry and expect that results will vary some with the addition of finer sizes, but that the general trend may remain. Turrialba volcano componentry is like Poás volcano and mainly comprises hydrothermal, lithic, recycled/altered material, and juvenile components. However, Turrialba maximum juvenile contents are 15 and 20% during Mar 9, 2017 and Oct 9, 2018, respectively (Figure 32), whereas the juvenile fraction is close to 80% during the magmatic phase at Poás.

Contrary to Poás, Turrialba volcano early samples (for 2010–2014) exhibit low fractal dimensions (D = 1.3–2.3; Figure 36). These characteristics could indicate inefficient fragmentation during shallow hydrothermal seal failures like the one proposed by de Moor et al. (2016), Mick et al. (2021), and Stix and de Moor (2018). The relationship between fractal dimension and median grain size reinforces the interpretation that coarse deposits are associated with low D values, while

finer-grained deposits correspond to higher D values, reflecting higher fragmentation efficiency.

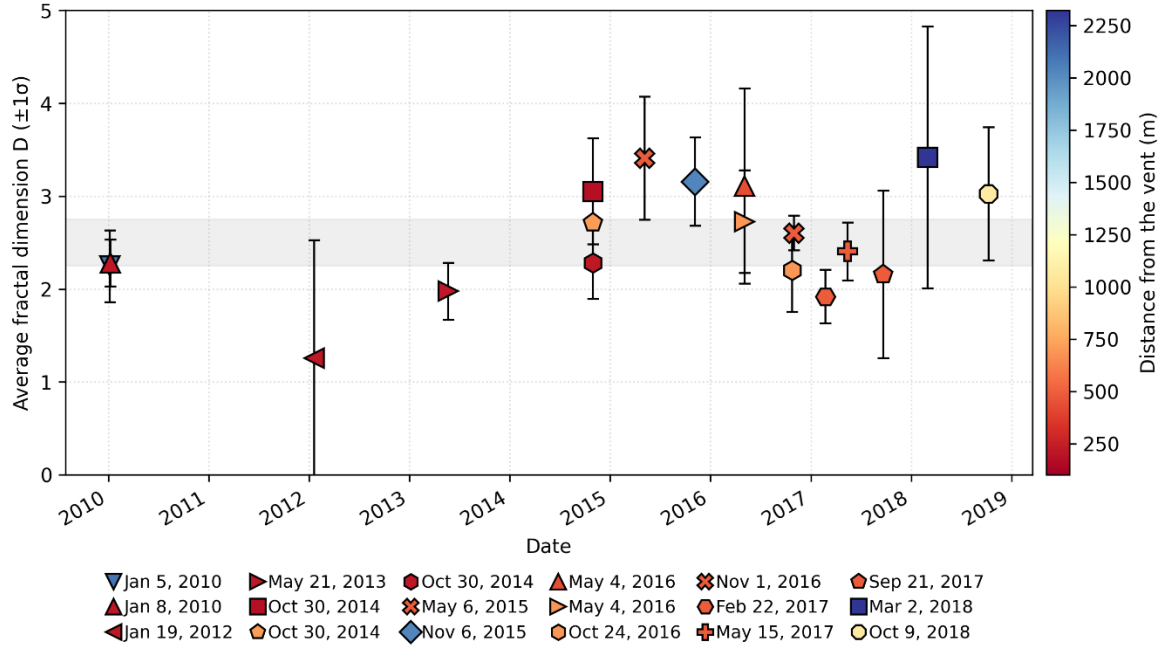

Figure 36. Average fractal dimension (D) as a function of time. Error bars are one standard deviation, and the gray rectangle represents the value of primary fragmentation.

4.4 Temporal evolution of ash properties and eruptive activity

Early in the studied eruption sequence (2010–2013), grain-size distributions are coarse and variable, with lower fractal dimensions and broad cumulative number distributions (Figure 35). These deposits are dominated by lithic and hydrothermal material and display relatively low to moderate densities with large variability. According to Mick et al. (2021) the majority of the hydrothermal breccias that seal the system are made out of SiO_2 polymorphs and gypsum; these minerals have densities of 2.27 $g \cdot cm^{-3}$ and 2.3 $g \cdot cm^{-3}$, respectively ("Mineral data," n.d.). The identification of strong hydrothermal component is consistent with lower density values (Table 6, Figure 33) and with interpretation of shallow hydrothermal overpressure events, where fragmentation is inefficient (fractal dimension of ~2.2) and governed by the sealing and pressurization of the hydrothermal system (Stix and de Moor, 2018).

Eruptions between 2014 and 2016 show mixed componentry (juvenile, hydrothermal and

lithics) and intermediate *D* values (2.5–3), consistent with phreatomagmatic activity where magma interacts with hydrothermal fluids, increasing fragmentation efficiency compared to purely phreatic events (Houghton et al., 2015). This coincides with mixed grain-size modes, increasing fractal dimensions, and a progressive stabilization of density.

Magmatic open-vent eruptions (2016–2017) show increased juvenile fractions (10–20%), average medium grain size of ~150 μm (±50 μm), density values stay at high values (2.6–2.7 $g \cdot m^{-3}$), and *D* values within the range expected for primary magmatic fragmentation (2.25–2.75). By late 2016–2017, juvenile fractions increase, fractal dimension stabilizes between 2.5 and 3.5 (Figure 36), and grain-size distributions between eruptions. This marks the transition to an open vent magmatic regime, characterized by sustained degassing and a stable conduit structure.

The latest events (2018–2019) are characterized by high altered fractions (or recycled? fragments) and higher juvenile contents, D values above 3, and fine grain sizes. These characteristics are consistent with secondary fragmentation and mechanical comminution during low-energy explosions. These trends highlight the connection between fragmentation efficiency (fractal dimension), density, grain size, and componentry evolution, and support the interpretation that changes in ash physical properties track conduit processes during unrest.

4.5 Integration with monitoring signals

Temporal trends in ash properties align with increases in tremor and LP seismicity and transitions in gas ratios (de Moor et al., 2016a; van der Laat et al., 2022). Early phreatic events between 2010–2013 occurred during periods of low tremor and high H_2S/SO_2 ratios. The deposits coincide with hydrothermal-rich ash and coarse grain size distributions (inefficient fragmentation), consistent with sealed-system pressurization and fluid movement.

The transition to open-vent behavior after 2016 is reflected in the decrease of hydrothermal

material in the deposits, sustained seismic tremors, and persistent SO_2 degassing (Table 3). In combination with denser particles and slightly higher juvenile proportions, this indicates a more efficient degassing and a clearer conduit. However, at Turrialba, the increase in juvenile proportion (10–20%) is small relative to Poás (up to 80%). These correlations demonstrate that ash properties provide an independent proxy for subsurface processes, complementing real-time seismic and gas monitoring. Componentry, density, and grain-size distributions preceded or coincided with major changes in degassing behavior, underscoring their forecasting potential.

For operational monitoring, these findings demonstrate the value of rapid ash characterization at hydrothermally influenced open-vent volcanoes. At Turrialba, subtle increases in juvenile content, shifts in grain-size distribution and rising fractal dimension signaled the transition from hydrothermal to phreato-magmatic to magmatic activity. This makes fractal dimensions and related grain-size metrics powerful early indicators of changing eruption style. Because these metrics are derived from standard ash collection and laser diffraction techniques, they can be rapidly integrated into observatory workflows, providing near-real-time information to complement gas and seismic networks.

5. Conclusions

Turrialba products of the 2010–2019 eruptive cycle shows a clear progression from hydrothermal-seal failure to a more open-vent influenced conduit. Early deposits are coarse, hydrothermal/altered material dominated, low-density, and have low fractal dimensions (inefficient fragmentation). During 2014–2017, ash density increases while hydrothermal fractions decrease, juvenile fractions modestly increase. After 2016, densities and fractal dimensions are more consistently in intermediate ranges, consistent with sustained open-vent degassing. These changes correlate with geophysical and gas monitoring signals. High H_2S/SO_2 and low tremor accompany

the early phreatic phase; increasing LP/tremor with rising CO_2/SO_2 mark growing magmatic input; persistent SO_2 and harmonic tremor coincide with open-vent conditions.

Compared with Poás volcano during the eruptive episodes in 2016–2019, the same trends apply, but with smaller juvenile input at Turrialba. Poás undergoes a sharper change to juvenile rich, magmatic fragmentation and then to secondary fragmentation, whereas Turrialba remains hydrothermal/altered dominated with only modest juvenile increases. This reflects differences in conduit dynamics and hydrothermal system persistence but also confirms the general applicability of median grain size, fractal dimension, and componentry metrics for tracking eruptive transitions at hydrothermally influenced volcanoes.

The results from Turrialba volcano suggest a longer-lived, hydrothermal-buffered conduit where juvenile contributions increase only in small amounts. Poás volcano more clearly transitions from hydrothermal-dominated to juvenile-rich, comparatively “dry” magmatic activity and then back toward eruptions in which recycled material is more dominant.

CHAPTER V

5. CONCLUSIONS

This dissertation demonstrates that the physical properties of volcanic ash are compelling indicators of transitions in periods of volcanic unrest. Across three chapters, changes in grain size metrics, componentry, and density correspond with these transitions in eruptive episodes.

Chapter 2 examines eruptions at Poás volcano during 2016–2019 and shows the progressive excavation of a hydrothermal system as well as the transition from fluid-driven to magmatic explosions and finally to the production of recycled, fine-grained ash. Early explosions (August 2016–April 2017) were dominated by hydrothermally altered particles (65–25 vol.%) and low juvenile content (<25 vol.%), suggesting small phreatomagmatic explosions driven by hydrothermal seal failure. Juvenile-rich deposits were coarser grained (up to 80 vol.% juvenile, >100 μm), reflecting primary fragmentation processes. In contrast, deposits dominated by recycled fragments were fine grained (>56 vol.% recycled, <24 μm), indicating re-fragmentation of pre-existing material.

Chapter 3 shows that traditional stereomicroscopic classifications overestimate the percentage of juvenile particles. Componentry corrections based on SEM-cross section will improve the accuracy of interpretations in early phreatic eruptions, where juvenile signatures can be subtle or non-existing. With these componentry corrections, 50–96% of presumed juvenile grains are reclassified as altered or lithic material. Moreover, in chapter 3, particle morphology (e.g., solidity, convexity, axial ratio, form factor) shows trends to differentiate juvenile material with other types of particles (hydrothermal, altered and/or lithics). For example, juvenile material tends to be less convex and have lower solidity but cannot replace SEM cross-sectional verification.

In the last chapter findings show that during 2010–2019 Turrialba volcano eruptions,

densities during early eruptions 2010–2013 evolve from lower (2.3–2.6 g·cm^{-3}) to higher (2.6–2.8 g·cm^{-3}) in 2016–2017 and then remain comparatively steady in 2019 (2.6–2.7 g·cm^{-3}), consistent with a progressively opening conduit and reduced hydrothermal dominance. Componentry is constantly hydrothermal-altered-lithic dominated with subtle juvenile increases (10–20 %) in 2017–2019. Fractal dimension (D) of cumulative number density correlates to eruptive processes. Coarse deposits with low D=1.3–2.3 reflect inefficient fragmentation consistent with a hydrothermal seal failure. Fine-rich deposits with high D≥3 reflect magma-water interaction and/or recycling of previous material.

In summary, this research establishes a transferable framework for operational ash monitoring that can be applied to other similar volcanoes worldwide, expanding understanding of shallow conduit processes.

APENDIX A

1. SUPPLEMENTARY MATERIAL FOR CHAPTER II

Supplementary material

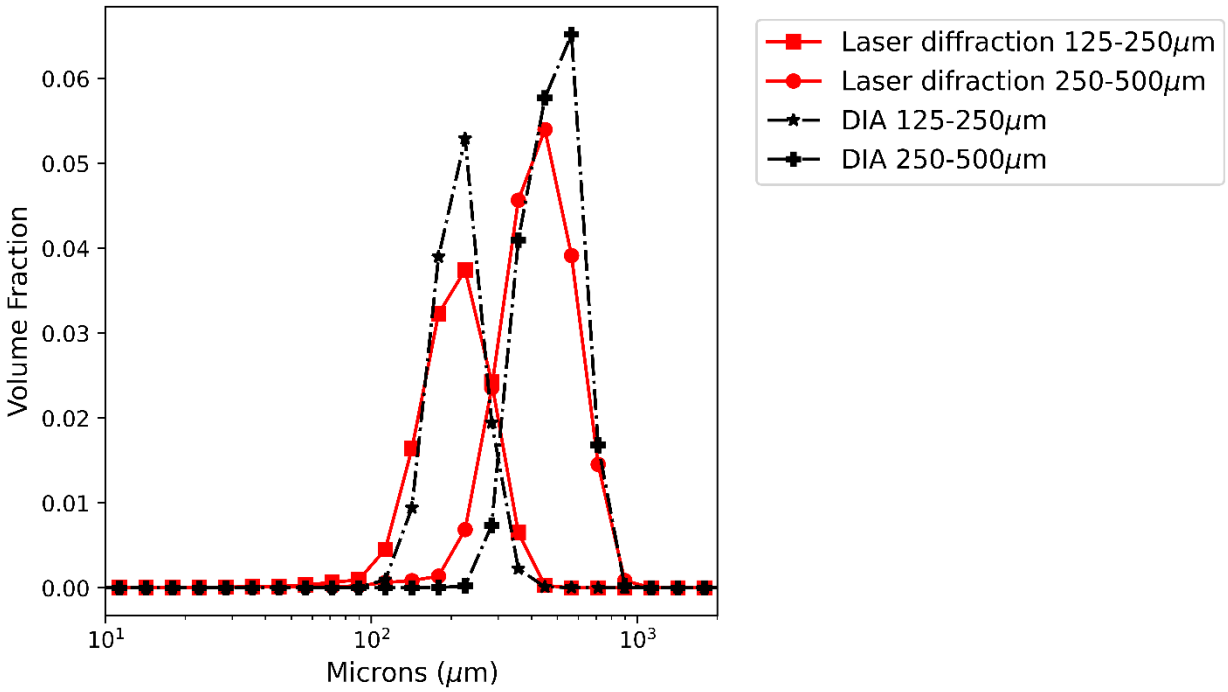

Supplementary Figure 1. Comparison of the volume fraction as a function of the particle size obtained by dynamic imaging analysis (DIA) and laser diffraction techniques in the sample from April 22, 2017. DIA provides narrower distributions slightly skewed toward larger sizes compared to laser diffraction, but the median diameters obtained with the two techniques are within 1% (125–250 μm size fraction) and 11% (250–500 μm size fraction) of one another. These discrepancies could be in part explained by the difference in the size parameter measured: DIA measures dry grain outlines and assumes ellipsoidal shapes, whereas laser diffraction measures the scattering of light due to (assumed) spherical grains that have been dispersed in water.

Supplementary Table 1. Summary of the characteristics of the six components identified in the twenty samples and used for componentry analysis.

Category	**Description**
Juvenile	Glossy appearance and semi-vesicular. Translucent-transparent and/or black in color.
Red Juvenile	Semi-vesicular, glossy, or dull. Red in color.
Lithics	Dull, opaque luster. Identical in character to the deposits of older eruptive episodes at the volcano, and from other basement rocks.
Recycled	Dull-opaque-like appearance, round edges. Sometimes presence of clay or oxidation of surface. Translucent-transparent and/or black in color.
Hydrothermal	Based on color and luster (including metallic luster, sulfide minerals, white color that is characteristic of gypsum and anhydrite).
Crystals	Free crystals, inferred to be of juvenile or lithic origin.
Aggregates	Clumps of smaller grains, inferred to be preserved remnants of primary aggregation during plume transport.

Supplementary Table 2. Major elements compositions of the groundmass glass of juvenile particles from explosions on Aug 4, 2017, April 22, 2017, and Feb 11, 2019, at Poás. For each eruption, the number in the spot name refers to a specific juvenile grain (6 to 7 grains per explosion), and the letter to a spot on that grain (2 spots on each grain). For the juvenile material of the 1955 eruption, spots were collected on seven fragments from a single, crushed bomb. Whole rock (WR), XRF data collected on bombs from the 1955 eruption (Prosser and Carr, 1987; de Moor et al. 2019) and the April 22, 2017, eruption (de Moor et al. 2019) are also provided. Values for all are normalized to 100 wt.%.

Spot name	Na_2O	SiO_2	K_2O	Al_2O_3	FeO	MgO	CaO	MnO	S	Cl	TiO_2	P_2O_5
08/04/16-1a	3.18	61.15	2.38	13.43	9.43	2.81	5.68	0.18	0.01	0.18	1.3	0.27
08/04/16-1b	4.59	59.72	1.93	15.69	8	1.97	6.32	0.16	0.01	0.16	1.2	0.26
08/04/16-2a	3.53	61.43	2.73	13.77	8.67	2.25	5.74	0.17	0.01	0.16	1.22	0.32
08/04/16-2b	4.13	61.26	1.82	14.91	7.72	2.23	6.12	0.17	0.01	0.14	1.18	0.3
08/04/16-3a	3.36	57.81	1.88	14.02	10.39	3.58	6.99	0.21	0.01	0.15	1.33	0.27
08/04/16-3b	3.39	57.52	1.85	14.41	10.39	3.55	6.96	0.21	0.01	0.14	1.3	0.27
08/04/16-4a	2.68	61.5	2.36	14.02	9.1	2.52	5.77	0.19	0.01	0.19	1.37	0.3
08/04/16-4b	3.54	61.06	2.29	13.61	9.27	2.49	5.78	0.19	0	0.19	1.3	0.29
08/04/16-5a	2.99	57.44	1.86	14.44	10.66	3.63	7.04	0.21	0.01	0.14	1.3	0.27
08/04/16-5b	3.54	57.92	1.98	14.35	10.15	3.43	6.75	0.2	0.01	0.12	1.3	0.27
08/04/16-6a	3.26	57.73	1.88	14.4	10.3	3.48	6.98	0.2	0.01	0.13	1.35	0.27
08/04/16-6b	3.03	57.95	1.93	13.95	10.67	3.52	7	0.21	0	0.13	1.32	0.27
04/22/17-1a	3.02	68.52	3.59	13.6	5.71	0.89	3.03	0.14	0.01	0.14	0.95	0.39
04/22/17-1b	3.34	68.18	3.6	13.66	5.73	0.9	3.03	0.14	0	0.21	0.87	0.34
04/22/17-2a	3.26	68.82	3.68	13.2	5.7	0.81	2.86	0.14	0	0.19	0.96	0.38
04/22/17-2b	3.33	67.64	3.72	13.78	5.99	0.88	3.05	0.15	0	0.11	0.92	0.41
04/22/17-3a	3.87	67.01	3.57	13.98	5.84	0.9	3.19	0.14	0.01	0.23	0.91	0.35
04/22/17-3b	3.88	67.3	3.12	14.01	5.78	0.89	3.46	0.14	0	0.14	0.88	0.4
04/22/17-4a	3.4	66.7	3.47	13.09	6.8	1.06	3.42	0.19	0.01	0.33	0.89	0.64
04/22/17-4b	3.48	67.86	3.54	13.99	5.09	0.73	3.66	0.13	0	0.19	0.87	0.47
04/22/17-5a	3.56	67.29	3.37	13.95	5.65	1.15	3.45	0.14	0	0.16	0.87	0.41
04/22/17-5b	3.73	66.94	3.29	13.98	5.77	1.14	3.52	0.16	0	0.2	0.88	0.39
04/22/17-6a	2.99	67.29	3.31	13.75	6.04	1.22	3.66	0.16	0	0.27	0.91	0.4
04/22/17-6b	2.63	68.64	3.4	14.05	5.38	1.05	3.35	0.15	0.01	0.23	0.83	0.3
04/22/17-7a	3.74	68.84	3.71	13.32	5.3	0.81	2.83	0.13	0	0.17	0.9	0.25
04/22/17-7b	3.38	67.41	3.31	14.28	5.79	0.76	3.51	0.14	0	0.19	0.87	0.35
02/11/19-1a	3.99	62.43	3.58	14.82	6.48	2.08	4.16	0.14	0	0.18	1.48	0.67
02/11/19-1b	3.86	62.53	3.73	14.56	6.67	2.14	4.05	0.13	0	0.17	1.48	0.66
02/11/19-2b	4.56	62.42	3.47	14.4	6.38	2.2	4.1	0.13	0	0.15	1.49	0.7
02/11/19-2b	3.75	62.31	3.54	14.91	6.67	2.26	4.08	0.13	0	0.18	1.48	0.71
02/11/19-3a	3.97	62.47	3.8	14.67	6.57	2.05	4.04	0.12	0	0.11	1.48	0.7
02/11/19-3b	3.73	63.08	3.68	14.53	6.12	2.23	4.12	0.14	0	0.16	1.52	0.67
02/11/19-4a	3.88	63.06	3.54	14.81	6.21	2.03	4	0.13	0	0.15	1.5	0.68
02/11/19-4b	4.17	62.16	3.34	14.64	6.88	2.09	4.27	0.14	0	0.18	1.43	0.68
02/11/19-5a	4.72	61.75	3.22	15.23	6.25	2.01	4.49	0.13	0	0.18	1.38	0.64
02/11/19-5b	3.84	62.82	3.41	14.74	6.47	2.14	4.17	0.12	0	0.19	1.45	0.67

02/11/19-6a	4.72	61.71	3.31	14.72	6.65	2.21	4.23	0.13	0.01	0.17	1.46	0.67
02/11/19-6b	4.26	62.52	3.41	15.15	6.05	2.09	4.05	0.14	0	0.16	1.46	0.7
1955-a	3.62	57.9	1.8	14.65	9.92	3.51	6.75	0.19	0.01	0.14	1.26	0.25
1955-b	3.43	57.63	1.78	14.86	9.96	3.63	6.91	0.19	0.01	0.13	1.24	0.25
1955-c	3.46	57.86	1.86	14.38	10.15	3.57	6.89	0.2	0	0.13	1.27	0.24
1955-d	3.67	58.06	1.75	14.36	10.06	3.43	6.83	0.19	0.01	0.12	1.29	0.24
1955-e	3.38	57.6	1.82	15.05	10	3.5	6.81	0.18	0	0.13	1.27	0.25
1955-f	3.17	57.71	1.71	14.92	10.04	3.67	6.93	0.2	0	0.13	1.29	0.25
1955-g	3.46	57.62	1.83	14.94	9.84	3.6	6.91	0.19	0	0.13	1.25	0.24
1955 WR – P&C 1987	2.97	54.3	1.03	18.07	8.65	4.75	9.15	0.15	-	-	0.8	0.13
1955 WR PO161115R1	2.98	54.57	1.04	18.83	8.22	4.35	8.93	0.15	-	-	0.79	0.14
2017 – WR PO170425R6	3.15	57.29	1.6	17.83	7.71	3.52	7.79	0.16	-	-	0.74	0.21
2017 – WR PO170425R4	3.15	57.54	1.62	17.83	7.62	3.42	7.75	0.16	-	-	0.73	0.2

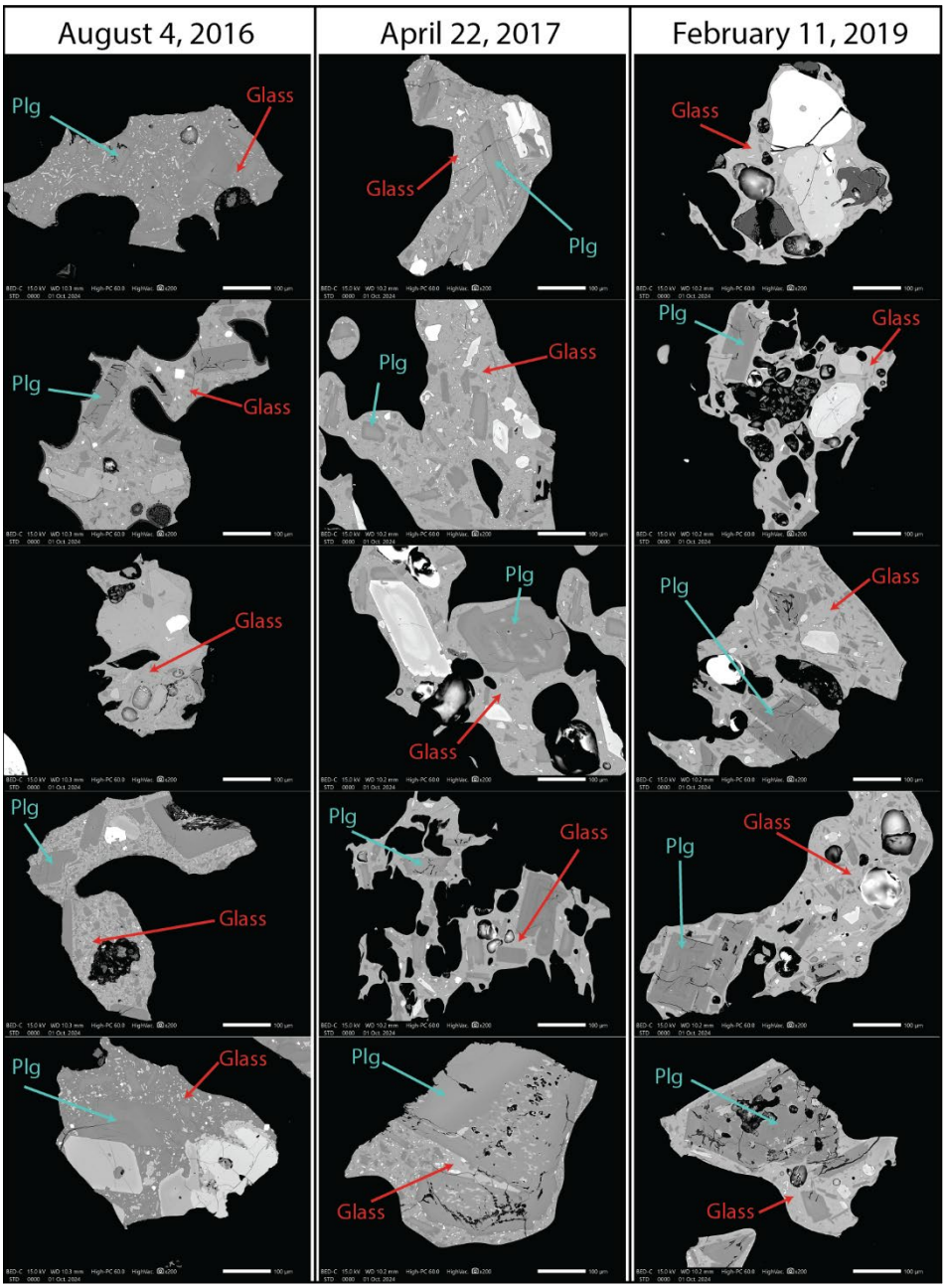

Supplementary Figure 2. Juvenile particles of ash from three eruptions on August 4, 2016, April 22, 2017, and February 11, 2019. The grains are microlite rich and on August 4, 2016 some of the grains appear to be more microlite rich than the other eruptions. The dominant micro-phenocrysts and phenocrysts are plagioclase, pyroxene, and oxides. We analyzed the glass on some of these particles with EMPA.

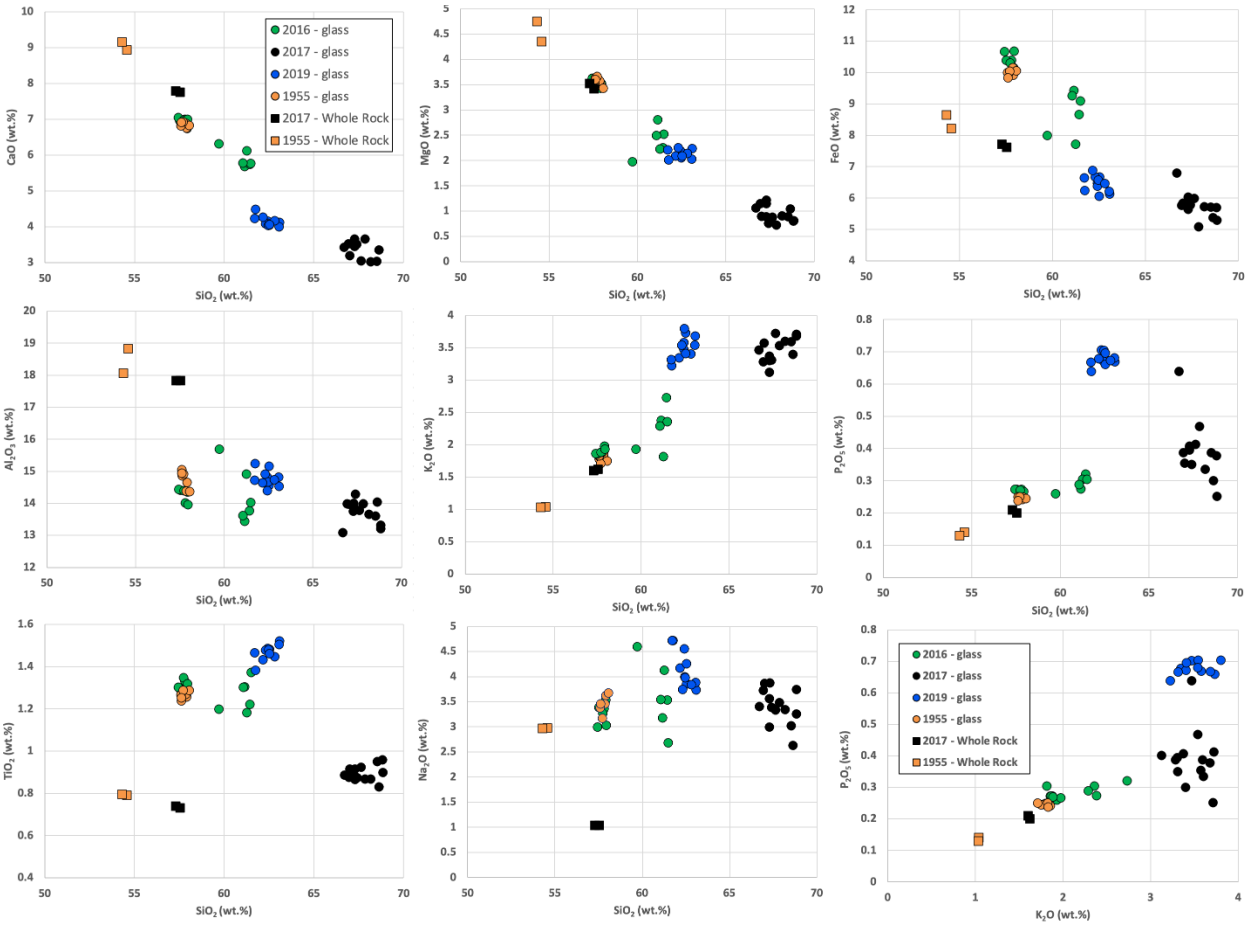

Supplementary Figure 3. Harker diagrams of whole rock and groundmass glass composition of juvenile magma from explosions at Poás in 1955, August 4, 2016, April 22, 2017, and February 11, 2019. Groundmass glass composition was obtained by electronic microprobe in this study whereas whole rock compositions were obtained by x-ray fluorescence by Prosser and Carr (1987, scoria from 1955 eruption) and de Moor et al. (2019, scoria from 1955 and bombs from 2017). Oxides amounts are normalized to 100%.

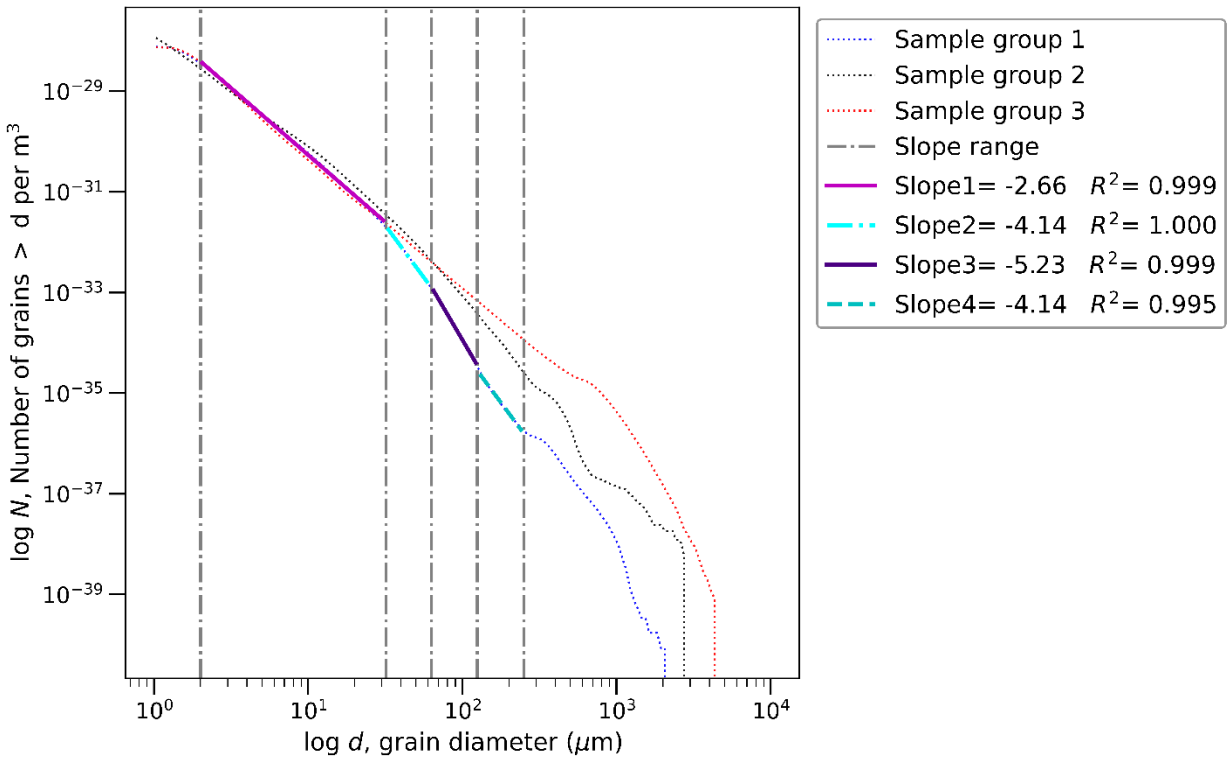

Supplementary Figure 4. Example of the cumulative number density of particles greater for three samples, one for each group identified based on size. The distribution of the sample from group 1 (blue) has been fitted using a power law (straight line on this log-log plot) in four sections (2–32 µm, 32–63 µm, 63–125 µm, and 125–250 µm) to obtain the fractal dimension (absolute value of the slope) of each of this section and then calculate the average and standard deviation of the fractal dimension.

Supplementary Table 3. Median grain diameter, average fractal dimension over the range 2–250 μm, and standard deviation of the fractal dimension (see Supplementary Figure 4). The median grain size corresponds to the 50 percentiles on the cumulative curve (magenta horizontal line on Figure 6d)

Explosion date (M/D/Y)	Median grain size (μm)	Average fractal dimension	Standard deviation of slopes
August 4, 2016	48	3.52	0.56
April 7, 2017	211	2.49	0.26
April 10, 2017	42	4.17	0.92
April 14, 2017	137	2.65	0.22
April 15, 2017	149	2.74	0.45
April 19, 2017	242	2.47	0.28
April 20, 2017	37	4.05	0.68
April 22, 2017	370	2.59	0.05
May 9,2017	317	2.12	0.21
June 11, 2017	63	2.93	0.57
August 30, 2017	22	5.52	4.42
September 13, 2017	130	2.95	0.79
October 30, 2017	23	4.45	3.02
February 8, 2019	16	6.15	1.28
February 11, 2019	24	5.92	2.29
February 12, 2019	18	5.55	1.43
February 14, 2019	16	6.18	3.66
March 7, 2019	19	5.74	1.28
March 18, 2019	21	5.18	0.90
April 30, 2019	20	5.23	0.91

Supplementary Table 4. Componentry data.

Explosion date (M/D/Y)	Weighted average componentry						
	Juvenile	Lithics	Recycled	Hydrothermal	Crystals	Aggregates	Red
August 4, 2016	0.17	0.06	0.13	0.64	0.00	0.00	0.00
April 7, 2017	0.12	0.29	0.16	0.43	0.00	0.00	0.00
April 10, 2017	0.19	0.06	0.35	0.35	0.05	0.00	0.00
April 14, 2017	0.35	0.14	0.32	0.17	0.00	0.00	0.01
April 15, 2017	0.24	0.20	0.35	0.19	0.00	0.00	0.01
April 19, 2017	0.18	0.34	0.20	0.26	0.00	0.00	0.01
April 20, 2017	0.21	0.02	0.66	0.09	0.01	0.00	0.00
April 22, 2017	0.71	0.09	0.15	0.05	0.01	0.00	0.00
May 9,2017	0.72	0.08	0.14	0.05	0.01	0.00	0.00
June 11, 2017	0.32	0.10	0.45	0.10	0.00	0.02	0.03
August 30, 2017	0.46	0.01	0.52	0.00	0.01	0.00	0.00
September 13, 2017	0.70	0.05	0.18	0.05	0.01	0.00	0.01
October 30, 2017	0.28	0.01	0.68	0.01	0.00	0.02	0.00
February 8, 2019	0.23	0.01	0.70	0.06	0.00	0.00	0.00
February 11, 2019	0.23	0.00	0.68	0.08	0.01	0.00	0.00
February 12, 2019	0.24	0.00	0.68	0.08	0.00	0.00	0.00
February 14, 2019	0.30	0.00	0.69	0.01	0.00	0.00	0.00
March 7, 2019	0.34	0.00	0.62	0.02	0.01	0.00	0.00
March 18, 2019	0.33	0.01	0.58	0.01	0.05	0.03	0.00
April 30, 2019	0.29	0.01	0.56	0.03	0.10	0.01	0.00

Supplementary Table 4.1. Continuation of componentry

Explosion date (M/D/Y)	32–63 μm componentry Volume fraction						
	Juvenile	Lithics	Recycled	Hydrothermal	Crystals	Aggregates	Red
August 4, 2016	0.21	0.01	0.15	0.63	0.00	0.00	0.00
April 7, 2017	0.22	0.03	0.37	0.38	0.00	0.00	0.00
April 10, 2017	0.21	0.00	0.47	0.30	0.02	0.00	0.00
April 14, 2017	0.51	0.00	0.46	0.03	0.00	0.00	0.00
April 15, 2017	0.40	0.00	0.52	0.07	0.00	0.00	0.00
April 19, 2017	0.25	0.00	0.69	0.06	0.00	0.00	0.00
April 20, 2017	0.14	0.00	0.78	0.07	0.01	0.00	0.00
April 22, 2017	0.72	0.00	0.23	0.05	0.00	0.00	0.00
May 9,2017	0.62	0.02	0.35	0.02	0.00	0.00	0.00
June 11, 2017	0.25	0.01	0.70	0.04	0.00	0.00	0.00
August 30, 2017	0.43	0.00	0.56	0.00	0.01	0.00	0.00
September 13, 2017	0.60	0.00	0.40	0.00	0.00	0.00	0.00
October 30, 2017	0.26	0.00	0.73	0.01	0.00	0.00	0.00
February 8, 2019	0.21	0.01	0.73	0.05	0.00	0.00	0.00
February 11, 2019	0.21	0.00	0.71	0.07	0.01	0.00	0.00
February 12, 2019	0.24	0.00	0.69	0.07	0.00	0.00	0.00
February 14, 2019	0.28	0.00	0.72	0.00	0.00	0.00	0.00
March 7, 2019	0.31	0.00	0.67	0.01	0.01	0.00	0.00
March 18, 2019	0.33	0.00	0.62	0.00	0.05	0.00	0.00
April 30, 2019	0.27	0.00	0.60	0.02	0.11	0.00	0.00

Supplementary Table 4.2. Continuation of componentry

Explosion date (M/D/Y)	63–125 μm componentry Volume fraction						
	Juvenile	Lithics	Recycled	Hydrothermal	Crystals	Aggregates	Red
August 4, 2016	0.06	0.11	0.11	0.71	0.00	0.00	0.00
April 7, 2017	0.16	0.16	0.12	0.54	0.00	0.00	0.00
April 10, 2017	0.15	0.17	0.17	0.41	0.09	0.00	0.00
April 14, 2017	0.30	0.05	0.42	0.20	0.01	0.00	0.02
April 15, 2017	0.24	0.06	0.49	0.19	0.00	0.00	0.02
April 19, 2017	0.31	0.20	0.12	0.35	0.00	0.00	0.02
April 20, 2017	0.41	0.02	0.38	0.16	0.01	0.00	0.02
April 22, 2017	0.77	0.01	0.11	0.06	0.05	0.00	0.01
May 9,2017	0.77	0.02	0.15	0.05	0.00	0.00	0.01
June 11, 2017	0.47	0.16	0.08	0.20	0.00	0.00	0.09
August 30, 2017	0.70	0.03	0.23	0.01	0.00	0.00	0.03
September 13, 2017	0.71	0.04	0.18	0.05	0.01	0.00	0.02
October 30, 2017	0.51	0.03	0.44	0.01	0.00	0.00	0.01
February 8, 2019	0.42	0.03	0.42	0.14	0.00	0.00	0.00
February 11, 2019	0.51	0.04	0.16	0.25	0.00	0.00	0.03
February 12, 2019	0.24	0.02	0.54	0.20	0.00	0.00	0.00
February 14, 2019	0.48	0.02	0.39	0.10	0.00	0.00	0.01
March 7, 2019	0.55	0.01	0.41	0.02	0.00	0.00	0.01
March 18, 2019	0.42	0.05	0.42	0.09	0.00	0.00	0.02
April 30, 2019	0.56	0.11	0.27	0.04	0.00	0.00	0.01

Supplementary Table 4.3. Continuation of componentry

Explosion date (M/D/Y)	125–250 μm componentry Volume fraction						
	Juvenile	Lithics	Recycled	Hydrothermal	Crystals	Aggregates	Red
August 4, 2016	0.05	0.23	0.06	0.65	0.00	0.00	0.00
April 7, 2017	0.11	0.35	0.11	0.43	0.00	0.00	0.00
April 10, 2017	0.12	0.15	0.06	0.53	0.13	0.00	0.00
April 14, 2017	0.35	0.15	0.22	0.23	0.01	0.00	0.03
April 15, 2017	0.25	0.08	0.37	0.29	0.00	0.00	0.02
April 19, 2017	0.18	0.40	0.12	0.29	0.01	0.00	0.01
April 20, 2017	0.58	0.08	0.15	0.17	0.00	0.00	0.02
April 22, 2017	0.79	0.05	0.10	0.04	0.02	0.00	0.01
May 9,2017	0.78	0.07	0.08	0.06	0.01	0.00	0.01
June 11, 2017	0.36	0.29	0.15	0.14	0.00	0.01	0.04
August 30, 2017	0.71	0.04	0.23	0.01	0.00	0.00	0.01
September 13, 2017	0.75	0.05	0.10	0.08	0.01	0.00	0.01
October 30, 2017	0.38	0.14	0.15	0.00	0.02	0.30	0.00
February 8, 2019	0.34	0.04	0.34	0.28	0.00	0.00	0.00
February 11, 2019	0.29	0.21	0.12	0.38	0.00	0.00	0.00
February 12, 2019	0.33	0.12	0.28	0.23	0.03	0.00	0.00
February 14, 2019	0.31	0.12	0.45	0.11	0.00	0.00	0.00
March 7, 2019	0.13	0.22	0.37	0.07	0.05	0.15	0.00
March 18, 2019	0.20	0.14	0.45	0.06	0.02	0.11	0.01
April 30, 2019	0.37	0.22	0.23	0.08	0.00	0.05	0.05

Supplementary Table 4.4. Continuation of componentry

Explosion date (M/D/Y)	250–500 μm componentry Volume fraction						
	Juvenile	Lithics	Recycled	Hydrothermal	Crystals	Aggregates	Red
August 4, 2016	0.04	0.3	0.05	0.6	0.00	0.00	0.01
April 7, 2017	0.08	0.41	0.12	0.39	0.00	0.00	0.00
April 10, 2017	0.10	0.22	0.08	0.60	0.00	0.00	0.00
April 14, 2017	0.19	0.36	0.13	0.29	0.00	0.00	0.02
April 15, 2017	0.15	0.48	0.15	0.19	0.01	0.00	0.02
April 19, 2017	0.16	0.44	0.09	0.28	0.01	0.01	0.02
April 20, 2017	0.58	0.16	0.08	0.17	0.01	0.00	0.01
April 22, 2017	0.73	0.11	0.09	0.05	0.01	0.00	0.00
May 9,2017	0.76	0.09	0.05	0.06	0.02	0.00	0.00
June 11, 2017	0.35	0.16	0.15	0.12	0.01	0.20	0.02
August 30, 2017	0.00	0.00	0.00	0.00	0.00	0.00	0.00
September 13, 2017	0.76	0.07	0.06	0.09	0.01	0.00	0.01
October 30, 2017	0.00	0.00	0.00	0.00	0.00	0.00	0.00
February 8, 2019	0.00	0.00	0.00	0.00	0.00	0.00	0.00
February 11, 2019	0.13	0.16	0.13	0.50	0.00	0.05	0.03
February 12, 2019	0.00	0.00	0.00	0.00	0.00	0.00	0.00
February 14, 2019	0.00	0.00	0.00	0.00	0.00	0.00	0.00
March 7, 2019	0.00	0.00	0.00	0.00	0.00	0.00	0.00
March 18, 2019	0.03	0.15	0.07	0.01	0.01	0.73	0.00
April 30, 2019	0.22	0.34	0.12	0.03	0.01	0.25	0.03

Supplementary Table 4.5. Continuation of componentry

Explosion date (M/D/Y)	500–1000 μm componentry Volume fraction						
	Juvenile	Lithics	Recycled	Hydrothermal	Crystals	Aggregates	Red
August 4, 2016	0.00	0.18	0.18	0.64	0.00	0.00	0.00
April 7, 2017	0.07	0.43	0.07	0.43	0.00	0.00	0.00
April 10, 2017	0.05	0.31	0.07	0.51	0.00	0.06	0.00
April 14, 2017	0.14	0.47	0.08	0.28	0.01	0.00	0.02
April 15, 2017	0.08	0.63	0.06	0.21	0.00	0.00	0.02
April 19, 2017	0.07	0.51	0.09	0.31	0.00	0.01	0.02
April 20, 2017	0.14	0.45	0.20	0.21	0.00	0.00	0.00
April 22, 2017	0.66	0.13	0.15	0.04	0.01	0.00	0.00
May 9,2017	0.68	0.14	0.11	0.06	0.01	0.00	0.00
June 11, 2017	0.29	0.39	0.04	0.05	0.00	0.22	0.01
August 30, 2017	0.00	0.00	0.00	0.00	0.00	0.00	0.00
September 13, 2017	0.71	0.14	0.07	0.06	0.01	0.00	0.01
October 30, 2017	0.00	0.00	0.00	0.00	0.00	0.00	0.00
February 8, 2019	0.00	0.00	0.00	0.00	0.00	0.00	0.00
February 11, 2019	0.00	0.21	0.03	0.69	0.00	0.03	0.03
February 12, 2019	0.00	0.00	0.00	0.00	0.00	0.00	0.00
February 14, 2019	0.00	0.00	0.00	0.00	0.00	0.00	0.00
March 7, 2019	0.00	0.00	0.00	0.00	0.00	0.00	0.00
March 18, 2019	0.00	0.01	0.00	0.00	0.00	0.99	0.00
April 30, 2019	0.01	0.10	0.01	0.00	0.00	0.88	0.00

Supplementary Table 4.6. Continuation of componentry

Explosion date (M/D/Y)	1000–2000 μm componentry Volume fraction						
	Juvenile	Lithics	Recycled	Hydrothermal	Crystals	Aggregates	Red
August 4, 2016	0.00	0.00	0.00	1.00	0.00	0.00	0.00
April 7, 2017	0.01	0.41	0.09	0.47	0.00	0.03	0.00
April 10, 2017	0.08	0.22	0.03	0.56	0.00	0.11	0.00
April 14, 2017	0.08	0.34	0.24	0.32	0.00	0.01	0.01
April 15, 2017	0.00	0.64	0.00	0.35	0.00	0.00	0.01
April 19, 2017	0.02	0.58	0.04	0.34	0.00	0.01	0.02
April 20, 2017	0.16	0.36	0.12	0.32	0.00	0.00	0.04
April 22, 2017	0.60	0.20	0.12	0.08	0.00	0.00	0.00
May 9,2017	0.71	0.13	0.08	0.07	0.00	0.00	0.00
June 11, 2017	0.00	0.00	0.00	0.00	0.00	0.00	0.00
August 30, 2017	0.00	0.00	0.00	0.00	0.00	0.00	0.00
September 13, 2017	0.72	0.15	0.06	0.06	0.00	0.00	0.01
October 30, 2017	0.00	0.00	0.00	0.00	0.00	0.00	0.00
February 8, 2019	0.00	0.00	0.00	0.00	0.00	0.00	0.00
February 11, 2019	0.00	0.00	0.00	1.00	0.00	0.00	0.00
February 12, 2019	0.00	0.00	0.00	0.00	0.00	0.00	0.00
February 14, 2019	0.00	0.00	0.00	0.00	0.00	0.00	0.00
March 7, 2019	0.00	0.00	0.00	0.00	0.00	0.00	0.00
March 18, 2019	0.00	0.00	0.00	0.00	0.00	0.00	0.00
April 30, 2019	0.00	0.00	0.00	0.00	0.00	0.00	0.00

Supplementary Table 4.7. Continuation of componentry

Explosion date (M/D/Y)	>2000 µm componentry Volume fraction						
	Juvenile	Lithics	Recycled	Hydrothermal	Crystals	Aggregates	Red
August 4, 2016	0.00	0.00	0.00	0.00	0.00	0.00	0.00
April 7, 2017	0.00	0.20	0.20	0.60	0.00	0.00	0.00
April 10, 2017	0.00	0.00	0.00	0.00	0.00	0.00	0.00
April 14, 2017	0.00	0.00	0.00	0.00	0.00	0.00	0.00
April 15, 2017	0.00	0.00	0.00	0.00	0.00	0.00	0.00
April 19, 2017	0.05	0.53	0.00	0.37	0.00	0.05	0.00
April 20, 2017	0.00	0.00	0.00	0.00	0.00	0.00	0.00
April 22, 2017	0.47	0.27	0.19	0.06	0.00	0.00	0.02
May 9,2017	0.00	0.00	0.00	0.00	0.00	0.00	0.00
June 11, 2017	0.00	0.00	0.00	0.00	0.00	0.00	0.00
August 30, 2017	0.00	0.00	0.00	0.00	0.00	0.00	0.00
September 13, 2017	0.00	0.00	0.00	0.00	0.00	0.00	0.00
October 30, 2017	0.00	0.00	0.00	0.00	0.00	0.00	0.00
February 8, 2019	0.00	0.00	0.00	0.00	0.00	0.00	0.00
February 11, 2019	0.00	0.00	0.00	0.00	0.00	0.00	0.00
February 12, 2019	0.00	0.00	0.00	0.00	0.00	0.00	0.00
February 14, 2019	0.00	0.00	0.00	0.00	0.00	0.00	0.00
March 7, 2019	0.00	0.00	0.00	0.00	0.00	0.00	0.00
March 18, 2019	0.00	0.00	0.00	0.00	0.00	0.00	0.00
April 30, 2019	0.00	0.00	0.00	0.00	0.00	0.00	0.00

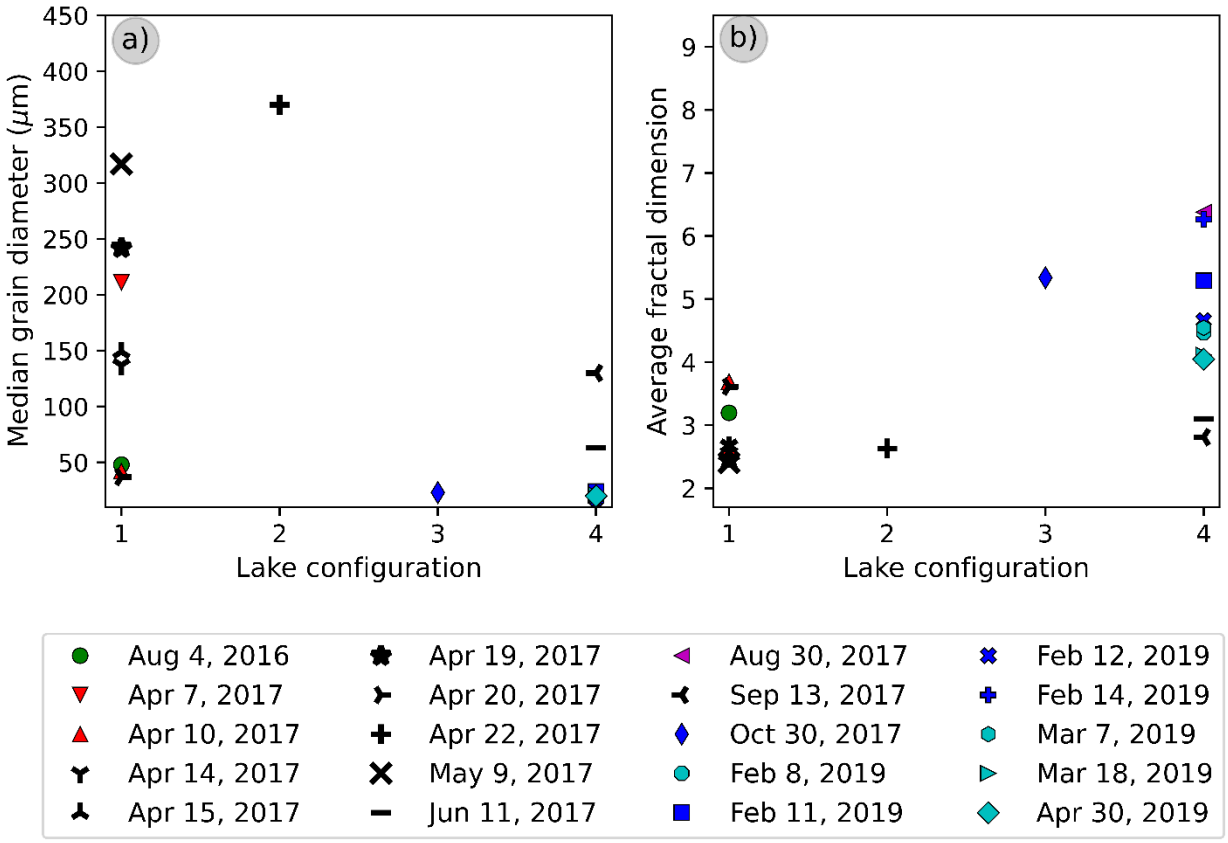

Supplementary Figure 5. A) Median grain diameter (μm) versus lake configuration. B) Average fractal dimension versus lake configuration. Both figures show no correlation between lake configuration, median grain size, and average fractal dimension.

APENDIX B

1. SUPPLEMENTARY FIGURES FOR CHAPTER III

Supplementary material

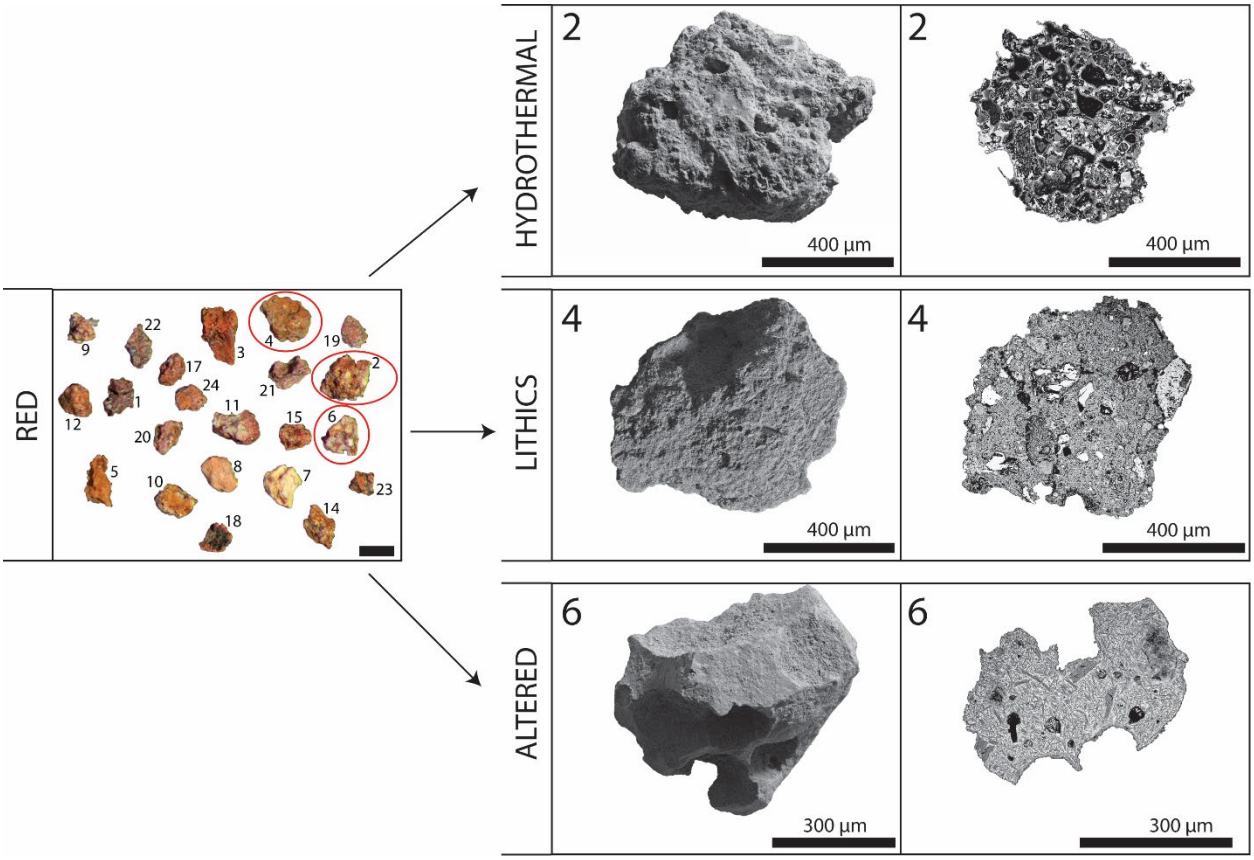

Supplementary Figure 6. Examples of red particles reclassified as another components.

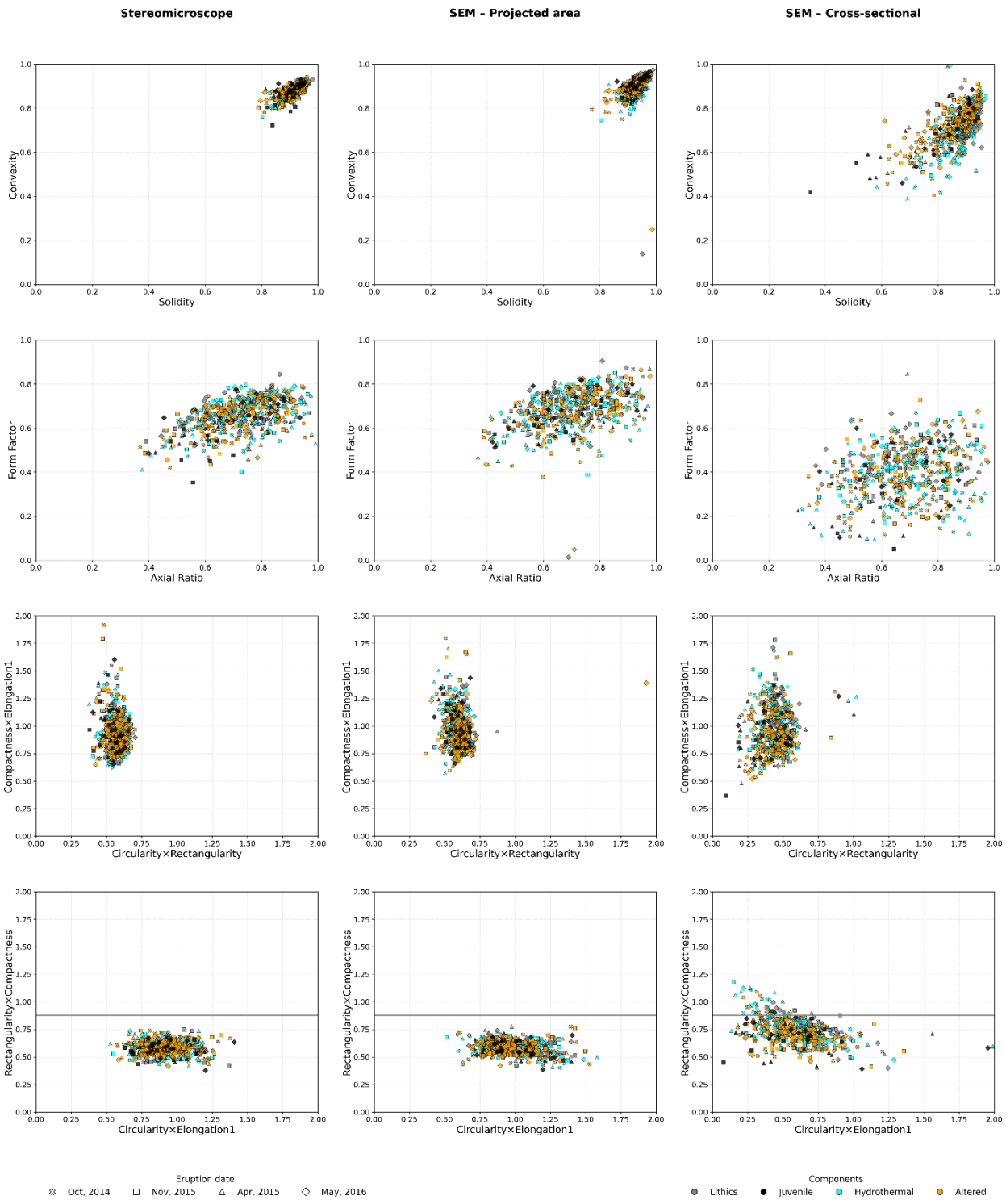

Supplementary Figure 7. Comparison between shape parameters with the different techniques.

REFERENCES

Aguilera, F., Tassi, F., Darrah, T., Moune, S., Vaselli, O., 2012. Geochemical model of a magmatic–hydrothermal system at the Lastarria volcano, northern Chile. Bull Volcanol 74, 119–134. https://doi.org/10.1007/s00445-011-0489-5

Alvarado, G.E., Brenes-Andre, J., Barrantes, M., Vega, E., de Moor, J.M., Avard, G., Dellino, P., Mele, D., DeVitre, C., Di Piazza, A., Rizzo, A.L., Carapezza, M.L., 2016a. Actividad explosiva del turrialba (Costa Rica) en el 2010-2016. Rev. Geol. Amér. Central 55. https://doi.org/10.15517/rgac.v55i0.26965

Alvarado, G.E., Gans, P.B., 2011. Síntesis geocronológica del magmatismo, metamorfismo y metalogenia de Costa Rica, América Central. Rev. Geol. Amér. Central. https://doi.org/10.15517/rgac.v0i46.1836

Alvarado, G.E., Mele, D., Dellino, P., de Moor, J.M., Avard, G., 2016b. Are the ashes from the latest eruptions (2010–2016) at Turrialba volcano (Costa Rica) related to phreatic or phreatomagmatic events? Journal of Volcanology and Geothermal Research 327, 407–415. https://doi.org/10.1016/j.jvolgeores.2016.09.003

Andronico, D., Cristaldi, A., Del Carlo, P., Taddeucci, J., 2009. Shifting styles of basaltic explosive activity during the 2002–03 eruption of Mt. Etna, Italy. Journal of Volcanology and Geothermal Research, Models and products of mafic explosive activity 180, 110–122. https://doi.org/10.1016/j.jvolgeores.2008.07.026

Avard, G., Mora, M., Bakkar, H., Alvarado, G., Angarita, M., Cascante, M., Moor, J.M. de, Martínez, M., Muller, C., Pacheco, J., Ruiz, P., Soto, G., 2021. Volcano hazard and surveillance in Costa Rica. Volcanica 4, 141–161. https://doi.org/10.30909/vol.04.S1.141161

Balangue-Tarriela, M.I.R., Lagmay, A.M.F., Sarmiento, D.M., Vasquez, J., Baldago, M.C., Ybañez, R., Ybañez, A.A., Trinidad, J.R., Thivet, S., Gurioli, L., de Vries, B.V.W., Aurelio, M., Rafael, D.J., Bermas, A., Escudero, J.A., 2022. Analysis of the 2020 Taal Volcano tephra fall deposits from crowdsourced information and field data. Bull Volcanol 84, 35. https://doi.org/10.1007/s00445-022-01534-y

Barberi, F., Bertagnini, A., Landi, P., Principe, C., 1992. A review on phreatic eruptions and their precursors. Journal of Volcanology and Geothermal Research 52, 231–246. https://doi.org/10.1016/0377-0273(92)90046-G

Benet, D., Costa, F., Migadel, K., Lee, D.W.J., D'Oriano, C., Pompilio, M., Nurfiani, D., Rifai, H., 2025. A repository-hosted dataset of volcanic ash particle images and features. Sci Data 12, 681. https://doi.org/10.1038/s41597-025-04942-9

Benet, D., Costa, F., Pedreros, G., Cardona, C., 2021. The volcanic ash record of shallow magma intrusion and dome emplacement at Nevados de Chillán Volcanic complex, Chile. Journal of Volcanology and Geothermal Research 417, 107308. https://doi.org/10.1016/j.jvolgeores.2021.107308

Benet, D., Costa, F., Widiwijayanti, C., 2024. Volcanic Ash Classification Through Machine Learning. Geochemistry, Geophysics, Geosystems 25, e2023GC011224. https://doi.org/10.1029/2023GC011224

Bernard, B., 2013. Homemade ashmeter: a low-cost, high-efficiency solution to improve tephra field-data collection for contemporary explosive eruptions. J Appl. Volcanol. 2, 1. https://doi.org/10.1186/2191-5040-2-1

Brenes-André, J., Alvarado, G.E., Chavarría, N., Sánchez, B., Avard, G., Barrantes, M., Quesada, C., 2020. Análisis de la dinámica y productos balísticos durante la erupción del Poás (Costa Rica) en el 2017. Revista geológica de América central 62. https://doi.org/10.15517/rgac.v62i0.40640

Büttner, R., Dellino, P., La Volpe, L., Lorenz, V., Zimanowski, B., 2002. Thermohydraulic explosions in phreatomagmatic eruptions as evidenced by the comparison between pyroclasts and products from Molten Fuel Coolant Interaction experiments. J. Geophys. Res. 107, ECV 5-1-ECV 5-14. https://doi.org/10.1029/2001JB000511

Büttner, R., Dellino, P., Zimanowski, B., 1999. Identifying magma–water interaction from the surface features of ash particles. Nature 401, 688–690. https://doi.org/10.1038/44364

Calvo, C., Madrigal, K., Merayo, F., Salazar, M., Fallas, C., Alvarado, G.E., Sánchez, B., Sanchez, R., 2019. Vista de Modelo volcanotectónico del graben cuspidal complejo del Turrialba (Costa Rica) y su relación con los colapsos sectoriales bajo un régimen transpresivo y transtensivo. Revista Geológica de América Central 61, 57–77. https://doi.org/10.15517/rgac.v2019i61.000

Cascante, M., Giachetti, T., Wright, H.M.N., Van Eaton, A.R., Avard, G., 2025. Characteristics of volcanic ash reveal changes in fragmentation and eruption dynamics at Poás Volcano, Costa Rica, 2016–2019. Bull Volcanol 87, 36. https://doi.org/10.1007/s00445-025-01820-5

Casertano, L., Borgia, A., Cigolini, C., 1983. El volcan Poas, Costa Rica Cronologia y Caracteristicas de la actividad. Geof. Int. 22, 215–236.

Cashman, K.V., Hoblitt, R.P., 2004. Magmatic precursors to the 18 May 1980 eruption of Mount St. Helens, USA. Geology 32, 141–144. https://doi.org/10.1130/G20078.1

Cashman, K.V., Scheu, B., 2015. Magmatic Fragmentation, in: The Encyclopedia of Volcanoes. Elsevier, pp. 459–471. https://doi.org/10.1016/B978-0-12-385938-9.00025-0

Cioni, R., D'Oriano, C., Bertagnini, A., 2008. Fingerprinting ash deposits of small scale eruptions by their physical and textural features. Journal of Volcanology and Geothermal Research 177, 277–287. https://doi.org/10.1016/j.jvolgeores.2008.06.003

Cioni, R., Pistolesi, M., Bertagnini, A., Bonadonna, C., Hoskuldsson, A., Scateni, B., 2014. Insights into the dynamics and evolution of the 2010 Eyjafjallajökull summit eruption (Iceland) provided by volcanic ash textures. Earth and Planetary Science Letters 394, 111–123. https://doi.org/10.1016/j.epsl.2014.02.051

Conde, V., Bredemeyer, S., Duarte, E., Pacheco, J.F., Miranda, S., Galle, B., Hansteen, T.H., 2014. SO2 degassing from Turrialba Volcano linked to seismic signatures during the period 2008–2012. Int J Earth Sci (Geol Rundsch) 103, 1983–1998. https://doi.org/10.1007/s00531-013-0958-5

Craig, H., Wilson, T., Stewart, C., Outes, V., Villarosa, G., Baxter, P., 2016. Impacts to agriculture and critical infrastructure in Argentina after ashfall from the 2011 eruption of the Cordón Caulle volcanic complex: an assessment of published damage and function thresholds. J Appl. Volcanol. 5, 7. https://doi.org/10.1186/s13617-016-0046-1

D'Arcy, F., de Moor, J.M., Stix, J., Alan, A., Bogue, R., Corrales, E., Diaz, J.A., Mick, E., Salas-Navarro, J., Lauzeral, R., 2022. New insights into carbon isotope systematics at Poás volcano, Costa Rica. Journal of Volcanology and Geothermal Research 431, 107639. https://doi.org/10.1016/j.jvolgeores.2022.107639

de Moor, J.M., Aiuppa, A., Avard, G., Wehrmann, H., Dunbar, N., Muller, C., Tamburello, G., Giudice, G., Liuzzo, M., Moretti, R., Conde, V., Galle, B., 2016a. Turmoil at Turrialba Volcano (Costa Rica): Degassing and eruptive processes inferred from high-frequency gas monitoring. J. Geophys. Res. Solid Earth 121, 5761–5775. https://doi.org/10.1002/2016JB013150

de Moor, J.M., Aiuppa, A., Pacheco, J., Avard, G., Kern, C., Liuzzo, M., Martínez, M., Giudice, G., Fischer, T.P., 2016b. Short-period volcanic gas precursors to phreatic eruptions: Insights from Poás Volcano, Costa Rica. Earth and Planetary Science Letters 442, 218–227. https://doi.org/10.1016/j.epsl.2016.02.056

de Moor, J.M., Stix, J., Avard, G., Muller, C., Corrales, E., Diaz, J.A., Alan, A., Brenes, J., Pacheco, J., Aiuppa, A., Fischer, T.P., 2019. Insights on Hydrothermal-Magmatic Interactions and Eruptive Processes at Poás Volcano (Costa Rica) From High-Frequency Gas Monitoring and Drone Measurements. Geophysical Research Letters 46, 1293–1302. https://doi.org/10.1029/2018GL080301

Dellino, P., De Astis, G., La Volpe, L., Mele, D., Sulpizio, R., 2011. Quantitative hazard assessment of phreatomagmatic eruptions at Vulcano (Aeolian Islands, Southern Italy) as obtained by combining stratigraphy, event statistics and physical modelling. Journal of Volcanology and Geothermal Research, From maars to scoria cones: the enigma of monogenetic volcanic fields 201, 364–384. https://doi.org/10.1016/j.jvolgeores.2010.06.009

Dellino, P., Gudmundsson, M.T., Larsen, G., Mele, D., Stevenson, J.A., Thordarson, T., Zimanowski, B., 2018. Ash from the Eyjafjallajökull eruption (Iceland): Fragmentation processes and aerodynamic behavior. Journal of Geophysical Research: Atmospheres. https://doi.org/10.1029/2011JB008726@10.1002/(ISSN)2169-8996.ICEVOLCAN1

Dellino, P., Gudmundsson, M.T., Larsen, G., Mele, D., Stevenson, J.A., Thordarson, T., Zimanowski, B., 2012. Ash from the Eyjafjallajökull eruption (Iceland): Fragmentation processes and aerodynamic behavior. Journal of Geophysical Research: Solid Earth 117. https://doi.org/10.1029/2011JB008726

Dellino, P., Kyriakopoulos, K., 2003. Phreatomagmatic ash from the ongoing eruption of Etna reaching the Greek island of Cefalonia. Journal of Volcanology and Geothermal Research 126, 341–345. https://doi.org/10.1016/S0377-0273(03)00154-9

Dellino, P., Liotino, G., 2002. The fractal and multifractal dimension of volcanic ash particles contour: a test study on the utility and volcanological relevance. Journal of Volcanology and Geothermal Research 113, 1–18. https://doi.org/10.1016/S0377-0273(01)00247-5

DeVitre, C.L., Gazel, E., Allison, C.M., Soto, G., Madrigal, P., Alvarado, G.E., Lücke, O.H., 2019. Multi-stage chaotic magma mixing at Turrialba volcano. Journal of Volcanology and Geothermal Research 381, 330–346. https://doi.org/10.1016/j.jvolgeores.2019.06.011

Di Piazza, A., Rizzo, A.L., Barberi, F., Carapezza, M.L., De Astis, G., Romano, C., Sortino, F., 2015. Geochemistry of the mantle source and magma feeding system beneath Turrialba volcano, Costa Rica. Lithos 232, 319–335. https://doi.org/10.1016/j.lithos.2015.07.012

Di Piazza, A., Vona, A., Mollo, S., De Astis, G., Soto, G.J., Romano, C., 2019. Unsteady magma discharge during the "El Retiro" subplinian eruption (Turrialba volcano, Costa Rica): Insights from textural and petrological analyses. Journal of Volcanology and Geothermal Research 371, 101–115. https://doi.org/10.1016/j.jvolgeores.2019.01.004

Dinis, P., Castilho, A., 2012. Integrating Sieving and Laser Data To Obtain Bulk Grain-Size Distributions. Journal of Sedimentary Research 82, 747–754. https://doi.org/10.2110/jsr.2012.62

D'Oriano, C., Bertagnini, A., Cioni, R., Pompilio, M., 2014. Identifying recycled ash in basaltic eruptions. Sci Rep 4, 5851. https://doi.org/10.1038/srep05851

D'Oriano, C., Bertagnini, A., Pompilio, M., 2011. Ash erupted during normal activity at Stromboli (Aeolian Islands, Italy) raises questions on how the feeding system works. Bull Volcanol 73, 471–477. https://doi.org/10.1007/s00445-010-0425-0

D'Oriano, C., Del Carlo, P., Andronico, D., Cioni, R., Gabellini, P., Cristaldi, A., Pompilio, M., 2022. Syn-Eruptive Processes During the January–February 2019 Ash-Rich Emissions Cycle at Mt. Etna (Italy): Implications for Petrological Monitoring of Volcanic Ash. Front. Earth Sci. 10. https://doi.org/10.3389/feart.2022.824872

Dufek, J., Manga, M., Patel, A., 2012. Granular disruption during explosive volcanic eruptions. Nature Geosci 5, 561–564. https://doi.org/10.1038/ngeo1524

Fagents, S.A., Gregg, T.K.P., Lopes, R.M.C., 2013. Modeling Volcanic Processes: The Physics and Mathematics of Volcanism. Cambridge University Press, Cambridge, UNITED KINGDOM.

Gaunt, H.E., Bernard, B., Hidalgo, S., Proaño, A., Wright, H., Mothes, P., Criollo, E., Kueppers, U., 2016. Juvenile magma recognition and eruptive dynamics inferred from the analysis of ash time series: The 2015 reawakening of Cotopaxi volcano. Journal of Volcanology and Geothermal Research 328, 134–146. https://doi.org/10.1016/j.jvolgeores.2016.10.013

Giachetti, T., Trafton, K.R., Wiejaczka, J., Gardner, J.E., Watkins, J.M., Shea, T., Wright, H.M.N., 2021. The products of primary magma fragmentation finally revealed by pumice agglomerates. Geology 49, 1307–1311. https://doi.org/10.1130/G48902.1

Gonnermann, H.M., 2015. Magma Fragmentation. Annu. Rev. Earth Planet. Sci. 43, 431–458. https://doi.org/10.1146/annurev-earth-060614-105206

Gunawan, H., Surono, Budianto, A., Kristianto, Prambada, O., McCausland, W., Pallister, J., Iguchi, M., 2019. Overview of the eruptions of Sinabung Volcano, 2010 and 2013–present and details of the 2013 phreatomagmatic phase. Journal of Volcanology and Geothermal Research, Lessons learned from the recent eruptions of Sinabung and Kelud Volcanoes, Indonesia 382, 103–119. https://doi.org/10.1016/j.jvolgeores.2017.08.005

Hamzah, W.N., Ohba, T., Gurusinga, M.A., Moktikanana, M.L.A., Indriyanto, J.N., Hoshide, T., Abdurrahman, M., Kurniawan, I.A., Fadlin, 2025. Transition from magmatic to phreatomagmatic eruptions in Young Ciremai volcano, Indonesia: insights from stratigraphy, componentry, and textural analysis of tephra deposits. Earth Planets Space 77, 16. https://doi.org/10.1186/s40623-025-02143-7

Horwell, C.J., 2007. Grain-size analysis of volcanic ash for the rapid assessment of respiratory health hazard. J. Environ. Monit. 9, 1107. https://doi.org/10.1039/b710583p

Houghton, B., White, J.D.L., Van Eaton, A.R., 2015. Chapter 30 - Phreatomagmatic and Related Eruption Styles, in: Sigurdsson, H. (Ed.), The Encyclopedia of Volcanoes (Second Edition). Academic Press, Amsterdam, pp. 537–552. https://doi.org/10.1016/B978-0-12-385938-9.00030-4

Houghton, B.F., Smith, R.T., 1993. Recycling of magmatic clasts during explosive eruptions: estimating the true juvenile content of phreatomagmatic volcanic deposits. Bull Volcanol 55, 414–420. https://doi.org/10.1007/BF00302001

Iguchi, M., Nakamichi, H., Tanaka, H., Ohta, Y., Shimizu, A., Miki, D., Sakurajima Volcano Research Center, Disaster Prevention Research Institute, Kyoto University 1722-19 Sakurajima-Yokoyama-cho, Kagoshima 891-1419, Japan, University of Tsukuba, Ibaraki, Japan, Tohoku University, Miyagi, Japan, National Institute for Environmental Studies, Ibaraki, Japan, 2019. Integrated Monitoring of Volcanic Ash and Forecasting at Sakurajima Volcano, Japan. JDR 14, 798–809. https://doi.org/10.20965/jdr.2019.p0798

Informes Técnicos [WWW Document], n.d. URL https://www.ovsicori.una.ac.cr/index.php/vulcanologia/informes-y-boletines/informes-tecnicos?start=120 (accessed 3.22.25).

Inman, D.L., 1949. Sorting of sediments in the light of fluid mechanics. Journal of Sedimentary Research 19, 51–70. https://doi.org/10.1306/D426934B-2B26-11D7-8648000102C1865D

Kaminski, E., Jaupart, C., 1998. The size distribution of pyroclasts and the fragmentation sequence in explosive volcanic eruptions. Journal of Geophysical Research: Solid Earth 103, 29759–29779. https://doi.org/10.1029/98JB02795

Kanamitsu, M., Ebisuzaki, W., Woollen, J., Yang, S.-K., Hnilo, J.J., Fiorino, M., Potter, G.L., 2002. NCEP–DOE AMIP-II Reanalysis (R-2). Bulletin of the American Meteorological Society 83, 1631–1644. https://doi.org/10.1175/BAMS-83-11-1631

Kueppers, U., Scheu, B., Spieler, O., Dingwell, D.B., 2006. Fragmentation efficiency of explosive volcanic eruptions: A study of experimentally generated pyroclasts. Journal of Volcanology and Geothermal Research, MULTIMO: Multi-Parameter Monitoring, Modelling and Forecasting of Volcanic Hazard 153, 125–135. https://doi.org/10.1016/j.jvolgeores.2005.08.006

Leibrandt, S., Le Pennec, J.-L., 2015. Towards fast and routine analyses of volcanic ash morphometry for eruption surveillance applications. Journal of Volcanology and Geothermal Research 297, 11–27. https://doi.org/10.1016/j.jvolgeores.2015.03.014

Liu, E.J., Cashman, K.V., Miller, E., Moore, H., Edmonds, M., Kunz, B.E., Jenner, F., Chigna, G., 2020. Petrologic monitoring at Volcán de Fuego, Guatemala. Journal of Volcanology and Geothermal Research 405, 107044. https://doi.org/10.1016/j.jvolgeores.2020.107044

Liu, E.J., Cashman, K.V., Rust, A.C., 2015a. Optimising shape analysis to quantify volcanic ash morphology. GeoResJ 8, 14–30. https://doi.org/10.1016/j.grj.2015.09.001

Liu, E.J., Cashman, K.V., Rust, A.C., Gislason, S.R., 2015b. The role of bubbles in generating fine ash during hydromagmatic eruptions. Geology 43, 239–242. https://doi.org/10.1130/G36336.1

Liu, E.J., Cashman, K.V., Rust, A.C., Höskuldsson, A., 2017. Contrasting mechanisms of magma fragmentation during coeval magmatic and hydromagmatic activity: the Hverfjall Fires fissure eruption, Iceland. Bull Volcanol 79, 68. https://doi.org/10.1007/s00445-017-1150-8

Lowenstern, J.B., van Hinsberg, V., Berlo, K., Liesegang, M., Iacovino, K., Bindeman, I.N., Wright, H.M., 2018. Opal-A in Glassy Pumice, Acid Alteration, and the 1817 Phreatomagmatic Eruption at Kawah Ijen (Java), Indonesia. Front. Earth Sci. 6. https://doi.org/10.3389/feart.2018.00011

Lücke, O.H., Calderón, A., 2016. Characterization of the ashes from the 2014-2015 Turrialba Volcano eruptions by means of Scanning Electron Microscopy and Energy Dispersive X-Ray Spectroscopy. 1. https://doi.org/10.15517/rgac.v54i0.23281

Lupi, M., Geiger, S., Carey, R.J., Thordarson, T., Houghton, B.F., 2011. A model for syn-eruptive groundwater flow during the phreatoplinian phase of the 28–29 March 1875 Askja volcano eruption, Iceland. Journal of Volcanology and Geothermal Research 203, 146–157. https://doi.org/10.1016/j.jvolgeores.2011.04.009

Madrigal, P., Lücke, O.H., 2017. Petrographic Analysis of the Volcanic Bombs and Blocks from Poás Volcano: April-June 2017 Eruptive Period. Rev. Geol. Amér. Central. https://doi.org/10.15517/rgac.v0i57.30336

Maeno, F., Shohata, S., Suzuki, Y., Hokanishi, N., Yasuda, A., Ikenaga, Y., Kaneko, T., Nakada, S., 2023. Eruption style transition during the 2017–2018 eruptive activity at the Shinmoedake volcano, Kirishima, Japan: surface phenomena and eruptive products. Earth Planets Space 75, 76. https://doi.org/10.1186/s40623-023-01834-3

Maria, A., Carey, S., 2002. Using fractal analysis to quantitatively characterize the shapes of volcanic particles. Journal of Geophysical Research: Solid Earth 107, ECV 7-1-ECV 7-17. https://doi.org/10.1029/2001JB000822

Martínez Cruz, M., 2008. Geochemical evolution of the acid crater lake of Poas volcano (Costa Rica): Insights into volcanic-hydrothermal processes [WWW Document]. URL https://dspace.library.uu.nl/handle/1874/295352 (accessed 7.25.23).

Martini, F., Tassi, F., Vaselli, O., Del Potro, R., Martinez, M., del Laat, R.V., Fernandez, E., 2010. Geophysical, geochemical and geodetical signals of reawakening at Turrialba volcano (Costa Rica) after almost 150years of quiescence. Journal of Volcanology and Geothermal Research 198, 416–432. https://doi.org/10.1016/j.jvolgeores.2010.09.021

Martínez, M., Fernández, E., Valdés, J., Barboza, V., Van der Laat, R., Duarte, E., Malavassi, E., Sandoval, L., Barquero, J., Marino, T., 2000. Chemical evolution and volcanic activity of the active crater lake of Poás volcano, Costa Rica, 1993–1997. Journal of Volcanology and Geothermal Research 97, 127–141. https://doi.org/10.1016/S0377-0273(99)00165-1

Mastin, L.G., 2007. Generation of fine hydromagmatic ash by growth and disintegration of glassy rinds. Journal of Geophysical Research: Solid Earth 112. https://doi.org/10.1029/2005JB003883

Matsumoto, K., Geshi, N., 2021. Shallow crystallization of eruptive magma inferred from volcanic ash microtextures: a case study of the 2018 eruption of Shinmoedake volcano, Japan. Bull Volcanol 83, 31. https://doi.org/10.1007/s00445-021-01451-6

Mick, E., Stix, J., de Moor, J.M., Avard, G., 2021. Hydrothermal alteration and sealing at Turrialba volcano, Costa Rica, as a mechanism for phreatic eruption triggering. Journal of Volcanology and Geothermal Research 416, 107297. https://doi.org/10.1016/j.jvolgeores.2021.107297

Minami, Y., Imura, T., Hayashi, S., Ohba, T., 2016. Mineralogical study on volcanic ash of the eruption on September 27, 2014 at Ontake volcano, central Japan: correlation with porphyry copper systems. Earth, Planets and Space 68, 67. https://doi.org/10.1186/s40623-016-0440-2

Mineral data [WWW Document], n.d. URL https://webmineral.com/Alphabetical_Listing.shtml (accessed 6.14.25).

Miwa, T., Geshi, N., Itoh, J., Tanada, T., Iguchi, M., 2021. Automatic onsite imaging of volcanic ash particles with VOLCAT: Towards quasi-real-time eruption style monitoring. Journal of Volcanology and Geothermal Research 416, 107267. https://doi.org/10.1016/j.jvolgeores.2021.107267

Miwa, T., Geshi, N., Shinohara, H., 2013. Temporal variation in volcanic ash texture during a vulcanian eruption at the Sakurajima volcano, Japan. Journal of Volcanology and Geothermal Research 260, 80–89. https://doi.org/10.1016/j.jvolgeores.2013.05.010

Miwa, T., Toramaru, A., Iguchi, M., 2009. Correlations of volcanic ash texture with explosion earthquakes from vulcanian eruptions at Sakurajima volcano, Japan. Journal of Volcanology and Geothermal Research 184, 473–486. https://doi.org/10.1016/j.jvolgeores.2009.05.012

Montanaro, C., Mick, E., Salas-Navarro, J., Caudron, C., Cronin, S.J., de Moor, J.M., Scheu, B., Stix, J., Strehlow, K., 2022. Phreatic and Hydrothermal Eruptions: From Overlooked to Looking Over. Bull Volcanol 84, 64. https://doi.org/10.1007/s00445-022-01571-7

Mora Amador, R.A., Rouwet, D., González, G., Vargas, P., Ramírez, C., 2019. Volcanic Hazard Assessment of Poás (Costa Rica) Based on the 1834, 1910, 1953–1955 and 2017 Historical Eruptions, in: Tassi, F., Vaselli, O., Mora Amador, Raul Alberto (Eds.), Poás Volcano: The

Pulsing Heart of Central America Volcanic Zone, Active Volcanoes of the World. Springer International Publishing, Cham, pp. 261–299. https://doi.org/10.1007/978-3-319-02156-0_11

Moussallam, Y., Peters, N., Ramírez, C., Oppenheimer, C., Aiuppa, A., Giudice, G., 2014. Characterisation of the magmatic signature in gas emissions from Turrialba Volcano, Costa Rica. Solid Earth 5, 1341–1350. https://doi.org/10.5194/se-5-1341-2014

Murtagh, R.M., White, J.D.L., 2013. Pyroclast characteristics of a subaqueous to emergent Surtseyan eruption, Black Point volcano, California. Journal of Volcanology and Geothermal Research 267, 75–91. https://doi.org/10.1016/j.jvolgeores.2013.08.015

Newhall, C., Hoblitt, R., 2002. Constructing event trees for volcanic crises. Bull Volcanol 64, 3–20. https://doi.org/10.1007/s004450100173

Nurfiani, D., Bouvet de Maisonneuve, C., 2018. Furthering the investigation of eruption styles through quantitative shape analyses of volcanic ash particles. Journal of Volcanology and Geothermal Research 354, 102–114. https://doi.org/10.1016/j.jvolgeores.2017.12.001

Ohba, T., Kitade, Y., 2005. Subvolcanic hydrothermal systems: Implications from hydrothermal minerals in hydrovolcanic ash. Journal of Volcanology and Geothermal Research 145, 249–262. https://doi.org/10.1016/j.jvolgeores.2005.02.002

Pardo, N., Cronin, S.J., Németh, K., Brenna, M., Schipper, C.I., Breard, E., White, J.D.L., Procter, J., Stewart, B., Agustín-Flores, J., Moebis, A., Zernack, A., Kereszturi, G., Lube, G., Auer, A., Neall, V., Wallace, C., 2014. Perils in distinguishing phreatic from phreatomagmatic ash; insights into the eruption mechanisms of the 6 August 2012 Mt. Tongariro eruption, New Zealand. Journal of Volcanology and Geothermal Research 286, 397–414. https://doi.org/10.1016/j.jvolgeores.2014.05.001

Primulyana, S., Kern, C., Lerner, A.H., Saing, U.B., Kunrat, S.L., Alfianti, H., Marlia, M., 2019. Gas and ash emissions associated with the 2010–present activity of Sinabung Volcano, Indonesia. Journal of Volcanology and Geothermal Research, Lessons learned from the recent eruptions of Sinabung and Kelud Volcanoes, Indonesia 382, 184–196. https://doi.org/10.1016/j.jvolgeores.2017.11.018

Prosser, J.T., Carr, M.J., 1987. Poás volcano, Costa Rica: Geology of the summit region and spatial and temporal variations among the most recent lavas. Journal of Volcanology and Geothermal Research 33, 131–146. https://doi.org/10.1016/0377-0273(87)90057-6

Re, G., Corsaro, R.A., D'Oriano, C., Pompilio, M., 2021. Petrological monitoring of active volcanoes: A review of existing procedures to achieve best practices and operative protocols during eruptions. Journal of Volcanology and Geothermal Research 419, 107365. https://doi.org/10.1016/j.jvolgeores.2021.107365

Reagan, M., Duarte, E., Soto, G.J., Fernández, E., 2006. The eruptive history of Turrialba volcano, Costa Rica, and potential hazards from future eruptions, in: Volcanic Hazards in Central America. Geological Society of America. https://doi.org/10.1130/2006.2412(13)

Reagan, M.K., Rowe, M.C., Duarte, E., Fernandez, E., 2011. Juvenile glass fragments in phreatic explosion debris from Turrialba Volcano, Costa Rica, in: 3. Presented at the Goldschmidt Conference Abstracts, Mineral Magazine, Praga, p. 1700.

Rizzo, A.L., Di Piazza, A., de Moor, J.M., Alvarado, G.E., Avard, G., Carapezza, M.L., Mora, M.M., 2016. Eruptive activity at Turrialba volcano (Costa Rica): Inferences from 3He/4He in fumarole gases and chemistry of the products ejected during 2014 and 2015. Geochem. Geophys. Geosyst. 17, 4478–4494. https://doi.org/10.1002/2016GC006525

Roduit, N., 2007. JMicroVision: un logiciel d'analyse d'images pétrographiques polyvalent. Section des Sciences de la Terre, Université de Genève, Genève.

Romero, J.E., Aguilera, F., Delgado, F., Guzmán, D., Van Eaton, A.R., Luengo, N., Caro, J., Bustillos, J., Guevara, A., Holbik, S., Tormey, D., Zegarra, I., 2020. Combining ash analyses with remote sensing to identify juvenile magma involvement and fragmentation mechanisms during the 2018/19 small eruption of Peteroa volcano (Southern Andes). Journal of Volcanology and Geothermal Research 106984. https://doi.org/10.1016/j.jvolgeores.2020.106984

Ruiz Cubillo, P., 2012. Reconstruction of the Paleo and Neo stages of Poás and Turrialba volcanoes, Costa Rica: competing processes of growth and destruction. Rutgers University - Graduate School - New Brunswick. https://doi.org/10.7282/T3PG1QHX

Ruiz, P., Gazel, E., Alvarado, G.E., Carr, M.J., Soto, G.J., 2009. Caracterización geoquímica y petrográfica de las unidades geológicas del macizo del volcán Poás, Costa Rica. Rev. Geol. Amér. Central. https://doi.org/10.15517/rgac.v0i43.3457

Rymer, H., Locke, C.A., Borgia, A., Martinez, M., Brenes, J., Van der Laat, R., Williams-Jones, G., 2009. Long-term fluctuations in volcanic activity: implications for future environmental impact. Terra Nova 21, 304–309. https://doi.org/10.1111/j.1365-3121.2009.00885.x

Salvage, R.O., Avard, G., de Moor, J.M., Pacheco, J.F., Brenes Marin, J., Cascante, M., Muller, C., Martinez Cruz, M., 2018. Renewed Explosive Phreatomagmatic Activity at Poás Volcano, Costa Rica in April 2017. Front. Earth Sci. 6, 160. https://doi.org/10.3389/feart.2018.00160

Sheridan, M.F., Wohletz, K.H., 1981. Hydrovolcanic Explosions: The Systematics of Water-Pyroclast Equilibration. Science 212, 1387–1389. https://doi.org/10.1126/science.212.4501.1387

Shoji, D., Noguchi, R., Otsuki, S., Hino, H., 2018. Classification of volcanic ash particles using a convolutional neural network and probability. Sci Rep 8, 8111. https://doi.org/10.1038/s41598-018-26200-2

Soto, G.J., 1988. Estructuras Volcano-Tectonicas del Volcan Turrialba, Costa Rica, America Central.

Stix, J., 2018. Understanding Fast and Slow Unrest at Volcanoes and Implications for Eruption Forecasting. Front. Earth Sci. 6. https://doi.org/10.3389/feart.2018.00056

Stix, J., de Moor, J.M., 2018. Understanding and forecasting phreatic eruptions driven by magmatic degassing. Earth Planets Space 70, 83. https://doi.org/10.1186/s40623-018-0855-z

Suzuki, Y., Nagai, M., Maeno, F., Yasuda, A., Hokanishi, N., Shimano, T., Ichihara, M., Kaneko, T., Nakada, S., 2013. Precursory activity and evolution of the 2011 eruption of Shinmoe-dake in Kirishima volcano—insights from ash samples. Earth Planet Sp 65, 11. https://doi.org/10.5047/eps.2013.02.004

Taddeucci, J., Pompilio, M., Scarlato, P., 2002. Monitoring the explosive activity of the July–August 2001 eruption of Mt. Etna (Italy) by ash characterization. Geophysical Research Letters 29, 71-1-71–4. https://doi.org/10.1029/2001GL014372

Taddeucci, J., Scarlato, P., Andronico, D., Cristaldi, A., Büttner, R., Zimanowski, B., Küppers, U., 2007. Advances in the study of volcanic ash. Eos, Transactions American Geophysical Union 88, 253–256. https://doi.org/10.1029/2007EO240001

Tassi, F., Vaselli, O., Barboza, V., Fernandez, E., Duarte, E., 2004. Fluid geochemistry and seismic activity in the period 1998-2002 at Turrialba Volcano (Costa Rica). Annals of Geophysics 47, 12.

Trafton, K.R., Giachetti, T., 2021. The morphology and texture of Plinian pyroclasts reflect their lateral sourcing in the conduit. Earth and Planetary Science Letters 562, 116844. https://doi.org/10.1016/j.epsl.2021.116844

Turcotte, D.L., 1997. Fractals and Chaos in Geology and Geophysics [WWW Document]. Cambridge Core. https://doi.org/10.1017/CBO9781139174695

Turcotte, D.L., 1986. Fractals and fragmentation. Journal of Geophysical Research: Solid Earth 91, 1921–1926. https://doi.org/10.1029/JB091iB02p01921

van der Laat, L., Mora, M.M., Pacheco, J.Fco., Lesage, P., Meneses, E., 2022. Seismicity during the recent activity (2009–2020) of Turrialba volcano, Costa Rica. Journal of Volcanology and Geothermal Research 431, 107651. https://doi.org/10.1016/j.jvolgeores.2022.107651

van Hinsberg, V., Berlo, K., Lowenstern, J., 2020. An Experimental Investigation of Interaction between Andesite and Hyperacidic Volcanic Lake Water. Minerals 10, 96. https://doi.org/10.3390/min10020096

Vargas-Alfaro, M., Douglas-Gordon, S., Chamizo-Garcia, H., 2023. Exposición a ceniza volcánica producida por el volcán Turrialba y enfermedades respiratorias, Costa Rica, 2016. HS 22, 517–526. https://doi.org/10.19136/hs.a22n3.5628

Vaselli, O., Tassi, F., Duarte, E., Fernandez, E., Poreda, R.J., Huertas, A.D., 2010. Evolution of fluid geochemistry at the Turrialba volcano (Costa Rica) from 1998 to 2008. Bull Volcanol 72, 397–410. https://doi.org/10.1007/s00445-009-0332-4

Watanabe, Koichiro, Danhara, T., Watanabe, Kazunori, Terai, K., Yamashita, T., 1999. Juvenile volcanic glass erupted before the appearance of the 1991 lava dome, Unzen volcano, Kyushu, Japan. Journal of Volcanology and Geothermal Research 89, 113–121. https://doi.org/10.1016/S0377-0273(98)00127-9

White, J.D.L., 1996. Impure coolants and interaction dynamics of phreatomagmatic eruptions. Journal of Volcanology and Geothermal Research 74, 155–170. https://doi.org/10.1016/S0377-0273(96)00061-3

Wiejaczka, J., Giachetti, T., 2022. Using Eruption Source Parameters and High-Resolution Grain-Size Distributions of the 7.7 ka Cleetwood Eruption of Mount Mazama (Oregon, United States) to Reveal Primary and Secondary Eruptive Processes. Front. Earth Sci. 10. https://doi.org/10.3389/feart.2022.853021

Wilson, T.M., Stewart, C., Sword-Daniels, V., Leonard, G.S., Johnston, D.M., Cole, J.W., Wardman, J., Wilson, G., Barnard, S.T., 2012. Volcanic ash impacts on critical infrastructure. Physics and Chemistry of the Earth, Parts A/B/C, Volcanic ash: an agent in Earth systems 45–46, 5–23. https://doi.org/10.1016/j.pce.2011.06.006

Wohletz, K.H., 1983. Mechasnisms of Hydrovolcanic Pyroclast Formation: Grain-Size, Scanning Electron Microscopy, and Experimental Studies. Journal of Volcanology and Geothermal Research 17, 31–63.

Wright, H.M.N., Pallister, J.S., McCausland, W.A., Griswold, J.P., Andreastuti, S., Budianto, A., Primulyana, S., Gunawan, H., Battaglia, M., Diefenbach, A., Griswold, J., Ewert, J., Kelly, P., Kern, C., LaFevers, M., Lockhart, A., Marso, J., Mayberry, G., McCausland, W., Pallister, J., Schilling, S., Wessels, R., White, R., Wright, H., Aisyah, N., Andreastuti, S., Budianto, A., Heriwaseso, A., Kartadinata, N., Kristianto, Primulyana, S., Putra, R., Saing, U.B., Solihin, A., Suparman, Y., Syahbana, D.D., Triastuty, H., 2019. Construction of probabilistic event trees for eruption forecasting at Sinabung volcano, Indonesia 2013–14. Journal of Volcanology and Geothermal Research, Lessons learned from the recent eruptions of Sinabung and Kelud Volcanoes, Indonesia 382, 233–252. https://doi.org/10.1016/j.jvolgeores.2018.02.003

Yaguchi, M., Ohba, T., Hirayama, Y., Numanami, N., 2022. Volcanic Ash from the June 17, 1962 Eruption of Yakedake Volcano: Stereomicroscopic, XRD, and Water-Soluble Components Analyses. Journal of Disaster Research 17, 257–262. https://doi.org/10.20965/jdr.2022.p0257

Yamanoi, Y., Takeuchi, S., Okumura, S., Nakashima, S., Yokoyama, T., 2008. Color measurements of volcanic ash deposits from three different styles of summit activity at Sakurajima volcano, Japan: Conduit processes recorded in color of volcanic ash. Journal of Volcanology and Geothermal Research, Dynamics of Volcanic Explosions: Field Observations, Experimental Constraints and Integrated Modelling 178, 81–93. https://doi.org/10.1016/j.jvolgeores.2007.11.013

Zimanowski, B., Büttner, R., Dellino, P., White, J.D.L., Wohletz, K.H., 2015. Magma–Water Interaction and Phreatomagmatic Fragmentation, in: The Encyclopedia of Volcanoes. Elsevier, pp. 473–484. https://doi.org/10.1016/B978-0-12-385938-9.00026-2

Zimanowski, B., Büttner, R., Lorenz, V., 1997. Premixing of magma and water in MFCI experiments. Bulletin of Volcanology 58, 491–495. https://doi.org/10.1007/s004450050157

Zimanowski, B., Fröhlich, G., Lorenz, V., 1991. Quantitative experiments on phreatomagmatic explosions. Journal of Volcanology and Geothermal Research 48, 341–358. https://doi.org/10.1016/0377-0273(91)90050-A

Zimanowski, B., Wohletz, K., Dellino, P., Büttner, R., 2003. The volcanic ash problem. Journal of Volcanology and Geothermal Research 122, 1–5. https://doi.org/10.1016/S0377-0273(02)00471-7